POLYPUBLIE
Polytechnique Montréal

Titre: Title:	Field-Resolved Detection of Terahertz Pulses Based on a Four-Wave Mixing Nonlinearity
Auteur: Author:	Marco Scaglia
Date:	2022
Type:	Mémoire ou thèse / Dissertation or Thesis
Référence: Citation:	Scaglia, M. (2022). Field-Resolved Detection of Terahertz Pulses Based on a Four-Wave Mixing Nonlinearity [Mémoire de maîtrise, Polytechnique Montréal]. PolyPublie. https://publications.polymtl.ca/10590/

Document en libre accès dans PolyPublie
Open Access document in PolyPublie

URL de PolyPublie: PolyPublie URL:	https://publications.polymtl.ca/10590/
Directeurs de recherche: Advisors:	Denis Seletskiy
Programme: Program:	Génie physique

POLYTECHNIQUE MONTRÉAL

affiliée à l'Université de Montréal

Field-Resolved Detection of Terahertz Pulses
Based on a Four-Wave Mixing Nonlinearity

MARCO SCAGLIA

Département de génie physique

Mémoire présenté en vue de l'obtention du diplôme de *Maîtrise ès sciences appliquées*
Génie physique

Novembre 2022

POLYTECHNIQUE MONTRÉAL

affiliée à l'Université de Montréal

Ce mémoire intitulé :

Field-Resolved Detection of Terahertz Pulses
Based on a Four-Wave Mixing Nonlinearity

présenté par **Marco SCAGLIA**
en vue de l'obtention du diplôme de *Maîtrise ès sciences appliquées*
a été dûment accepté par le jury d'examen constitué de :

Maksim SKOROBOGATIY, président
Denis SELETSKIY, membre et directeur de recherche
Mohammad S. SHARAWI, membre

DEDICATION

To my family and friends

ACKNOWLEDGEMENTS

I would like to express my sincere gratitude to Professor Denis Seletskiy for taking a chance on me and making my Double Degree project come true by welcoming me in the femtoQ team. The conversations we had on a regular basis allowed me to grow as a young researcher and helped me in pushing my understanding of theoretical and experimental aspects to a deeper level. I am also grateful for the support and assistance that Stéphane Virally provided throughout these last two years, being a motivating reference for the team. Thank you as well to my thesis' co-supervisor from Politecnico di Milano, Professor Salvatore Stagira, whose expertise in the terahertz field, added with Professor Seletskiy's one, helped me in shaping this challenging project and reaching the various goals we defined. I am thankful for Professor Maksim Skorobogatiy and Professor Mohammad S. Sharawi for accepting to take on the role of jury member of my Master thesis' defense and for providing valuable feedback to make the thesis more complete.

I thank my femtoQ colleagues Patrick, Gabriel, Etienne, Laurent, Grégory-Samuel, Émile, Justine, Sho, Shilong and all the interns for the inspiring discussions and for creating a pleasant and fun atmosphere within the group. In particular, I acknowledge Gabriel for sharing the burden of ensuring proper performance of the OPA, Etienne for giving me invaluable advice on the design of a THz system, Patrick for the guidance on pulse measurements and the unlimited answers regarding coding, Grégory-Samuel for his knowledge on THz generation and detection and for the countless hours spent in the lab hunting for the signal.

I am beyond grateful for my family, who has been a constant source of encouragement and support from day one and who gracefully accepted to let me go and experience the world, even if it meant putting an ocean between us. Thank you to my partner, Brunda, for her patience across this roller-coaster ride and for always reminding me of my potential. Thanks to *RB* and *RZ*, with whom I shared some truly unforgettable moments. Our friendship is one of the most precious achievements of this journey.

Finally, I am thankful for PolyMtl Engineering Physics department's administrative staff for supporting me in coordinating the purchase of the elements needed for the setup, for the technical staff who helped me in machining parts, for both PolyMtl and PoliMi Double Degree offices who provided assistance and guidance through this joint program, and for the creator of ComponentLibrary, Alexander Franzen, whose library has been a very useful tool for drawing optical setups.

RÉSUMÉ

Le développement intense que la technologie térahertz (THz) a connu au cours des dernières décennies a donné accès à de multiples techniques pour générer et détecter ces champs à basse fréquence. Un tel progrès est le résultat d'un effort considérable des chercheurs, encouragés par les nombreuses signatures spectrales moléculaires trouvées dans cette gamme et par la faible énergie portée par ces photons; caractéristiques qui sont exploitées dans diverses applications telles que la spectroscopie en domaine temporel, l'imagerie, les inspections non destructifs, etc. Outre l'échantillonnage électro-optique (EOS), une des stratégies les plus diffuses pour détecter de manière cohérente les champs THz, une autre approche a attiré de plus en plus d'attention ces derniers temps et consiste en la détection homodyne d'un signal défini *terahertz-field-induced second-harmonic* (*TFISH*). Contrairement à l'EOS, dont les spectres correspondants sont déformés en raison des interactions avec les phonons dans les cristaux, la détection basée sur *TFISH* n'est pas affecté par ce problème et le mélange avec un champ d'oscillateur local (LO) externe offre la possibilité de combler potentiellement l'écart entre détection THz classique et quantique, en donnant accès aux deux quadratures du champ électromagnétique.

L'objectif principal de ce travail était de concevoir, assembler et optimiser une configuration optique pour la détection résolue en champ des impulsions THz basée sur le processus *TFISH* dans des materiaux à l'état solide. Après avoir été générés via rectification optique (OR), une non-linéarité d'ordre deux, stimulée par une source laser à 1550 nm émettant des impulsions de 50 fs, les impulsions THz ont d'abord été caractérisés via EOS pour assurer un processus performant de génération et faciliter la réussite de la preuve-de-principe de détection du signal *TFISH*. Pour une détection efficace, il était nécessaire d'affiner les optiques de focalisation et de collimation et de sélectionner les matériaux appropriés pour le processus *TFISH* au travers des simulations numériques des conditions d'adaptation de phase.

La détection des ces champs à basse fréquence, générés via OR dans un substrat de ZnTe de 500 μm d'épaisseur, a été réalisée via un mélange linéaire du signal *TFISH* et un biais de seconde-harmonique, avec un bon rapport signal sur bruit (SNR de 25 avec un temps d'intégration de 500 ms pour chaque point de données) et incluant des composantes spectrales comprises principalement entre 0,5 et 2,5 THz, comparables à la bande passante obtenue avec la méthode EOS. Les distorsions de la trace temporelle, en particulier les oscillations de longue durée après l'impulsion principale, et l'apparition dans le spectre de chutes spectrales étroites, correspondant à certaines entre les plus fortes résonances de vapeur d'eau tabulées,

suggèrent que le champ THz excitait des modes de vibration des molécules de vapeur d'eau. En parallèle, des évaluations supplémentaires ont été réalisées pour montrer davantage la nature du processus *TFISH* en tant que phénomène non linéaire d'ordre trois.

Enfin, des mesures des deux quadratures du champ THz ont été accomplies avec succès en appliquant simplement une variation $\pi/2$ au terme de phase de l'interférence *TFISH-LO*, validant la potentialité de cette approche à être utilisée pour des applications quantiques.

ABSTRACT

The intense development that terahertz (THz) technology experienced during the last few decades gave access to multiple techniques to generate and detect these low-frequency fields. Such progress is the result of an extensive effort put by researchers, encouraged by the numerous molecular spectral signatures found within this range and by the low energy carried by these photons, features that are exploited in various applications such as time-domain spectroscopy, imaging, nondestructive inspections, etc. Besides electro-optic sampling (EOS), one of the most diffuse strategies to coherently detect THz transients, another approach has gained more and more attention lately and it consists in the homodyne detection of the so called terahertz-field-induced second-harmonic (TFISH) signal, induced by a four-wave mixing process. Conversely to EOS, whose corresponding spectra are distorted due to interactions with phonons in the crystals, the TFISH-based detection is "vibration-free" and the mixing with an external local oscillator (LO) field yields the opportunity to potentially bridge the gap between classical and quantum THz sensing, by giving access to both generalized quadratures of the electromagnetic field.

The main objective of this work was to conceive, assemble and optimize an optical setup for field-resolved detection of THz pulses based on the TFISH process in solid-state media. After being generated via optical rectification (OR), a second-order nonlinearity, driven by a 1550 nm laser source emitting 50 fs pulses, the THz transients were first characterized via EOS to set a benchmark of our THz source and to ensure a proper generation process, facilitating the successful proof-of-principle detection of the TFISH signal. For efficient detection, it was necessary to fine-tune the focusing and collection optics and to determine suitable materials for the TFISH process via numerical simulations of the corresponding phase matching conditions.

Detection of the low-frequency transients, generated via OR in a 500 μm thick ZnTe substrate, was achieved via linear mixing of the TFISH signal with a second-harmonic bias, with a decent signal-to-noise ratio (SNR of 25 with 500 ms integration time for each data point) and with spectral components comprised mainly between 0.5 and 2.5 THz, comparable with the bandwidth obtained via EOS measurements. Distortions in the temporal trace, particularly the long-lasting oscillations after the trailing edge, and the appearance in the corresponding spectrum of narrow spectral drops, matching some of the strongest tabulated water vapor resonances, suggested that the generated THz field excited some of the vibrational modes of water vapor molecules. In the meantime, additional evaluations were realized to further

show the nature of the TFISH process as a third-order nonlinear phenomenon.

Finally, measurements of both quadratures of the generated THz field were successfully carried out by simply applying a $\pi/2$ variation to the relative phase term of the TFISH-LO interference, validating the potentiality of this approach to be used for quantum applications.

TABLE OF CONTENTS

LIST OF TABLES

LIST OF FIGURES

LIST OF SYMBOLS AND ACRONYMS

ABCD	Air-biased coherent detection
BBO	Beta-barium borate
BPD	Balanced photodetector
BPF	Band-pass filter
BS	Beamsplitter
CaF_2	Calcium fluoride
CMOS	Complementary metal oxide semi-conductor
CW	Continuous wave
DC	Direct current
DFG	Difference-frequency generation
DX	Detection crystal
EOS	Electro-optic sampling
EOX	Electro-optic crystal
FROG	Frequency-resolved optical gating
FWHM	Full width at half maximum
FWM	Four-wave mixing
GaP	Gallium phosphide
GaSe	Gallium selenide
GD	Group delay
GDD	Group delay dispersion
Ge	Germanium
GUI	Graphical user interface
GVD	Group velocity dispersion
GX	Generation crystal
IA	Intensity autocorrelation
InGaAs	Indium gallium arsenide
IR	Infrared
$LiNbO_3$	Lithium niobate
LO	Local oscillator
LPF	Low-pass filter
mid-IR	Medium infrared
NA	Numerical aperture
near-IR	Near infrared

OAPM	Off-axis parabolic mirror
OPA	Optical parametric amplification
OR	Optical rectification
PBS	Polarizing beamsplitter
PC	Photoconductive
PD	Photodetector
SFG	Sum-frequency generation
SG	Supercontinuum generation
SHG	Second-harmonic generation
Si	Silicon
SiC	Silicon carbide
SNR	Signal-to-noise ratio
SPM	Self-phase modulation
SSBCD	Solid-state-biased coherent detection
TFISH	Terahertz-field-induced second-harmonic
THG	Third-harmonic generation
THz	Terahertz
THz-TDS	Terahertz time-domain spectroscopy
TL	Transform-limited
TOD	Third-order dispersion
UV	Ultraviolet
WLG	White-light generation
WP	Wollaston prims
Yb:KGW	Ytterbium-doped potassium gadolinium tungstate
ZnTe	Zinc telluride

LIST OF APPENDICES

CHAPTER 1   INTRODUCTION

1.1   General Introduction

Confined between the infrared and microwave frequency bands, the terahertz (THz) region is commonly defined as the portion of the electromagnetic spectrum between 0.1 and 30 THz (with 1 THz = 10^{12} Hz) [1–3]. Another historical definition for this range of frequencies is "THz gap" because up to the last few decades it has been rather inaccessible, mainly due to the lack of efficient sources and proper detectors.

Nevertheless, this spectral band is rich of scientific opportunities. Given its low photon energy, THz radiation is able to excite a multitude of fundamental spectral features like rotational and vibrational molecular transitions, lattice phonons in solids, energy bandgaps in superconductors and intraband excitations in semiconductors. Therefore, the THz band is of fundamental importance to allow characterization of condensed matter, not to mention the large number of applications that are developed on the basis of this low-frequency light [2]. Firstly, considering that the vibrational and rotational transitions are specific for each molecule, at the point that they effectively constitute a spectral fingerprint, it is possible to retrieve information relative to the composition of a specimen under investigation. This specificity opens the door to applications like diagnosis of diseases, sensing of biochemical agents, detection of atmospheric contaminants and pollutants, quality testing of aliments and pharmaceutics, etc. [1].

Notably, it is of particular interest the so called THz time-domain spectroscopy (THz-TDS), technique that yields the temporal dependence of both the amplitude and phase of the electric field, which is not achievable with typical detectors measuring only the intensity. Consequently, this approach, sometimes referred to as an "oscilloscope for light", gives direct access to the complex dielectric function of an analyte without demanding the resolution of the Kramers-Kronig relations [3, 4]. THz-TDS is realizable because the ultrafast pulses (in the order of few femtoseconds) emitted by the widely diffused visible to near-infrared (near-IR) laser sources, such as titanium sapphire lasers [5] or erbium-doped fiber lasers [6], grant perfect probing for the much longer (in the order of few picoseconds) oscillation cycle of a THz pulse [7, 8].

Another advantage of carrying low energies is that THz photons do not induce photoionization in biological tissues, conversely to X-rays, avoiding destruction of the sample. At the same time, due to the high absorption of water in the THz range [9], this radiation minimally

penetrates in the human body, making it a better-suited tool for imaging then microwaves [1], because even in the remote chance of causing some damage, it would be limited to the skin level. In addition, since this radiation is reflected by metals while transmitted by dielectric materials (e.g. paper, clothes, plastics, ceramics), it provides favorable contrasting properties for nondestructive inspection of sealed packages in the industrial and security fields. THz is also a highly attractive spectral region for telecommunication, in order to expand the portfolio of available frequencies and fulfill the constant need for larger bandwidth communication links. With a higher link directionality and a lower eavesdropping exposure, this spectral band is a potential candidate for the next generation of wireless communication technologies [10].

All the aforementioned considerations motivated the large research effort put in place to develop efficient sources, both continuous wave (CW) and pulsed, and detectors capable of filling this spectral gap [1–3]. Nowadays, an extensive collection of sources are available to cover the entire THz range, including Schottky diode mixers [11], gas lasers [12], quantum cascade lasers [13, 14]. A prominent class of few-cycle THz pulses sources is based on the conversion of femtosecond lasers via photoconductive (PC) switches [15, 16], via frequency-conversion in second-order nonlinear media like optical rectification (OR) and difference-frequency generation (DFG) [7, 17–19], or via two-colors driven laser-plasma [20, 21]. On the detection side, some of the most important strategies for resolving broadband THz fields exploit PC antennas [22, 23], electro-optic sampling (EOS) in nonlinear crystals [3, 17, 24] and third-order nonlinear processes in air [25–28], defined as terahertz-field-induced second-harmonic (TFISH) generation.

In particular, detection of THz transients via TFISH generated in solid-state media mixed with an optically-provided local oscillator (LO) field appears as a promising technique to extend the classical detection of this low-frequency fields to a full quantum tomography in the time domain [29]. Indeed, the possibility to independently control the optical properties of the LO field provides additional degrees of freedom, with respect to approaches like EOS, that help in achieving measurement of both generalized quadratures, which are essential to sample quantum fluctuations of the electromagnetic fields [30, 31].

1.2   Research Objectives

Immersed in an ever-growing laboratory approaching the crossroads between classical and quantum optics, this project is developed with the ambition to lay the groundwork for an experimental THz measurement system capable of demonstrating the "classical" functionality of tools needed for THz quantum applications. In particular, the main objective is to design, assemble and characterize an optical setup for field-resolved detection of THz pulses based

on a third-order nonlinearity in solid-state media. To this end, 50 fs pulses output by an optical parametric amplifier with central wavelength at 1550 nm are used as excitation source for generating low-frequency pulses via optical rectification (OR). Once generated, the THz transients are recombined with the probe beam in a properly chosen substrate to induce the nonlinear effect of terahertz-field-induced second-harmonic (TFISH). At this point, the THz field's amplitude and phase are temporally-resolved via linear mixing of the TFISH signal with a local oscillator (LO) field, obtained separately via second-harmonic generation. For such detection scheme to be successful, it is required to identify suitable materials for the TFISH process via phase matching numerical simulations, to optimize the focusing and collection conditions of the various beams and to analyze the experimental data to validate the aforementioned methodology.

1.3   Thesis Outline

The thesis begins with a presentation of the theoretical framework needed to understand the purpose and the working principle of the conceived optical system, including some of the fundamental concepts of laser pulse generation, characterization, propagation through dispersive media, and of nonlinear optical phenomena of the second and third-order. After a brief review of the main advantages and disadvantages of the various cutting-edge techniques for THz generation and detection, chapter 2 carries on with a depiction of the basics of optical rectification (OR), electro-optic sampling (EOS) and terahertz-field-induced second-harmonic generation (TFISH), being, respectively, the chosen strategies to generate (OR) and coherently-detect (EOS and TFISH) the THz transients. Then, the chapter concludes with a mathematical analysis of the diffraction and collection of the low-frequency beam and with some comments on the electronic detection methods. The main work is separated in two parts. Chapter 3 includes a description of the laser system employed as excitation source for the experiment and a detailed portrayal of the designed THz generation-detection setup. Afterwards, chapter 4 presents a first characterization of the generated THz fields via EOS, kept as a benchmark of the THz source and as a reference for optimizing the generation side of the system in order to facilitate the achievement of proof-of-principle detection of the THz transient via homodyne mixing of the TFISH signal. Following a preliminary analysis of the time-resolved traces and spectra, some of the expected features of this method are demonstrated, such as the quadratic dependence on the probe intensity and the possibility to control the phase of the TFISH-LO interference. Finally, in chapter 5, some limitations with potential solutions are discussed, together with interesting future improvements of the experimental setup.

CHAPTER 2   THEORY

2.1   Basic Treatment of Light Traveling through Media

The electromagnetic field associated to an electromagnetic wave propagating in free space is defined by two vector fields, the electric $\mathbf{E}(\mathbf{r}, t)$ and the magnetic $\mathbf{H}(\mathbf{r}, t)$ field, each function of position $\mathbf{r}$ and time t. These vectorial fields need to satisfy the wave equation, which is directly derived from Maxwell's equations [4]

$$\nabla^2 u(\mathbf{r}, t) - \frac{1}{c^2} \frac{\partial^2 u(\mathbf{r}, t)}{\partial t^2} = 0 \tag{2.1}$$

where the scalar function $u(\mathbf{r}, t)$ represents any of the three scalar components of the electric and magnetic fields. c is the speed of light in vacuum and is defined as

$$c = \frac{1}{\sqrt{\epsilon_0 \mu_0}} \tag{2.2}$$

with ϵ_0 and μ_0, respectively, the electric permittivity and the magnetic permeability of free space.

It can be shown [4] that the propagation of a wave traveling through dielectric, source-free (i.e. no free charges, no current sources) media, which will be the most recurring situation that will be treated in this work, is described by an equation similar to eq. 2.1, with the only difference being c replaced by the speed of light in the medium v, equal to

$$v = \frac{1}{\sqrt{\epsilon \mu}} \tag{2.3}$$

Here ϵ and μ are denoted as the electric permittivity and the magnetic permeability, respectively, of the considered medium and they are physical quantities that characterize the response of the medium to the incident light wave. In particular, they define the so called constitutive relations, which relate the polarization and magnetization densities, $\mathbf{P}$ and $\mathbf{M}$, on one side, and the electric and magnetic fields, $\mathbf{E}$ and $\mathbf{H}$, on the other. The polarization density $\mathbf{P}$ of a dielectric medium corresponds to the macroscopic sum of the microscopic electric dipole moments induced by the applied electric field. The same definition holds equivalently for the magnetization density $\mathbf{M}$. In the simplest case of a linear, non-dispersive,

homogeneous and isotropic dielectric medium [4], the electric permittivity ϵ is equal to

$$\epsilon = \epsilon_0 \left(1 + \chi\right) \tag{2.4}$$

with χ defined as the electric susceptibility of the medium. In this very particular case χ is a constant scalar quantity. However, as soon as we remove some of the conditions listed above, the electric susceptibility becomes a more complicate physical quantity. In the following, we remove such conditions one by one to understand their effect on χ:

- non-homogeneous medium: χ becomes function of the position $\mathbf{r}$, $\chi = \chi(\mathbf{r})$

- anisotropic medium: χ is now described by a tensor, $\chi = \{\chi_{ij}\}$, because the properties of the medium depend on the direction of the incident electric field $\mathbf{E}$

- dispersive medium: the medium response to the excitation of $\mathbf{E}$ is not instantaneous, hence χ becomes function of frequency, $\chi = \chi(\omega)$

We have not yet discussed the actual solutions of the wave equation, presented in eq. 2.1. The simplest functions that satisfy the wave equation are monochromatic waves, which are harmonic functions. Their wave function $u(\mathbf{r}, t)$ can be expressed as the real part of the following complex function $U(\mathbf{r}, t)$

$$U(\mathbf{r}, t) = a(\mathbf{r})e^{i\Phi(\mathbf{r})}e^{-i\omega t} \tag{2.5}$$

where $a(\mathbf{r})$ describes the amplitude of the wave, $\Phi(\mathbf{r})$ represents the phase and $\omega = 2\pi\nu$ the angular frequency of the oscillation. Since these wavefunctions represent perfect sinusoids that extend in time from $-\infty$ to $+\infty$, they cannot describe a real physical wave because they would carry infinite energy. Nevertheless, they constitute very useful tools to represent arbitrary waveforms, because they form a complete set of orthogonal functions, and thus an orthonormal basis. As a consequence, a real polychromatic wave, which is non-harmonic, can be described as a superposition of monochromatic waves: an arbitrary wavefunction $u(\mathbf{r}, t)$ at a fixed position $\mathbf{r}$ can be expressed as

$$u(t) = \frac{1}{\sqrt{2\pi}} \int_{-\infty}^{+\infty} s(\omega)e^{-i\omega t}d\omega, \quad s(\omega) = \frac{1}{\sqrt{2\pi}} \int_{-\infty}^{+\infty} u(t)e^{i\omega t}dt \tag{2.6}$$

where $s(\omega)$ is the Fourier transform of $u(t)$.

Following what discussed above, it is evident that light does not travel in a medium at the same speed as when in vacuum. To measure the extent to which its speed is modified, it is

useful to introduce the medium's refractive index n as the ratio between the speed in vacuum and the speed in the medium

$$n = \frac{c}{v} = \sqrt{\frac{\epsilon}{\epsilon_0}\frac{\mu}{\mu_0}} \qquad (2.7)$$

Generally, the refractive index is a complex number: the real part causes a change in the phase of the wave, while the imaginary part, usually called extinction coefficient κ, represents the attenuation that light undergoes while traveling through the medium. Indeed, according to the Beer-Lambert's law [4], the intensity of a wave that travels for a distance z inside an absorptive medium presents an exponential decay

$$\frac{I(z)}{I_0} = e^{-\frac{2\kappa\omega}{c}z} \qquad (2.8)$$

Real and imaginary parts of the electric susceptibility, and hence of the refractive index, are intimately interconnected via the Kramers-Kronig relations [4], which constitute a special Hilbert-transform pair and they are a direct consequence of the causal nature of the medium response function. This implies that it is possible to retrieve the refractive index real part from the imaginary one, or viceversa, providing a very powerful tool, as it will be discussed in the next section in the context of dispersive materials.

In addition, it is interesting to study how light behaves when it travels across media with different properties. At the boundary between two media characterized by two different refractive indices, n_1 and n_2, a ray of light is split in two parts. One is reflected by the
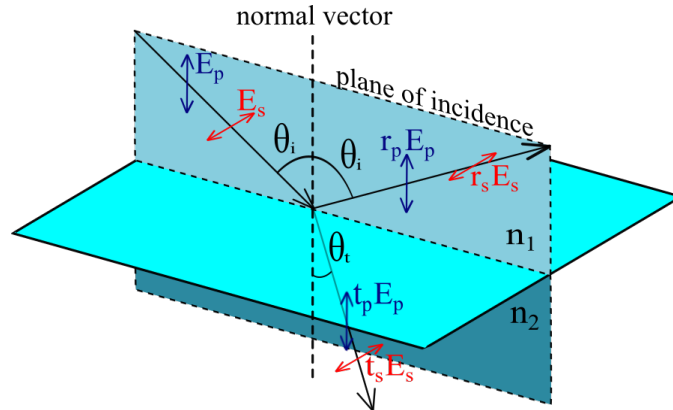

Figure 2.1 Behavior of a light wave at the interface between two media with refractive indices $n_1 < n_2$. θ_t is determined by Snell-Descartes' law, while $r_{s,p}$ and $t_{s,p}$ are the Fresnel coefficients for the reflected and transmitted s- and p-polarization components of the incident electric field, E_s and E_p, respectively.

surface and its direction lies in the same plane of incidence, which is the plane formed by the incident ray and the vector normal to the surface at the point of incidence, with an angle with respect to the normal equal to the incidence angle (see fig. 2.1). The other is transmitted, or refracted, and the direction obeys Snell-Descartes' law

$$n_1 \sin(\theta_i) = n_2 \sin(\theta_t) \tag{2.9}$$

with θ_i and θ_t being the incident and transmitted angles, respectively, in regard to the normal to the surface.

The amount of light that is reflected and transmitted depends on the polarization of the incoming light, on the direction of the incident and transmitted rays and on the optical properties of the media, in particular their refractive indices n_1 and n_2 . The reflected (r_s, r_p) and transmitted (t_s, t_p) electric field amplitudes normalized to the one of the incident field are determined by the Fresnel coefficients [32]

$$
\begin{aligned}
r_s &= \frac{n_1 \cos(\theta_i) - n_2 \cos(\theta_t)}{n_1 \cos(\theta_i) + n_2 \cos(\theta_t)}, \quad r_p = \frac{n_2 \cos(\theta_i) - n_1 \cos(\theta_t)}{n_2 \cos(\theta_i) + n_1 \cos(\theta_t)} \\
t_s &= \frac{2 n_1 \cos(\theta_i)}{n_1 \cos(\theta_i) + n_2 \cos(\theta_t)}, \quad t_p = \frac{2 n_1 \cos(\theta_i)}{n_2 \cos(\theta_i) + n_1 \cos(\theta_t)}
\end{aligned}
\tag{2.10}
$$

where s and p indicate the two sets of linear polarization components of the incident wave: s-polarization refers to the polarization perpendicular to the plane of incidence, while p-polarization represents the field component parallel to the plane of incidence (see fig. 2.1).

Then, it is straightforward to compute the power reflection R and transmission T coefficients starting from the amplitude coefficients [32]

$$R_{s,p} = |r_{s,p}|^2, \quad T_{s,p} = 1 - R_{s,p} = \frac{n_2 \cos(\theta_t)}{n_1 \cos(\theta_i)} |t_{s,p}|^2 \tag{2.11}$$

2.1.1 Pulse Propagation in Dispersive Media

According to what discussed in the previous section, a pulse of light comprises a sum of many monochromatic waves and the simplest way to represent its electric field (which is taken as a scalar in the following for convenience) in the time domain, when propagating through non-dispersive media, is as a time-varying envelope function $a(t)$ multiplied by a fast oscillatory term at the central optical frequency ω_0

$$E(z,t) = Re\left\{ a\left(t - \frac{nz}{c}\right) e^{-i\omega_0\left(t - \frac{nz}{c}\right)} \right\} = Re\left\{ a\left(t - \frac{nz}{c}\right) e^{i(\Phi(z) - \omega_0 t)} \right\} \tag{2.12}$$
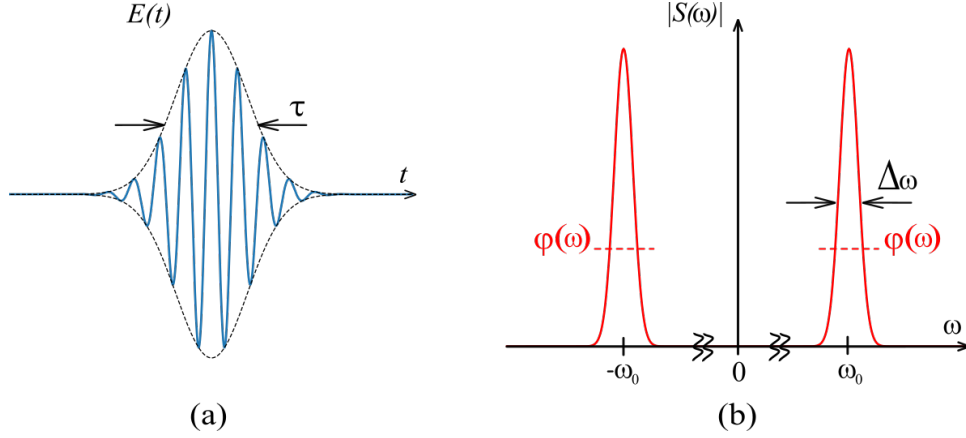
Figure 2.2 Temporal and spectral representations of a light pulse. (a) Electric field dependence on time, at a fixed position z, of a pulse with Gaussian-like envelope of duration τ. (b) Magnitude of the corresponding Fourier transform, characterized by the two strong components centered at $\pm\omega_0$ with FWHM equal to $\Delta\omega$ and with flat spectral phase $\varphi(\omega)$.

The corresponding Fourier transform is

$$S(z,\omega) = A(\omega - \omega_0)e^{i\omega nz/c} = A(\omega - \omega_0)e^{i\varphi(\omega)} \tag{2.13}$$

with $A(\omega)$ the Fourier transform of $a(t)$ and $\varphi(\omega)$ the spectral phase. In fig. 2.2 we include the representation in time and frequency domain of a pulse with duration τ, intended as the full width at half maximum (FWHM). The envelope function generally varies more slowly with respect to an optical cycle, hence its Fourier transform presents a spectral FWHM $\Delta\omega$ much smaller than the central frequency ω_0. Furthermore, $\Delta\omega$ is related to the pulse temporal duration τ via the so called time-bandwidth product

$$\tau\frac{\Delta\omega}{2\pi} \geq a \tag{2.14}$$

where a is a constant value that changes based on the pulse envelope shape (e.g. for Gaussian-like pulses $a \approx 0.441$, for hyperbolic-secant-like pulses $a \approx 0.315$ [33]). This means that for a given spectral bandwidth it exists an inferior limit to the minimal pulse duration that can be attained. Such a pulse is defined as Fourier-transform-limited, or simply as transform-limited.

When the pulse propagates through a linear, homogeneous, isotropic, non-magnetic and dispersive medium, each frequency component of the pulse spectrum experiences a different

refractive index $n(\omega)$ (putting together eqs. 2.4 and 2.7)

$$n(\omega) = \sqrt{\frac{\epsilon}{\epsilon_0}} = \sqrt{1 + \chi(\omega)} \tag{2.15}$$

and therefore it travels with a different phase velocity, defined as

$$v(\omega) = \frac{c}{n(\omega)} \tag{2.16}$$

The phase velocity is the speed at which the phase of any frequency component propagates through the medium. On the other hand, the envelope of the wave (which defines the packet of light) travels with a different speed, known as group velocity, and given by

$$v_g(\omega_0) = \left[\frac{dk(\omega)}{d\omega}\bigg|_{\omega_0}\right]^{-1} \tag{2.17}$$

where $k(\omega) = \omega n(\omega)/c$ is the frequency-dependent wave vector, which is a measure of the phase delay per unit length and it generally points in the direction of the wave propagation. Looking at eq. 2.17, we realize that the group velocity might vary with frequency if spectral dependence of $n(\omega)$ is quadratic or of higher order. It is of use to introduce the group index as

$$n_g(\omega_0) = \frac{c}{v_g} = c\frac{dk(\omega)}{d\omega}\bigg|_{\omega_0} = n(\omega_0) + \omega_0\frac{dn(\omega)}{d\omega}\bigg|_{\omega_0} \tag{2.18}$$

or, alternatively, in terms of wavelength as

$$n_g(\lambda_0) = n(\lambda_0) - \lambda_0\frac{dn(\lambda)}{d\lambda}\bigg|_{\lambda_0} \tag{2.19}$$

The phenomenon for which phase and group velocities are frequency-dependent is known as chromatic dispersion and it has to be taken into great consideration if we want to obtain transform-limited pulses, which is true in the majority of cases. Indeed, the minimum pulse duration is achieved only when the spectral phase $\varphi(\omega)$ is constant or linear, or in other words, when it does not include quadratic or higher order dependence on the angular frequency ω. The spectral phase accumulated by the pulse after traveling for a distance L in a dispersive medium is linearly proportional to the wave vector, $\varphi(\omega) = k(\omega)L$. For this reason, a useful way to characterize the chromatic dispersion is by writing the wave vector in terms of its Taylor series expansion

$$k(\omega) = k(\omega_0) + \frac{\partial k}{\partial \omega}\bigg|_{\omega_0}(\omega - \omega_0) + \frac{1}{2}\frac{\partial^2 k}{\partial \omega^2}\bigg|_{\omega_0}(\omega - \omega_0)^2 + \frac{1}{6}\frac{\partial^3 k}{\partial \omega^3}\bigg|_{\omega_0}(\omega - \omega_0)^3 + \cdots \tag{2.20}$$

The zero-order term is constant and it causes a simple phase shift. The first-order term can be recognized from eq. 2.17 as the inverse of the group velocity v_g and it represents the overall time delay that the pulse accumulates when traveling through the material. For this reason, this term multiplied by the length L is defined as the group delay GD

$$GD = \left.\frac{\partial \varphi}{\partial \omega}\right|_{\omega_0} = L \left.\frac{\partial k}{\partial \omega}\right|_{\omega_0} = \frac{L}{v_g} \tag{2.21}$$

Neither of these terms affects the pulse shape. On the other hand, the second-order term is the first term of eq. 2.20 that has an impact on the pulse duration, in particular it elongates the pulse with respect to its transform-limited duration. This term is the derivative of the GD per unit length and is defined as group velocity dispersion GVD

$$GVD = \left.\frac{\partial^2 k}{\partial \omega^2}\right|_{\omega_0} = \left.\frac{\partial}{\partial \omega}\left(\frac{1}{v_g}\right)\right|_{\omega_0} \tag{2.22}$$

Hence, the GVD expresses the delay per unit length accumulated by each frequency component. From another point of view, with a non-zero GVD, each component arrives at different moments because they do not travel with the same group velocity inside the material. It follows that the instantaneous frequency depends on time, $\omega(t) = \frac{d\Phi(t)}{dt}$, and the pulse is said to be chirped. Fig. 2.3 depicts a temporal representation of a TL pulse that travels through a material with null, positive and negative GVD, respectively, highlighting the effect of an up-chirp and a down-chirp on the original TL pulse.

Similarly to what done above with the GD, it is useful to introduce the group delay dispersion GDD as

$$GDD = \left.\frac{\partial^2 \varphi}{\partial \omega^2}\right|_{\omega_0} = L \left.\frac{\partial^2 k}{\partial \omega^2}\right|_{\omega_0} = L \cdot GVD \tag{2.23}$$

Concerning the higher order terms in the Taylor expansion, they all induce different variations in the pulse shape depending on the order. It is now clear why recurring to the Taylor expansion is useful: starting from the refractive index curve as a function of frequency, in principle, for any media we can compute the expected effect of dispersion on the pulse propagation up to the interested order.

In the previous section we briefly discussed Kramers-Kronig relations and how they interconnect real and imaginary part of the refractive index. A consequence of these formulas is that media whose refractive index is wavelength dependent, i.e. dispersive media, must be absorptive and showing an extinction coefficient that also depends on the wavelength. This is important because it determines that the dispersion is particularly strong close to a resonance of the medium, which corresponds to a spectral region presenting an absorption
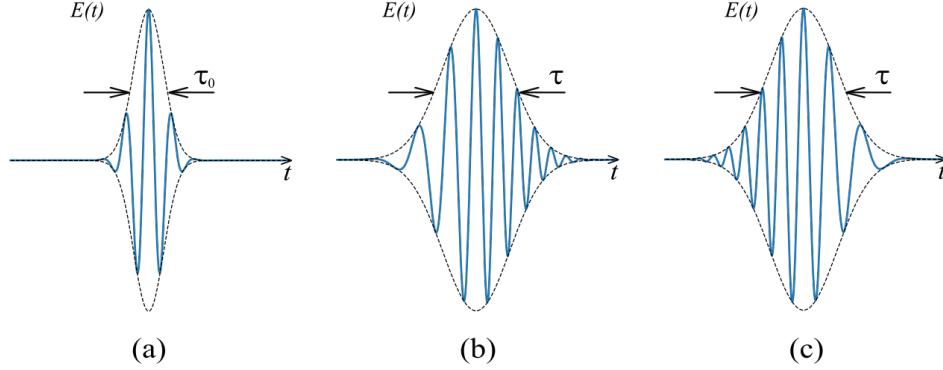
Figure 2.3 Time domain representation of the effect of a linear chirp, positive and negative, on a Gaussian-like transform-limited pulse. (a) Gaussian-like TL pulse with duration τ_0. (b) Pulse resulting from propagation through a medium with positive GVD: the duration of the up-chirped pulse is larger and it is evident that the instantaneous frequency is time-dependent, with higher frequencies arriving later because of the normal dispersion in the medium. (c) Down-chirped pulse: the anomalous dispersion, i.e. $GVD < 0$, makes lower frequencies appear on the trailing edge of the pulse. In terms of the envelope width τ, it is the same in (b) and (c) because it only matters the absolute value of the chirp, not the sign.

peak. On the other hand, the dispersion is weak far from the resonance. For this reason, most materials that are transparent in the visible region while presenting resonances in the ultraviolet (electronic resonances) and in the infrared (nuclei vibrations), exhibit a similar dispersion behavior [34]. Away from the absorption peaks, the refractive index increases with frequency and GVD is positive, hence the group velocity is smaller than the phase velocity. This behavior is defined normal dispersion. Conversely, within the resonance regions, the refractive index decreases with frequency and the material presents negative GVD, originating the terminology anomalous dispersion. This confirms what presented in fig. 2.3: in the case of an up-chirp ($GVD > 0$), higher frequencies are on the pulse trailing edge because they arrive later, while the opposite happens in the case of a down-chirp ($GVD < 0$).

2.2   Generation of Ultrashort Pulses

Ultrafast pulses are undoubtedly one of the most brilliant achievements of the last few decades and a key ingredient for this work. With their extremely high peak powers (up to 10^{15} W) and peak intensities (exceeding 10^{20} W/cm^2), they are useful for multiple applications, including time-resolved spectroscopy, frequency metrology, nonlinear optics (see section 2.4), biomedical applications, material processing, and many others [34, 35]. A clear identification of ultrafast pulses, also called ultrashort pulses, is not available, but generally they refer to

laser pulses whose duration ranges from few femtoseconds (1 fs $= 10^{-15}$ s) to few tens of picoseconds (1 ps $= 10^{-12}$ s).

A very trivial way to obtain pulsed light from a laser is to employ a continuous-wave (CW) laser and an external modulator, like a switch. A CW laser is a laser source that is continuously pumped and it continuously emits light. The conjunction of such laser and modulator results in the transmission of light only during short time intervals (ON-period), provided that a fast-enough modulator is available. It is immediate to deduct that this simple scheme presents some important disadvantages: the pulses peak power is the same as the steady power of the CW laser, making them useless for the applications mentioned above, and a lot of energy is wasted because the light energy that is blocked by the modulator is dumped during the OFF-periods and not recovered by the system, making it inefficient. Not to mention that modulators able to provide on-off switch on femtosecond timescale do not exist. Therefore, we understand that to efficiently produce ultrafast pulses, the lasing source itself has to be turned on and off via an internal modulator. This way, during the OFF-periods the energy is stored either in the form of light in the laser cavity either in the form of population difference in the atomic system, leading to very intense and short light pulses.

In particular, there are principally four schemes able to internally modulate the laser light and achieve high peak powers [4]: gain switching, Q-switching, cavity dumping and mode locking. In gain switching, as the name suggests, the modulation is executed directly on the laser pump, which affects the population inversion and thus the gain. For instance, when the laser pump is a flashlamp, the modulation is achieved by driving the lamp with a sequence of electrical pulses. Q-switching consists in periodically increasing the losses of the laser cavity by introducing a modulated absorber. In other words, the resonator quality factor Q, which is proportional to the ratio of energy stored in the resonator to the energy dissipated per oscillation cycle, is modulated by keeping constant the pumping while periodically increasing the cavity losses. As a result, during the OFF-periods energy is stored under the form of population inversion in the active medium and, as soon as the loss coefficient is brought below the gain coefficient, the accumulated energy is released as an intense burst of light, with durations generally in the order of the nanoseconds. Cavity dumping is a pulsing scheme that is also based on energy accumulation and sudden release in the form of short pulses. However, it is different from Q-switching because the energy is stored in the form of photon density inside the cavity instead of atomic population difference, and the cavity losses are modulated by varying the output mirror's transmittance: when the end mirror is completely reflective photons cannot escape and are stored in the resonator, until the end mirror is removed (i.e. full transmission) and the laser energy gets released as a strong pulse

of light. Normally, the pulse durations obtained with this scheme are of the same order of magnitude as for *Q*-switching. Finally, mode locking is the one technique among these four able to achieve periodic trains of ultrashort pulses with highest repetition rates, in the order of hundreds of kilohertz (kHz) to tens of megahertz (MHz), and shortest duration, ranging between picoseconds and femtoseconds.

Before we explain the working principle behind this scheme it is fundamental to introduce the concept of longitudinal modes. Let us consider for simplicity a Fabry-Pérot cavity, i.e. an optical cavity made up by two mirrors facing each other. Light bouncing back and forth on the mirrors interferes in a constructive and destructive fashion, giving rise to standing waves between the cavity extremities. These standing waves are a consequence of the constructive interference and they are defined as the cavity longitudinal modes. They constitute the discrete set of the sole frequencies allowed to oscillate in the cavity, since all the other frequencies do not survive due to the destructive interference. The spectral spacing between each mode, known as Fabry-Pérot intermodal spacing f_{FP}, is fixed by the cavity length L
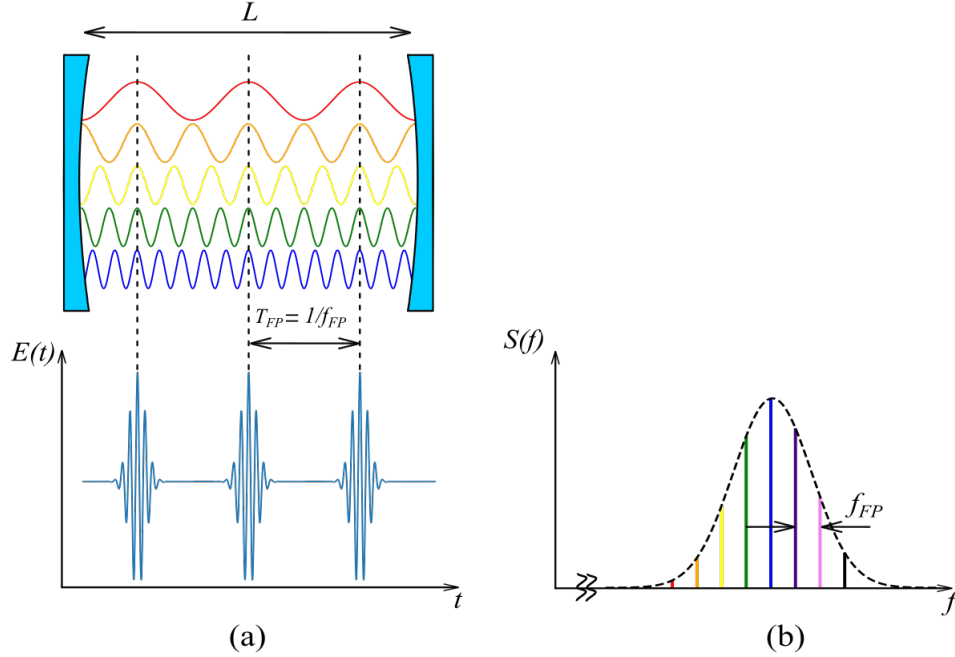
Figure 2.4 Mode locking working principle. (a) The fixed phase relationship between the longitudinal modes sustained by the Fabry-Pérot cavity with length L results in constructive interference and the periodic emission of intense ultrashort pulses, with period T_{FP}. (b) Representation in the spectral domain of the longitudinal modes that are located within the gain curve of the laser medium, separated between each other by f_{FP}.

$$f_{FP} = \frac{c}{2L} \tag{2.24}$$

Now, each longitudinal mode oscillates independently with its own individual phase and the resulting laser output may be constant or randomly vary due to the nature of the modal interference, sometimes constructive and some others destructive. On the other hand, when all modes are coupled together and their phases are locked together, i.e. there is a fixed relationship between the phase of each mode, the laser outputs very intense periodic bursts of light, resulting from the constructive interference of the longitudinal modes. The time separation T_{FP} between two consecutive pulses is inversely proportional to the intermodal spacing f_{FP}, and hence it directly depends on the cavity length L [4].

There are multiple methods used to lock the phase of the modes and they can be separated in two main categories, active and passive mode locking, depending whether the optical modulator placed inside the cavity is, respectively, controlled or not by an external signal. For instance, active mode locking is achieved by placing an acousto-optic or electro-optic switch inside the resonator. If such a switch is modulated at a frequency equal to the intermodal spacing f_{FP}, then its action generates sidebands of the original optical field that are in-phase and spaced exactly by the intermodal separation. It follows that the CW operation is destroyed due to a transfer of power into coherent sidebands. From a time domain perspective, the modulator acts as a periodic shutter synchronized with the pulse round-trip transit time $T_{FP} = 2L/c$ [34]. Even though active mode locking is a rather common and established technique, it presents a couple of drawbacks. First, there is a lower limit to the achievable pulse width because the pulse shortening action induced by the external modulator becomes ineffective for very short pulse duration. Second, the requirement of a very precise externally-driven modulator, since the modulation frequency has to be accurately set to match the intermodal spacing, imposes some serious constraints on the design of the mode locked laser.

These downsides can be avoided by exploiting passive mode locking methods, which replace the external modulator with certain nonlinear optical elements, whose losses are intensity-dependent. In particular, the element can be chosen in such a way that the losses for pulsed operation are lower, which can be achieved either by material loss or through modal loss for CW operation. This way, only the ultrashort pulse generated by the in-phase oscillations can survive and all the other random phase combinations are suppressed by the higher losses. In addition, provided that the response time of the nonlinearity is fast enough, this modulation gets faster as the pulse becomes shorter, hence very short pulses can be obtained.

Examples of passive mode locking strategies include the use of a saturable absorber, whose absorption decreases with intensity or energy, or the implementation of a Kerr-lens mode

locking. The latter method takes advantage of the optical Kerr effect, that is a nonlinear phenomenon causing the refractive index to depend on the intensity (more details in subsection 2.4.2), within a proper Kerr material put inside the cavity. As a result, the medium acts as a lens, inducing tighter spatial focusing for higher intensity modes, which are isolated from the others by placing a sufficiently small aperture in the focal plane of the Kerr-lens. Similarly, the Kerr effect can take place within the gain medium itself and the phase-locked modes are selected by increasing their overlap with the strongly-focused pump laser, leading to a larger gain [4].

2.3   Pulse Characterization

The large majority of the applications presented at the beginning of the previous section, requiring ultrafast laser pulses as excitation source, need to know the actual duration of those pulses in order to work as intended. For instance, in nonlinear optics it is fundamental to reach certain peak intensities to drive the desired nonlinear phenomenon, but if the intensity is too high, i.e. above the damage threshold of the used material, the medium risks to be irreversibly damaged.

Unfortunately, the duration of pulses on the femtosecond time scale cannot be retrieved by measuring the time dependence of the intensity with a photodetector. Indeed, even the state-of-the-art photodetectors are not able to resolve such short pulses, being limited by the response time of the carriers. Similarly, a linear autocorrelator, such as a Michelson interferometer [4], does not provide information on the pulse duration [34]. One of the simplest methods of pulse duration characterization which overcomes this limitation is the intensity autocorrelation (IA) [34], which requires the presence of a nonlinear element. Basically, a Michelson interferometer is employed to split the pulse in two identical copies which are successively recombined with a relative time delay τ in a nonlinear crystal, generally a second-harmonic generation (SHG) crystal (more details in section 2.4). Then, the resulting average second-harmonic power is recorded with a slow time-averaging detector as a function of τ. This way, we take advantage of the short duration of the pulse, which is often the shortest event available, to get a sufficiently high time resolution to obtain an approximation of the pulse width. The trace $I_{IA}(\tau)$ obtained with this experiment, also defined as optical intensity autocorrelation, can be expressed as

$$I_{IA}(\tau) = \int_{-\infty}^{\infty} I(t)I(t-\tau)dt \tag{2.25}$$

It is trivial to realize that the pulse FWHM $\Delta\tau_p$ is directly related to the autocorrelation one

$\Delta\tau_{IA}$: however, to retrieve a precise value it is required to make an a priori assumption on the pulse envelope shape. For example, for a Gaussian-like pulse we have $\Delta\tau_p = \Delta\tau_{IA}/\sqrt{2}$. Since the assumption can be more or less correct, the intensity correlation can only yield an estimation of the duration. Furthermore, this method does not provide any information on the spectral amplitude nor on the spectral phase, which are generally required to properly execute experiments in the ultrafast realm [34].

One could rightfully think that the pulse width can be retrieved by measuring the spectral amplitude of the source with a spectrometer, since spectral width and the temporal duration are intrinsically related via the time-bandwidth product, as introduced in subsection 2.1.1. However, such an approach gives only an indication of the transform-limited FWHM duration, which in a real situation does not match the actual duration because of the presence of dispersion. In addition, since the spectrometer gives no information on the spectral phase, there is no way of characterizing the dispersion terms and retrieve the real duration. At this point it is clear that a method able to retrieve both spectral amplitude and phase allows to fully characterize a pulse. That is where techniques operating in the time-frequency domain come into play [36]. Those approaches take advantage of the combination of the two domains, instead of operating in one of the two separately, which happens in the case of autocorrelators and spectrometers. Among them, one technique that has stood out for its reliability, ease of employment and universality is called frequency-resolved optical gating (FROG), introduced in 1991 by Rick Trebino and Daniel J. Kane [37].

There exists a whole portfolio of FROG implementations depending on the nonlinear interaction exploited for the self-referencing of the pulse [36]. Among these different geometries, the most common one, presenting the largest sensitivity and accuracy, is known as SHG-FROG because it employs second-harmonic generation to yield the nonlinear autocorrelation signal. The setup is still somehow related to a Michelson interferometer, but the two copies of the pulses are recombined by making them focus and spatially overlap inside a second-order nonlinear crystal. If the recombination happens in a non-collinear fashion it is possible to spatially select only the contribution derived from the nonlinear mixing of the two relative delayed replicas, and record it with a spectrometer. As a result, the generated second-harmonic is spectrally resolved for each time delay τ, resulting in a complete spectrogram, also called FROG trace

$$I_{FROG}(\omega,\tau) = \left| \int_{-\infty}^{\infty} E_{sig}(t,\tau)e^{-i\omega t}dt \right|^2 \qquad (2.26)$$

where $E_{sig}(t,\tau)$ depends on the chosen geometry, hence in the SHG-FROG case

$$E_{sig}(t,\tau) = E(t)E(t-\tau) \tag{2.27}$$

It can be shown that the spectrogram indirectly contains all the information required to fully reconstruct the pulse field, i.e. its intensity and phase. The procedure to recover those physical quantities starting from the FROG trace is not trivial and it is based on approximate iterative retrieval algorithms. Indeed, the mathematical problem that needs to be solved, known as 2D phase retrieval problem, does not present a direct inverse [36]. Nevertheless, very powerful retrieval algorithms are nowadays available and SHG-FROG leads to a full characterization of the pulse and its distortions, without requiring assumptions on the pulse shape as in the case of IA.

2.4 Nonlinear Optics

The invention of laser sources emitting ultrashort pulses (see section 2.2) gave access to a new realm of phenomena that occur only in the presence of very high intensities, such as the generation of new colors from monochromatic sources of light, or the self-focusing of a beam inside a homogeneous medium [38]. Nonlinear optics is the branch of optics responsible to study and understand these complex events, and it constitutes one of the topics at the core of this project.

To describe ordinary effects of light propagating through materials such as reflection, refraction, diffraction, scattering, etc., it is sufficient to introduce some parameters (for example the index of refraction) that are independent of the intensity of light. This is the linear regime of optics. On the other hand, with the high intensities capable of inducing nonlinear phenomena in the material, those parameters cannot be considered constant, but they become a function of the light intensity. For this reason, it is defined as "nonlinear" optics, because the optical properties of the materials depend in a nonlinear manner on the strength of the applied optical field [35]. The theory of nonlinear optics is developed starting from the well-understood model of linear optics and it exploits a similar concept of light-matter interaction: as mentioned in section 2.1, the material response to the excitation of light is characterized by the polarization density, P(t). In the linear regime, the induced polarization is linearly proportional to the electric field strength

$$P(t) = \epsilon_0 \chi^{(1)} E(t) \tag{2.28}$$

where $\chi^{(1)}$ is the linear susceptibility of the material. It can be noticed that in eq. 2.28 the induced polarization at time t depends instantaneously on the applied field, which is true only with the assumption that the medium is lossless and dispersionless.

Assuming that the strength of the applied field $E(t)$ is not enough to ionize matter (a regime known as non-perturbative nonlinear optics, which will not be treated because out of the scope of this work), it is possible to express the induced polarization of the medium as a power series of the electric field

$$P(t) = \epsilon_0 \left[\chi^{(1)} E(t) + \chi^{(2)} E^2(t) + \chi^{(3)} E^3(t) + ... \right] \equiv P^{(1)}(t) + P^{(2)}(t) + P^{(3)}(t) + ... \quad (2.29)$$

with $\chi^{(2)}$ and $\chi^{(3)}$, respectively, the second and third-order nonlinear optical susceptibilities. For simplicity, in this equation it was assumed that the fields $P(t)$ and $E(t)$ are scalar quantities since it is already enough to demonstrate the appearance of nonlinear effects. A complete vectorial analysis of the fields would show that the susceptibilities $\chi^{(i)}$ are tensors of rank $i + 1$.

The fact that the induced polarization $P(t)$ is expressed as a power series also implies that the higher is the order of the interested nonlinearity, the higher the field value must be in order for this effect to become relevant. Finally, the presence of even and odd orders of the nonlinear polarization $P(t)$ is dictated by the symmetry of the nonlinear medium: even order (i.e. second, fourth, etc.) nonlinear interactions can occur only for non-centrosymmetric materials, meaning those media that do not possess inversion symmetry, while odd order interactions can happen for both centrosymmetric and non-centrosymmetric materials.

This property can be qualitatively shown by describing the nonlinear optical properties via an extended version of the Lorentz model, which is known to describe very well the linear optical properties [35]. The model for the linear optical regime considers the atom as a harmonic oscillator and the restoring force $F_{rest}(x)$ contains only a term linearly proportional to the electron displacement x. Similarly, in the "extended" Lorentz model, F_{rest} is still related to the electron displacement, but this time it is expressed as a Taylor expansion series of the displacement, adding therefore the possibility of having also nonlinear terms.

Now, the restoring force is related to a potential energy function $U(x)$ defined as

$$U(x) = -\int F_{rest}(x) dx \quad (2.30)$$

and here is where the symmetry of the medium comes into play: centrosymmetric materials admit a potential energy function containing only even order terms, hence the restoring force includes only odd order terms. Consequently, only odd order optical nonlinearities

are present, while even order ones are absent. Conversely, for non-centrosymmetric media $U(x)$ comprises both even and odd order powers of the displacement, implying that optical nonlinearities of even and odd order might occur.

2.4.1 Second-Order Nonlinearities

The second component of the induced polarization described in eq. 2.28 is responsible for the appearance of second-order nonlinearities. By considering a field $E(t)$ given by the superposition of two monochromatic waves at frequency ω_1 and ω_2

$$E(t) = \frac{1}{2}E_1 e^{-i\omega_1 t} + \frac{1}{2}E_2 e^{-i\omega_2 t} + c.c. \tag{2.31}$$

it's possible to show how the nonlinear response of the material generates new frequencies, different from the input ones

$$
\begin{aligned}
P^{(2)}(t) = {} & \frac{1}{4}\epsilon_0\chi^{(2)} \left[E_1^2 e^{-i2\omega_1 t} + E_2^2 e^{-i2\omega_2 t} + 2E_1 E_2 e^{-i(\omega_1+\omega_2)t} + 2E_1 E_2^* e^{-i(\omega_1-\omega_2)t} + c.c. \right] \\
& + \frac{1}{2}\epsilon_0\chi^{(2)} \left[E_1 E_1^* + E_2 E_2^* \right] e^0
\end{aligned}
\tag{2.32}
$$

Narrowing the attention to the exponents of the complex exponential terms, five new frequencies components appeared, and each one is the result of a different physical phenomenon:

- $2\omega_1, 2\omega_2$: second-harmonic generation (SHG)

- $\omega_1 + \omega_2$: sum-frequency generation (SFG)

- $\omega_1 - \omega_2$: difference-frequency generation (DFG)

- 0 : optical rectification (OR)

In order to understand the nature of these phenomena, let us consider each interaction in terms of a photon exchange between the different frequency components and represent the material as a simple two-level system, as depicted in fig. 2.5. In each scheme, the solid line depicts the ground state while the dashed line represents a virtual state. There is an important physical difference between those states: the ground state is an *eigenstate* of the isolated atom, whereas the virtual states result from a combination of the energy *eigenstates* of the atom and of one or more photons of the incoming radiation field.

In the SHG, two photons at frequency ω are annihilated and a photon at higher frequency is created in a single quantum-mechanical process. SFG is an almost identical process, except
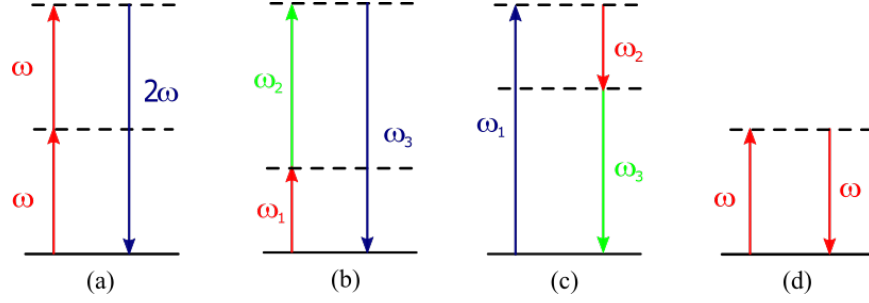
Figure 2.5 Energy-level diagrams for $\chi^{(2)}$ phenomena. (a) Second-harmonic generation. (b) Sum-frequency generation. (c) Difference-frequency generation. (d) Optical rectification.

for the fact that the two destroyed photons are at different frequencies, hence they come from different sources and not from the same source as in SHG. Moving to the DFG, a higher frequency photon is decomposed into two photons at lower frequencies. This process is of particular interest when a strong field at higher frequency and a weaker signal at lower frequency are incident on a $\chi^{(2)}$ medium. According to the photon energy-level description of DFG (see fig. 2.5), the atom is firstly excited to the highest virtual level via the absorption of the photon at high frequency ω_1, and then it decays by a two-photon emission process that is stimulated by the other incoming photon at frequency ω_2. As a result of the energy conservation, for every created photon at the difference frequency ω_3 from the annihilation of a high frequency photon (ω_1), another low frequency photon (ω_2) must be created. Hence, at the output of the medium, the once-weaker signal at lower frequency is amplified at the expenses of the higher frequency field as a consequence of the process of difference-frequency generation. For this reason, the DFG is also defined as optical parametric amplification (OPA) (more details in appendix B). The two-photon emission characterizing the DFG happens even when the input field at frequency ω_2 is not present and, in this case, it is called spontaneous two-photon emission because the DFG process is seeded by the vacuum fluctuations. Finally, in the optical rectification the generation of the DC electric field (zero-frequency component) can be seen as a DFG process, with one of the two created photons at the same frequency of the annihilated photon and the other at zero-frequency.

So far, the entire discussion was based solely on perfectly monochromatic fields, which are obtained from continuous wave lasers. However, the only lasers presenting field peak intensities sufficiently high to induce nonlinear processes are pulsed lasers with a finite duration, and thus a non-zero frequency bandwidth (see subsection 2.1.1). This in turn implies that the new frequencies generated by the nonlinearities of the medium present non-null frequency span, and it is of fundamental importance for certain applications. For instance, the optical rectification of non-monochromatic sources, e.g. femtosecond laser

pulses, gives a field with frequency components centered around DC. If the spectrum of the mentioned input source ranges from the visible to the near-infrared (NIR), then the generated quasi-DC components fall in the terahertz (THz) range. This is one of the main methods to design THz sources, as it will be reported in subsection 2.5.1.

2.4.2 Third-Order Nonlinearities

Looking back at the simplistic interpretation of second-order nonlinearities in terms of photon exchange with a two-level system in fig. 2.5, it's immediate to realize that $\chi^{(2)}$ processes are three-wave mixing processes. Similarly, third-order nonlinear phenomena are four-wave mixing processes, meaning that the total number of annihilated and generated photons is four.

In the most general case, the third term of eq. 2.28, $P^{(3)}(t) = \epsilon_0 \chi^{(3)} E^3(t)$, is induced by a field composed of three different frequency components:

$$E(t) = \frac{1}{2}E_1 e^{-i\omega_1 t} + \frac{1}{2}E_2 e^{-i\omega_2 t} + \frac{1}{2}E_3 e^{-i\omega_3 t} + c.c. \tag{2.33}$$

Following straightforward calculations, we find that the term $E^3(t)$ contains up to 22 different positive frequency components (and other 22 if also the negative frequencies are considered), which are [35]

$$\begin{aligned}
&\omega_1, \omega_2, \omega_3, 3\omega_1, 3\omega_2, 3\omega_3, (2\omega_1 \pm \omega_2), (2\omega_1 \pm \omega_3), (2\omega_2 \pm \omega_1), (2\omega_3 \pm \omega_2), \\
&(\omega_1 + \omega_2 \pm \omega_3), (\omega_1 + \omega_3 - \omega_2), (\omega_3 + \omega_2 - \omega_1)
\end{aligned} \tag{2.34}$$

For the moment, we focus our attention to the components at frequencies ω_i and $3\omega_i$, which also constitute the sole components obtained in the particular case of a monochromatic incident field, i.e. when a single laser beam is the source:

$$E(t) = \frac{1}{2}E e^{-i\omega t} + c.c. \tag{2.35}$$

Then

$$\begin{aligned}
P^{(3)}(t) &= \frac{1}{8}\epsilon_0 \chi^{(3)} E^3 e^{-i3\omega t} + \frac{3}{8}\epsilon_0 \chi^{(3)} |E|^2 E e^{-i\omega t} + c.c. = \\
&= \frac{1}{4}\epsilon_0 \chi^{(3)} E^3 \cos(3\omega t) + \frac{3}{4}\epsilon_0 \chi^{(3)} |E|^2 E \cos(\omega t)
\end{aligned} \tag{2.36}$$

The first term represents the third-harmonic generation (THG) since it oscillates at 3 times the frequency of the exciting field: in the photon description represented in fig. 2.6, three photons at frequency ω are annihilated and one at frequency 3ω is generated. The second
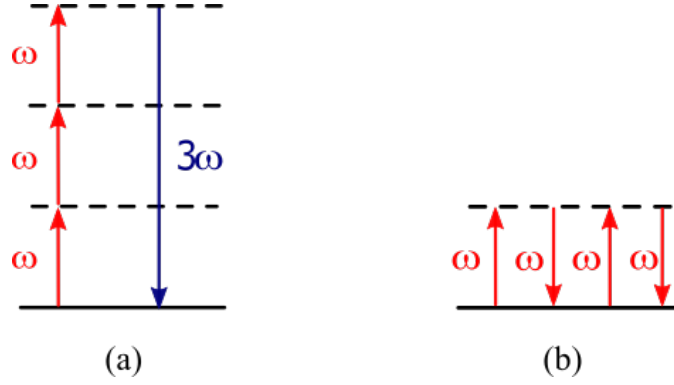
Figure 2.6 Energy-level diagrams for $\chi^{(3)}$ phenomena. (a) Third-harmonic generation. (b) Optical Kerr effect.

term constitutes a nonlinear contribution oscillating at the same frequency of the input field. Reminding that in the linear regime the index of refraction is directly related to the susceptibility and observing that the second term is proportional to the absolute value squared of the field, which in turn is related to the intensity of the field itself, it's practical to define the refractive index as

$$n(t) = n_0 + n_2 I(t) \tag{2.37}$$

with n_0 as the linear refractive index, $n_2 \equiv \frac{3\chi^{(3)}}{2n_0^2\epsilon_0 c}$ as an optical constant indicating the strength of the nonlinearity and $I(t) = \frac{1}{2}n_0\epsilon_0 c |E(t)|^2$ as the intensity of the field. This way, it is clear that the refractive index changes with the actual intensity of the incoming laser pulse. This effect is also known as optical Kerr effect, to distinguish it from the traditional Kerr effect where the refractive index of a certain medium varies by an amount proportional to the square of the applied static electric field. The optical Kerr effect is of particular relevance because it is at the basis of phenomena like self-focusing, which affects the spatial profile of the pulse, and self-phase modulation, concerning the temporal profile of the pulse.

Self-focusing occurs when a sufficiently intense pulse with a non-uniform transverse profile (e.g. a Gaussian-like shape) propagates through a material that presents positive n_2 coefficient. Such a medium acts as a positive lens since the refractive index is larger at the center of the beam with respect to its sides, inducing the rays to bend toward each other and focus within the material. From a practical point of view, it is important to consider this phenomenon to avoid possible damaging of the material due to the high intensities achieved as a consequence of the self-focusing. Another interesting consequence of self-focusing happens when the amount of focusing counteracts the natural divergence of a beam due to diffraction, giving rise to a field that can propagate for very long distances with an invariant spatial profile, also known as spatial soliton.

Self-phase modulation (SPM) causes a shift in the phase $\phi(t)$ of the optical pulse propagating through a medium and since it is related to a $\chi^{(3)}$ process, it happens in all materials, as detailed at the beginning of section 2.4. However, for this phenomenon to be relevant, the pulse has to be sufficiently short and intense. The change in phase after propagation through a material of thickness L is time-dependent because it is directly related to the intensity profile $I(t)$ of the field, oscillating at frequency ω_0, via the nonlinear coefficient n_2 (see eq. 2.37)

$$\phi(t) = \omega_0 t - \frac{\omega_0}{c} \left[n_0 + n_2 I(t) \right] L \tag{2.38}$$

This in turn causes a modification in the pulse spectrum, in particular it leads to a broadening of the spectrum if the medium presents $n_2 > 0$. Indeed, considering the instantaneous frequency $\omega(t)$, defined as the time derivative of the phase $\phi(t)$,

$$\omega(t) = \frac{d\phi(t)}{dt} = \omega_0 - \frac{\omega_0}{c} n_2 L \frac{dI(t)}{dt} \tag{2.39}$$

we realize that the leading edge of the pulse is redshifted (i.e. $\omega(t)$ is lower than ω_0), while the trailing edge is blueshifted (i.e. $\omega(t)$ is larger than ω_0).

Considering that a pulse going through any medium suffer dispersion (see subsection 2.1.1), SPM can lead to a pulse temporal broadening or shortening if the material shows normal or anomalous dispersion, respectively. Consequently, SPM can be exploited in particular conditions to obtain ultrashort pulses. Another phenomenon deriving from the temporal shortening due to SPM is temporal solitons: the broadening due to dispersion is exactly matched by the shortening due to the nonlinearities, producing a pulse that keeps propagating in the medium with invariant temporal profile.

2.4.3 Phase Matching Condition and Birefringence

All the processes described above are parametric processes, which means that the initial and final quantum-mechanical states of the considered system are identical. This implies that the population excited from the ground state can reside in the virtual states only for a very brief amount of time $\Delta\tau$ (for this reason they are defined as virtual), generally in the order of few femtoseconds. In accordance with the Heisenberg uncertainty principle, $\Delta\tau$ is described by the relation

$$\Delta\tau \Delta E \sim \hbar \tag{2.40}$$

where $\Delta E = \hbar \Delta\omega$ is the energy difference between the virtual state and the nearest *eigenlevel*, or from a similar perspective, it represents the energy broadening $\hbar \Delta\omega$ of the *eigenlevel* (see

fig. 2.7(a)).

Another direct consequence of being a parametric process is that both energy and momentum of the photons are conserved since neither energy nor momentum can be transferred to or from the medium. The energy conservation imposes a precise relationship between the annihilated and the created photons. For example, in the DFG process the generated photons, at frequency ω_2 and ω_3, and the destroyed one, at frequency ω_1, are such that

$$\hbar\omega_3 = \hbar\omega_1 - \hbar\omega_2 \tag{2.41}$$

Similarly, in the SFG the new photons are given by the sum of the incoming photons. SHG and OR coincide, respectively, to the sum-frequency and difference-frequency generation processes involving photons within the same frequency component of the field, or seen from an experimental perspective, involving photons that belong to the same laser beam.

Moving to the momentum conservation, it can be expressed in the same way as in eq. 2.41 (still in the case of DFG):

$$\hbar\mathbf{k}_3 = \hbar\mathbf{k}_1 - \hbar\mathbf{k}_2 \tag{2.42}$$

When this relation is satisfied, the nonlinear process occurs with its maximum efficiency and the phase matching condition is met.

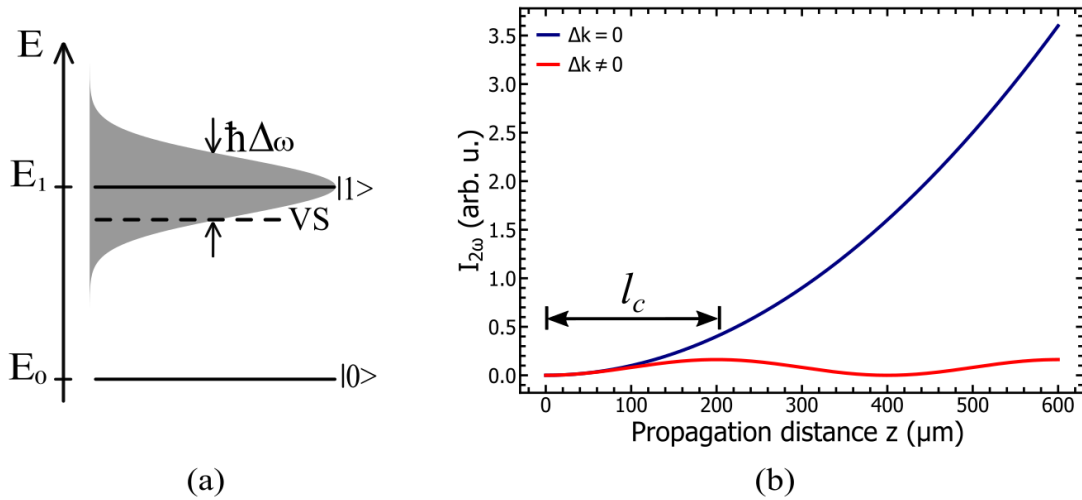Figure 2.7 (a) Physical interpretation of the virtual state (VS), which can be thought as a consequence of the energy broadening $\hbar\Delta\omega$ of the excited state $|1\rangle$. (b) Dependence of the SH intensity on the propagation distance z for the case where phase matching is satisfied (blue trace) and where it is not achieved (red trace). For the latter case, the coherence length is equal to 200 μm.

To describe the phase matching condition from a physical point of view we can depict the material as an ensemble of a very large number N of atoms and we will consider for simplicity the case of second-harmonic generation. When the input field at frequency ω hits the material, the atom develops an oscillating dipole moment containing multiple frequency components, as seen in the previous subsections, among which there is one at the double-frequency 2ω. The oscillatory motion of the atom generates in turn a radiation at the same frequency [35]. This process happens for every atom of the material and in the most general case these dipoles oscillate out of phase with respect to each other (phase mismatch). The emitted radiation fields will then destructively interfere and the total emitted radiation would be zero. However, when the relative phasing of the dipoles is correct, the radiated fields add constructively in the forward direction leading to a well-defined beam at the SH frequency. Since the phase of the dipole oscillation depends on the phase of the incident fields, to achieve in-phase oscillation, the input field should propagate through the material with the same speed as the emitted radiation at 2ω. For this reason, to obtain phase matching, the conservation of the momenta, which is related to the propagation speed of the fields, has to be satisfied. Indeed, recalling that $k = \omega n(\omega)/c$, in a collinear configuration eq. 2.42 can be rewritten for the case of SHG as

$$\Delta k = n(2\omega)2\omega - 2n(\omega)\omega = 0 \tag{2.43}$$

So far we have given a qualitative explanation of why the phase matching condition leads to the maximum efficiency of the considered nonlinear process. However, even if Δk is not exactly 0, the nonlinear process can still manifest itself provided the thickness of the medium is properly chosen. Solving the propagation equation in a nonlinear medium in the monochromatic limit [34], it can be shown that, under the assumption of nondepleted fundamental beam (i.e. the intensity I_ω of the fundamental beam is constant), the intensity of the SH beam $I_{2\omega}$ is related to the propagation distance z through medium via the equation

$$I_{2\omega}(z) \propto I_\omega^2 \left[\frac{2}{\Delta k} \sin\left(\frac{\Delta k z}{2} \right) \right]^2 \tag{2.44}$$

We notice that for very small values of Δk, eq. 2.44 reduces to

$$I_{2\omega}(z) \propto I_\omega^2 z^2 \tag{2.45}$$

Fig. 2.7(b) shows the dependence of $I_{2\omega}$ on the propagation distance z for the phase-mismatched and phase-matched cases, respectively described in eqs. 2.44 and 2.45. While

for small z the curve increases quadratically in both cases, for the phase-mismatched one the intensity reaches a maximum at the distance $l_c \equiv \pi/\Delta k$, known as coherence length, which corresponds to the distance over which the accumulated phase shift between the input field and the induced polarizations is equal to $\pi/2$. After this point, the nonlinear contributions add up in a negative way, causing $I_{2\omega}$ to decrease gradually to 0, following a sinusoidal behavior with period equal to $2l_c$. This means that when phase matching cannot be satisfied, to generate the highest intensity of the SH beam the crystal thickness should be chosen equal to the coherence length. Generally, l_c is in the order of tens of micrometers, leading to very weak nonlinear beams. Therefore, it is evident the need to satisfy phase matching.

Achieving phase matching in a dispersive medium for a given set of frequencies can be absolutely non-trivial due to the frequency-dependent refractive index (see subsection 2.1.1). For this reason, it can be shown that it is generally not possible to satisfy this condition in an isotropic medium. On the other hand, it is very common to exploit the birefringence of certain non-centrosymmetric crystals, like β-barium borate (BBO), lithium niobate (LiNbO$_3$), silicon carbide (SiC), etc.

Birefringence is the property for which the refractive index of the material is polarization dependent. In particular, we limit ourselves to the simpler case of uniaxial materials, in which there is only a single direction that dictates the optical anisotropy, defined as optical

(a)   (b)
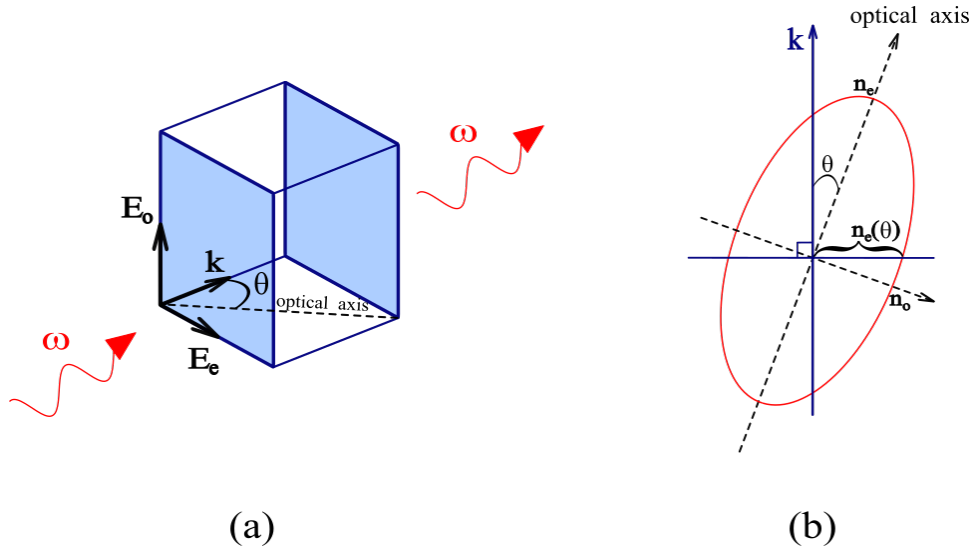
Figure 2.8 Uniaxial birefringent crystals. (a) Section of a crystal cut at an angle θ with respect to the optical axis and indication of ordinary E_o and extraordinary E_e polarization components of the field $\mathbf{E}$. (b) Section of the index ellipsoid for a positive ($n_e > n_o$) uniaxial crystal with explicit graphical representation of ordinary and extraordinary refractive indices. In both pictures $\mathbf{k}$ represents the wave vector.

axis, while all its perpendicular directions are optically equivalent. Hence, uniaxial crystals present two frequency-dependent refractive indices: the ordinary refractive index, n_o, seen by the ordinary polarization component, and the extraordinary refractive index, n_e, seen by the extraordinary polarization component, parallel to the optical axis (refer to fig. 2.8). If the field propagates parallel to the optical axis, the refractive index is always n_o, regardless of the polarization. However, when the field wave vector $\mathbf{k}$ presents an angle θ with respect to the optical axis, the ordinary polarization experiences n_o while the extraordinary polarization propagates with a refractive index that varies between n_e and n_o, as a function of θ according to the following equation:

$$(n_e(\theta))^{-1} = \sqrt{\frac{\cos^2(\theta)}{n_o^2} + \frac{\sin^2(\theta)}{n_e^2}} \qquad (2.46)$$

As a consequence, it is often possible to optimize the phase matching for a given frequency or bandwidth by properly tuning the angle θ to obtain the value of $n_e(\theta)$ that satisfies eq. 2.43. Depending on the polarization of the fields involved in the nonlinear interaction, it is possible to differentiate between:

- *Type-I* phase matching: the fundamental beams present the same polarization, perpendicular to the one of the beam obtained from the nonlinear process

- *Type-II* phase matching: the fundamental beams are on crossed polarizations

2.5 Literature Review on Generation and Detection of Terahertz Fields

Even though the terahertz radiation occurs naturally in our everyday life, this region of the electromagnetic spectrum has been historically one of the least explored parts, mostly due to the lack of compact THz sources and detection systems. For this reason, in the past 30 years a lot of effort has been put into the development of strategies to efficiently generate and coherently detect such radiation [1–3], making nowadays available a large variety of methods. The goal of this section is to briefly discuss the state-of-the-art of some of the most common methods, reserving particular attention for the generation via optical rectification (OR) and detection via four-wave mixing (FWM) in solid-state media, being, respectively, the techniques adopted in this work to generate and detect few-cycles THz pulses. In addition, we will discuss some of the pros and cons of the various methods in order to justify the choice of the aforementioned techniques. The first part is dedicated to the generation methods, while the second focuses on the detection ones.

2.5.1 Terahertz Generation

The technique based on the use of photoconductive (PC) switches is one of the most common approaches for generation of THz pulses. It was first introduced in the early 1980s by Auston and Smith [15]. The working principle consists in the generation of sub-picosecond electromagnetic pulses caused by the acceleration of free carriers in a semiconductor. The free carriers are created when an ultrashort laser pulse hits the material and then they are immediately accelerated by the presence of electrodes kept under strong electric bias [2,3,15]. In other words, the generation of THz transients happens when this biased semiconductor device is short-circuited by the laser pulse.

Since the energy of the THz pulses directly depends on the applied bias field, the generation of THz is a very efficient process, especially for small energy values of the pump pulse. Indeed, it was demonstrated [16] that in the range of small pump energies (less than few μJ) this approach is more advantageous with respect to optical rectification, while for higher pump energies the opposite happens because strong saturation is reached sooner than in the case of OR.

PC switches typically produce broadband (of about 5 THz) gap-free generation below 7 THz [3], while they can reach frequency components up to 15 THz, with the presence of a spectral gap around 8 THz [39] due to absorption in the material. Indeed, the most common material used for these devices is gallium arsenide (GaAs), which presents transverse optical (TO) phonon resonances exactly at 8 THz. The choice of such a material is mostly related to its fast carrier rise time and high mobility, characteristics that make it a perfect candidate for high-efficient generation. In addition, it has a bandgap of 1.42 eV, which is slightly below the photon energy of a 800nm-Ti:Sapphire laser (1.55 eV), source widely used for THz generation and detection. In comparison with OR, the generation of high frequency components is less favorable since it is ultimately limited by the non-instantaneous response time of the free carriers, and the optical alignment can be significantly more complicated than in the case of OR.

Another interesting technique to produce ultrashort THz pulses implies the use of high-intensity femtosecond laser pulses to create plasma, which in turn emits coherent THz radiation. Two-colors driven laser-induced air plasma presents the advantage of not having a damage threshold for the emitter, since in principle the gas medium can be replenish continuously [3]. This means that optical pulses with very high intensity can be employed and THz radiation stronger than the one obtained with PC switches or OR is achieved [20]. This mechanism can be partially explained with a perturbative model as a four-wave mixing process between the fundamental beam and the second-harmonic, both focused in the air, as

proposed by Cook *et al.* [21]. Basically, it is the equivalent of the more traditional optical rectification, but based on a $\chi^{(3)}$ effect instead of a $\chi^{(2)}$ effect, and for this reason it is sometimes referred to as four-wave rectification [2, 3, 20]. It can be shown that the THz electric field $E_\Omega(t)$ is proportional to

$$E_\Omega(t) \propto \chi^{(3)} E_{2\omega}(t) E_\omega^*(t) E_\omega^*(t) cos(\Delta\phi) \tag{2.47}$$

where $E_\omega(t)$ and $E_{2\omega}(t)$ represent the field amplitudes of the fundamental and second-harmonic, respectively, and $\Delta\phi$ is the phase difference between the two fields. This implies that the relative phase $\Delta\phi$ is critical for efficient THz generation, and it can be precisely controlled by exploiting proper phase shifting media. With such adjustments, peak THz electric field of more than 60 kV/cm are rather easily obtained using as excitation source pulses with energy of about 0.5 mJ [3, 20], while recent developments yielded peaks of 100 MV/cm [40]. Actually, this perturbative model is not able to fully explain these levels of field strength as it is necessary to introduce a semiclassical transient photocurrent model, in which the THz transient is produced as a consequence of a nonvanishing transverse plasma current, consisting of bounded electrons that were stripped off (photoionized) by the two-color laser field [41].

Another positive aspect of this method is that there is no material absorption or dispersion, since it happens in air, achieving pretty regularly flat THz spectra extending up to 30 THz without a spectral gap [42]. This does not happen neither in PC switches, as mentioned above, neither in OR due to the phonon resonance of the nonlinear crystals where the THz generation takes place. The bandwidth of the THz pulse is limited only by the duration of the probe pulse and ultrabroadband generation up to 200 THz, inducing the plasma with 10 fs pulses, was demonstrated by Matsubara *et al.* [43]. With this said, the very high optical pulse energies (at least, if not higher than, 0.5 mJ) needed to produce the plasma impose some serious constraints on the laser source, limiting the widespread of such technique. Furthermore, instabilities caused by air fluctuations are difficult to be kept under control, making it non-trivial to achieve precise metrology measurements.

The fact that extreme THz field strengths do not play a fundamental role for the successful demonstration of the proof-of-principle THz field-resolved detection technique, which is the main focus of this work, added to the unavailability of a laser source capable of emitting pulses with energy values discussed above, convinced us to choose optical rectification of femtosecond pulses in nonlinear crystals as the source of THz radiation.

This second order nonlinear process produces THz as a result of difference-frequency generation (DFG) between the spectral components within a single ultrashort pump pulse (see

subsection 2.6.1 for a thorough analysis of OR). The larger the spectral bandwidth of the pump pulse, or in other words the shorter the pump pulse, the higher the generated THz frequencies. Most common materials chosen for this method are zinc telluride (ZnTe), gallium phosphide (GaP), gallium selenide (GaSe) and lithium niobate (LiNbO$_3$) [2,3,20]. A shortcoming of this technique, that is shared by all the crystals just listed, is the presence of a spectral gap, also known as Reststrahlen band [3], at low THz frequencies: it is due to the TO phonon resonances of those non-centrosymmetric media and it causes distortion in the pulse spectra as a consequence of absorption, dispersion and improper phase matching [2,44]. Depending on the particular material, the lowest TO phonon resonance ranges from around 5 THz, in ZnTe, up to 11 THz, in GaP.

ZnTe is the most used crystal for OR since it presents a rather high nonlinear coefficient compared to the other crystals and the phase matching condition is easily achieved in a collinear geometry for low THz frequencies, in the range 0.1-3.0 THz, when the pump laser is a Ti:Sapphire running at 800 nm [24]. A possible drawback of this material is that the amount of pump intensity used in the THz conversion is limited by a strong two-photon absorption at 800 nm, which in turn increases the THz absorption as a result of the larger number of free carriers [3,45]. OR in ZnTe was shown to be working also at telecommunication wavelengths, i.e. around 1550 nm, allowing to develop low-cost and compact THz systems exploiting the advantages of fiber laser technology [46]. However, a worse performance than in the case of a 800 nm excitation source is expected due to the larger phase mismatch of the nonlinear process at 1550 nm. GaP suffers similar drawbacks as for ZnTe, especially in terms of the two-photon absorption, and it has a lower nonlinear coefficient than ZnTe [3,24]. Nevertheless, low THz frequencies are well phase matched, in a collinear geometry, with optical pulses with central wavelength at 1 μm, making this crystal a good candidate for OR driven by ytterbium-doped fiber lasers [47]. GaSe is characterized by a significantly lower nonlinear coefficient but it has the great advantage of being a birefringent crystal, which allows to satisfy velocity matching for higher THz frequencies than in the case of ZnTe and GaP by simply playing with the incidence angle. This means that broader spectra, from 10 to 100 THz, can be routinely obtained [17], provided that the pump pulse duration is of few fs, and pulses covering the entire range from mid-IR to THz can be generated [18,19]. Finally, LiNbO$_3$ is another well-suited candidate for OR given its really high effective nonlinearity and its large bandgap, which removes the issue of two-photon absorption when the pumping is at 800 nm, allowing the use of larger pump intensities [2,3]. THz pulses with energies that are orders of magnitude superior to that of ZnTe can be produced, but they present narrower bandwidth than the ones generated with GaSe. In addition, phase matching cannot be achieved in a collinear geometry: the only ways to make OR work is either to exploit quasi-phase matching

in periodically poled lithium niobate [48], either to adopt tilted-pulse-front pumping, making it an effective noncollinear geometry since the THz radiation arises perpendicularly to the pump tilted front [49].

2.5.2 Terahertz Detection

PC switches are employed not only for generation but also for detection of THz fields, in the form of PC antennas. Broadband detection was demonstrated up to 60 THz by Kono *et al.* [22] with a GaAs PC antenna gated by 15 fs Ti:Sapphire pulses, achieving detection of ultrashort THz transients generated via OR. Furthermore, recent developments in the domain of plasmonic nanoantennas yielded THz detection PC-antenna-based-systems that operate at telecommunication wavelengths ($\sim$1550 nm), feature that was previously unavailable due to the high dark current levels induced in the substrate by the high bias electric fields [23]. As for the generation based on PC switches, even though the high-frequency tail of the response can be detected with such strategy, these detectors still present an exponential weighting toward lower frequencies with respect to other techniques, such as electro-optic sampling (EOS) and detection in plasmas.

Electro-optic sampling, based on a THz-induced Pockels effect (more details in subsection 2.6.2), has been proven to be a rather practical and easy-to-implement technique capable to detect ultrabroadband THz radiation [3, 17, 24], provided that a proper choice of the type and thickness of the nonlinear crystal is carried out. Indeed, as a general rule, the sensitivity increases with the thickness of the crystal, but the corresponding detected bandwidth diminishes. Similarly to what reported for OR, depending on the actual chosen material, the velocity matching between the optical probe and the THz components limits the efficiency and the bandwidth of the THz field: for instance, in the case of ZnTe and GaP typical detected spectra range between 0.1 and 5 THz [47, 50], while for thin slabs (around 20 μm) of GaSe the THz response can extend from 10 THz all the way to 105 THz, with a maximum around 34 THz, when the incidence angle is properly adjusted to achieve phase matching [17]. However, TO phonon absorption in EOS crystals always causes the presence of a spectral gap in the detected THz transient and makes the interpretation of the signal near the Reststrahlen band quite tricky, requiring proper corrections [44, 51]. Additionally, EOS is not particularly efficient for the detection of strong THz fields because of the drawback known as over-rotation [52, 53]: if the phase shift induced by the THz-driven birefringence is larger than $\pi/2$, then the polarization of the probe pulse can be over-rotated and the EOS trace is reversed, leading to ambiguities in the detected THz transient. In fact, this might happen even in the presence of moderate THz strengths. Since the birefringence is proportional to

both the THz field amplitude and the thickness of the crystal, the use of thicker crystals (in the order of few millimeters), with the goal to improve the signal-to-noise ratio (SNR), increases as well the chance of excessive rotation.

These limitations are not found in the THz wave detection with laser-induced plasma in gases, where the bandwidth of the entire time-domain spectroscopic system is limited only by the duration of the probe pulse. The phenomenon at the basis of such method is a four-wave mixing process, as in the four-wave rectification, in which two photons at the fundamental frequency combine with a photon at the THz frequency to produce an effective second-harmonic, also defined terahertz-field-induced second-harmonic (TFISH). Actually, the first demonstration of THz detection via TFISH was realized in a solid-state medium by Nahata and Heinz in 1998 [25], while in 2006 Dai *et al.* provided the first proof of TFISH-based coherent THz detection in laser-induced air plasma, from which the name air-biased coherent detection (ABCD) was introduced [26]. To achieve coherent detection of the THz transient, i.e. measurement of both intensity and phase of the field, the TFISH signal has to interfere with a strong local oscillator (LO) field (see subsection 2.6.3 for an in-depth explanation). In [26] such LO was obtained from a second-harmonic field produced in a supercontinuum of the detection plasma itself. However, this requires very intense probe pulses (more than 400μJ) and the LO cannot be independently controlled in terms of polarization, intensity and phase, which are all useful parameters to achieve efficient detection. A possible solution to ease the constraints on the pulse energy was reported by Karpowicz *et al.* [27], which consists in applying a high DC voltage across the plasma in order to break the symmetry and hence getting second-harmonic LO via external field-induced SHG. Another positive aspect of the latter method is that it is possible to control the polarization state of the LO. Nevertheless, it is required to handle strong voltages (up to few kilovolts), making applications like remote sensing more challenging [28]. In fact, the LO can be generated optically by introducing a $\chi^{(2)}$ crystal, such as beta-barium borate (BBO), along the probe beam path before the detection plasma, as suggested by Li *et al.* [28]. The latter strategy allows to act on the intensity, phase and polarization of the LO, without the strict requirements of extremely intense probe pulses nor high-voltage biases. In any case, whichever approach is used to obtain the LO, THz spectra gap-free have been detected in the range 0.3-10 THz with 80 fs optical pulses [27], and by reducing the probe pulse duration (down to 10 fs) the detection can be pushed up to 150 THz, as shown by Matsubara *et al.* [43]. Nevertheless, THz detection in air is not suitable for obtaining integrated THz sensors because of the highly energetic probe pulses required to generate the plasma.

Recent developments proved that it is possible to apply the same scheme as the one used in ABCD, where the LO field is obtained by applying a strong DC bias voltage, but using as

$\chi^{(3)}$ medium a solid-state material instead of air. This technique, named solid-state-biased coherent detection (SSBCD) by Tomasino *et al.* [54], permits to exploit the higher nonlinear coefficients and breakdown voltage of materials like silica [54] and silicon-nitride [55] with respect to air, which means that significantly lower bias voltages (tens of volts) and lower probe pulse energies (few tens of nJ) are required [55], avoiding the need of high-cost intense ultrashort laser pulse sources. In addition, the proposed devices employ very thin layers (few μm) of $\chi^{(3)}$ media, resulting in basically irrelevant dispersion and absorption and broadband gap-free detection (0.1 to 10 THz) has been demonstrated, where the upper limit is only due to the optical probe duration (150 fs) employed in those particular experiments. Diamond is another promising material for THz detection via TFISH due to its excellent transparency and low refractive index dispersion in the entire infrared range, together with a third-order nonlinear susceptibility larger by three orders of magnitude with respect to that of air. In a recent work by Matsubara *et al.* [56], using 10 fs pulses they were able to detect a THz radiation with flat spectrum in the range 1-100 THz, with a sensitivity enhanced by two orders of magnitude compared with the ABCD in similar experimental conditions.

As it was introduced for TFISH detection in air, the LO can also be provided optically via SHG in a $\chi^{(2)}$ crystal and mixed with a TFISH produced in a solid-state crystal. This way, THz transients can be coherently detected using low-energetic probe pulses, in the order of 100 nJ, and without the need of using electrodes to get a strong DC bias. For instance, Chen *et al.* [53] reported the study of TFISH detection in a beta-barium borate (BBO) sample, which behaves as the source of both the TFISH signal and the LO, being a non-centrosymmetric medium. In parallel, they clearly showed how this method allows to measure intense terahertz fields (up to 160 kV/cm) that would cause a distorted trace if detected via EOS due to the over-rotation issue [53]. Finally, an advantage that is shared by all these methods that exploit solid-state materials as nonlinear media for TFISH detection is that they expand the selection of suitable materials, since both centrosymmetric and non-centrosymmetric are allowed, making it easier to obtain miniaturized integrated photonics devices for mid-IR and THz pulse detection.

For all the reasons just mentioned, together with the fact that less intense optical pulses are needed, we try to demonstrate proof-of-principle coherent detection of THz transients exploiting TFISH generation in solid-state materials, mixed with a LO field produced in a separate arm, via SHG in a BBO crystal, so that it can be easily and independently manipulated in terms of intensity, phase, polarization. The latter aspect is particularly important in the outlook of extending this classical time-domain method to the quantum realm, such as for the metrology of quantum electric fields, where it is fundamental to get access to both quadratures of the field [30]. Indeed, with respect to the EOS technique, where

it is highly non-trivial to measure the quadrature of the field due to the intrinsic nature of the exploited process [31], with this $\chi^{(3)}$-based method employing an external and completely decoupled LO field, it is sufficient to act on the relative phase term of the homodyne signal and apply spectral filtering [29].

2.6 Generation and Field-Resolved Detection of Terahertz Fields

At this point, we can analyze in more details the approaches that will be exploited in this work to generate and detect THz transients, as quoted in the previous section.

2.6.1 Optical Rectification

The physical nature of optical rectification (OR) has already been introduced in subsection 2.4.1: this process, depicted in fig. 2.5(d), can be viewed as the annihilation of a photon ω from the non-monochromatic source and a creation of two photons, one at almost the same frequency ω and another one with quasi-DC frequency Ω, much smaller than the optical frequency and generally falling in the THz range. For this reason, this process is also known as intra-pulse difference-frequency generation.

In eq. 2.32, we determined that the bulk polarization induced by optical rectification in the case of a monochromatic source, $E(t) = E_0 e^{-i\omega t}$, is proportional to the applied light intensity

$$P_{OR}^{(2)} \propto \chi^{(2)} |E_0|^2 \tag{2.48}$$

with $\chi^{(2)}$ representing the second-order nonlinear susceptibility of the medium.

Now we consider an optical pulse, with duration τ and central optical frequency ω_0, as the source instead of a CW. The corresponding electric field can be expressed as $E_{\omega_0}(t) = E_0(t)e^{-i\omega t}$, where we emphasize that the field amplitude is now time-dependent. Under the assumptions that the pulse envelope varies slowly with respect to the optical period, i.e. $\tau \gg 1/\omega_0$, and that the dependence of $\chi^{(2)}$ on the frequency is negligible near the optical frequency ω_0 [2], it can be demonstrated that the rectified nonlinear polarization $P_{OR}^{(2)}$ replicates the pulse envelope. For instance, considering a pulse with Gaussian-like envelope of duration τ, $E_{\omega_0}(t) = E_0 e^{-t^2/\tau^2} e^{-i\omega_0 t}$, the induced polarization becomes

$$P_{OR}^{(2)}(t) \propto |E_{\omega_0}(t)|^2 = P_0 e^{-2t^2/\tau^2} \tag{2.49}$$

Then, reminding that the generated THz field $E_\Omega(z,t)$ is related to the induced polarization

P_{OR} via the wave equation [2]

$$\frac{\partial^2 E_\Omega(z,t)}{\partial z^2} - \frac{n^2}{c^2}\frac{\partial^2 E_\Omega(z,t)}{\partial t^2} = \frac{1}{\epsilon_0 c^2}\frac{\partial^2 P_{OR}^{(2)}(z,t)}{\partial t^2} \qquad (2.50)$$

where we assumed that a linearly polarized optical plane wave is propagating along the z-axis, and n represents the refractive index seen by the THz field.

Moving to the frequency domain and expressing $E_\Omega(z,t)$, $P_{OR}(z,t)$ in terms of spectral envelope functions ($\mathcal{E}_\Omega(z,\omega)$, $\mathcal{P}_{OR}(z,\omega)$) and Fourier integrals [34] as

$$E_\Omega(z,t) = \frac{1}{2}\left[\frac{1}{2\pi}\int_0^\infty d\omega \mathcal{E}_\Omega(z,\omega)e^{i[\omega t - k(\omega)z]}\right]$$
$$P_{OR}(z,t) = \frac{1}{2}\left[\frac{1}{2\pi}\int_0^\infty d\omega \mathcal{P}_{OR}(z,\omega)e^{i\omega t}\right] \qquad (2.51)$$

eq. 2.50 becomes

$$\left(\omega^2\frac{n^2}{c^2} - k^2(\omega)\right)\mathcal{E}_\Omega - 2ik(\omega)\frac{\partial\mathcal{E}_\Omega}{\partial z} + \frac{\partial^2\mathcal{E}_\Omega}{\partial z^2} = -\frac{\omega^2}{\epsilon_0 c^2}\mathcal{P}_{OR}e^{ik(\omega)z} \qquad (2.52)$$

Introducing the so called slowly varying envelope approximation ($SVEA$), which is valid when the variation of $\mathcal{E}_\Omega$ due to the effect of nonlinear propagation is small over a distance on the order of the optical wavelenght, we can assume that

$$\left|\frac{\partial^2\mathcal{E}_\Omega}{\partial z^2}\right| \ll 2k\left|\frac{\partial\mathcal{E}_\Omega}{\partial z}\right| \ll k^2\left|\mathcal{E}_\Omega\right| \qquad (2.53)$$

In addition, noting the dispersion relation $k(\omega) = \omega n/c$, eq. 2.52 simplifies to

$$\frac{\partial\mathcal{E}_\Omega(z,\omega)}{\partial z} = -\frac{i\omega}{2n(\omega)\epsilon_0 c}\mathcal{P}_{OR}e^{ik(\omega)z} \qquad (2.54)$$

in which the nonlinear polarization P_{OR} behaves as a source term which excites the complex spectral amplitude of the electric field $\mathcal{E}_\Omega$. By expliciting the dependence of P_{OR} on the input electric field E_{ω_0}, it can be shown [34] that the source term contains the exponential term $e^{-i\Delta k(\Omega)z}$, with $\Delta k(\Omega)$ representing the phase mismatch for the OR process

$$\frac{\partial\mathcal{E}_\Omega(z,\omega)}{\partial z} \propto e^{-i\Delta k(\Omega)z} \qquad (2.55)$$

In a dispersive nonlinear medium, the phase matching is achieved when the group velocity of the optical pulse is equal to the phase velocity of the central frequency Ω of the THz

spectrum [2, 3]

$$\frac{c}{n_{\omega_0} + \omega_0 \left.\frac{dn(\omega)}{d\omega}\right|_{\omega_0}} = \frac{c}{n_\Omega} \qquad (2.56)$$

Indeed, the phase matching condition for OR requires $\Delta k(\Omega) = k(\Omega) + k(\omega_0) - k(\omega_0 + \Omega) = 0$. Since the THz central frequency is much smaller than the frequency of the probe, i.e. $\Omega \ll \omega_0$, we can approximate the difference $k(\omega + \Omega) - k(\omega) \approx \partial k/\partial\omega|_{\omega_0} \cdot \Omega$, and we recognize the term on the right as the group velocity (see subsection 2.1.1). Hence, the phase matching condition can be rewritten as

$$\Delta k(\Omega) = \frac{\Omega}{c} \left[n(\Omega) - n_g(\omega_0) \right] = 0 \qquad (2.57)$$

leading to a condition equivalent to the one expressed in eq. 2.56.

To get a qualitative analysis of the influence of phase matching on the efficiency of the nonlinear process, we can consider that the incident pulse interacts with an infinitesimally thin layer of the nonlinear material, and then retrieve the total response of the material by adding up the single contributions of all the layers that constitute the medium. In this view, considering for simplicity a Gaussian pulse, from eqs. 2.49 and 2.50 we get that the resulting THz field is proportional to the second-order derivative of a Gaussian function, as shown in fig. 2.9(a).

If phase matching is satisfied, the THz pulse propagates with a phase velocity which is equal to the group velocity of the incident pulse, i.e. $v_\Omega = v_{\omega_0}$, as detailed above, and each infinitesimal contribution constructively interfere. On the other hand, in presence of a phase mismatch, the single contributions start to add up in a destructive fashion, and the worst case is reached when the considered length l_c of the medium is equal to the coherence length, as discussed in subsection 2.4.3. Both situations are summarized, respectively, in panels (b) and (c) of fig. 2.9.

Achieving a good OR phase matching over a large bandwidth is important not only because it allows to increase the thickness of the nonlinear crystal, which translates directly to a stronger THz field, but also because it leads to generation of broadband THz spectra. However, a decent phase matching is not enough to get wide spectra because the duration of the pump pulse comes into play as well, in particular the shorter the excitation pulse the wider the spectrum of the induced THz field will be. Indeed, this can be proved following a thorough mathematical analysis [57, 58] of the optical rectification process, but it can also intuitively understood by looking at eq. 2.49: a short pump pulse induces a fast nonlinear polarization, that in turn gives rise to a short THz pulse, which means a wide spectrum in the Fourier domain. For instance, it can be shown that employing pump pulses with duration of about
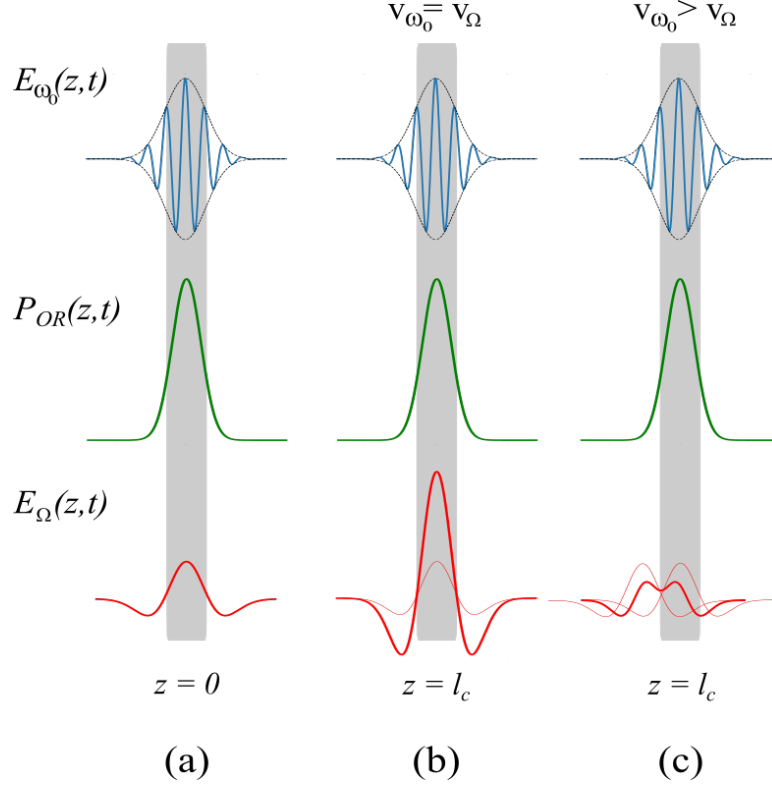
Figure 2.9 THz field generated via Optical Rectification. (a) THz field generated via OR by a thin layer: its linear proportionality to the second-order time derivative of P_{OR} is evident. (b) Constructive interference between the THz field generated by two layers when phase matching is satisfied. (c) Phase mismatch between the THz field and the optical pulse leads to destructive interference between the generated fields when the layers are separated by a distance equal to the coherence length l_c.

50 fs, even considering perfect phase matching, the generated THz spectrum is limited below 10 THz, approximately.

2.6.2 Electro-Optic Sampling

One of the most affirmed techniques which is able to achieve field-resolved detection of THz pulses is a pump-probe technique known as Electro-Optic Sampling (EOS). This method is exploited in this work to get a first characterization of the THz radiation generated via optical rectification and to compare the detected THz trace with the one measured with the technique of interest, i.e. the one based on the TFISH generation. EOS is chosen for its ease of implementation and for the fact that it works well even for low-energetic pulses, aspect that is not true for other techniques like air-biased coherent detection (refer to subsection 2.5.2).

EOS consists in the measurement of the THz field-induced birefringence, via the Pockels effect in a nonlinear crystal, with the help of a weak optical probe, and the entire THz waveform is determined by measuring such birefringence as a function of the relative delay between the THz and the probe pulses [1, 2].

The Pockels effect, also known as linear electro-optic effect, is a second order nonlinear effect caused by the presence of a static or low-frequency electric field. This phenomenon induces a modification in the refractive index of the nonlinear medium, that is proportional to the applied electric field strength [35]. From a qualitative point of view, this nonlinear process can be interpreted as a sum-frequency or difference-frequency operation between a photon at frequency ω and a quasi-DC photon (coming from the applied electric field) and resulting in the emission of a photon at the same optical frequency ω. Hence, there is a nonlinear contribution to the refractive index, which becomes a function of the applied external electric field. Following the discussion in section 2.4, since the Pockels effect is associated to the second-order nonlinear susceptibility, it can only occur in non-centrosymmetric materials.

The best way to introduce the linear electro-optic effect is via the deformations of the refractive index ellipsoid, expressed in the form

$$\left(\frac{1}{n^2}\right)_1 x^2 + \left(\frac{1}{n^2}\right)_2 y^2 + \left(\frac{1}{n^2}\right)_3 z^2 + 2\left(\frac{1}{n^2}\right)_4 yz + 2\left(\frac{1}{n^2}\right)_5 xz + 2\left(\frac{1}{n^2}\right)_6 xy = 1 \quad (2.58)$$

where (x, y, z) constitutes a general coordinate system and $\left(\frac{1}{n^2}\right)_i$ (with $i = 1, ..., 6$) represent the optical constants that are computed starting from the tensor elements which describe the index ellipsoid in the principal-axis coordinate system [35]. The latters are affected by the applied electric field E according to the following equation

$$\Delta\left(\frac{1}{n^2}\right)_i = \sum_{j=1}^{3} r_{ij} E_j \quad (2.59)$$

where r_{ij} are defined as electro-optic coefficients. These coefficients constitute a tensor, the electro-optic tensor of the medium, and generally most of them are zero due to symmetry reasons [35]. In practice, even along the directions for which the coefficients are non-zero, the applied field is able to cause only small refractive index changes, i.e. $r_{ij} E_j \ll 1$, hence we can approximate the expression in eq. 2.59 with

$$\Delta n_i \approx -\frac{n_0^3}{2} r_{ij} E_j \quad (2.60)$$

where we indicate with n_0 the linear refractive index. It results that the refractive index variation is linearly proportional to the field driving the nonlinear process.

In EOS, the terahertz field, at this point already generated, for instance, via optical rectification (see subsection 2.6.1), acts as the pump source for the Pockels effect, making the electro-optic crystal, which will be referred to as EOX for shortness, birefringent. Indeed, since the carrier frequency Ω of the THz field is much smaller than the central frequency ω of the visible or near-IR probe, the THz field can be considered as a quasi-DC field. As a consequence, the probe pulse propagating through the EOX suffers a modification in its polarization state, changing from linear to slightly elliptic.

Common crystals used in EOS, like zinc telluride (ZnTe) or gallium phosphide (GaP), present a zincblende structure. For such crystals, the optimal configuration for EOS requires having the THz field E_Ω and the probe field E_ω on orthogonal polarizations [59]: E_Ω is applied parallel to the [-110] axis, also indicated as x direction, while E_ω oscillates along the [001] crystalline direction, defined y direction. In addition, both fields propagate along the [110] crystallographic direction. This is summarized in fig. 2.10(a). As a result, a new index ellipsoid is generated with principal axes x' and y', rotated by 45° with respect to x and y.

(a)   (b)
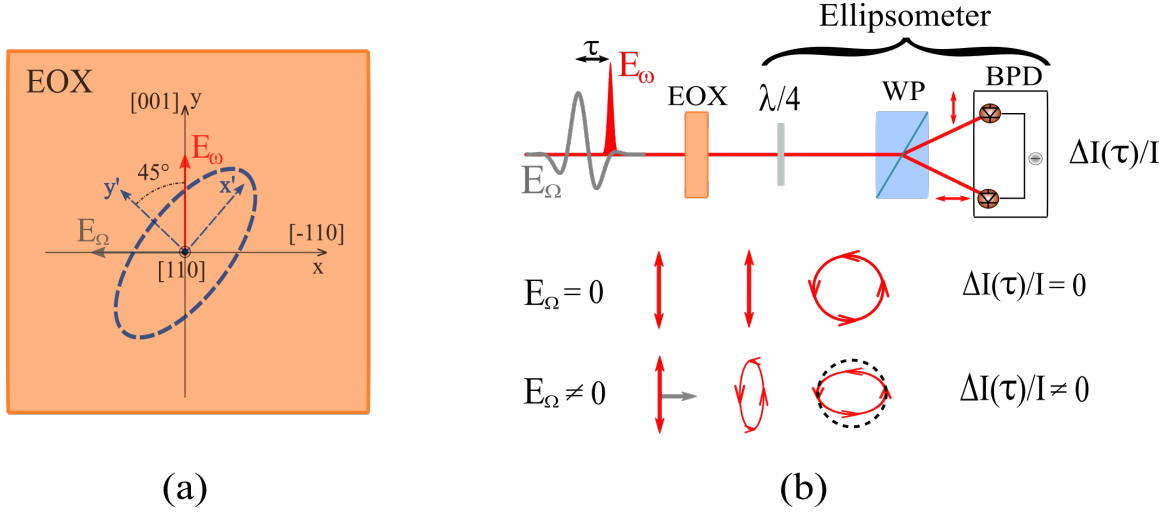
Figure 2.10 (a) Optimal geometry to get the largest phase shift due to the electro-optic effect when the electro-optic crystal (EOX) presents a zincblende-like structure. Both E_Ω and E_ω propagate along the [110] crystallographic direction. The dashed ellipse and arrows indicate the rotated coordinate system. (b) Working principle of the EOS detection scheme. The ellipsometer allows to retrieve the strenght of the THz field E_Ω, for a given relative delay τ with respect to the probe pulse E_ω, by measuring the power difference between the orthogonal polarization components induced by the nonlinear phase shift.

The refractive index n_0 is then modified along the x' and y' directions by the amount Δn

$$
\begin{aligned}
n_{x'} &= n_0 + \Delta n = n_0 + \frac{1}{2} n_0^3 r_{41} E_{\Omega,x} \\
n_{y'} &= n_0 - \Delta n = n_0 - \frac{1}{2} n_0^3 r_{41} E_{\Omega,x}
\end{aligned}
\tag{2.61}
$$

with r_{41} representing the tensor element relevant for the adopted geometry.

In turn, this means that for an EOX with thickness L the two orthogonal polarization components of the probe pulse present a global phase difference $\Delta\varphi$ equal to [2, 35, 60]

$$
\Delta\varphi = (n_{x'} - n_{y'}) \frac{\omega L}{c} = \frac{\omega L}{c} n_0^3 r_{41} E_{\Omega,x}
\tag{2.62}
$$

Hence, as discussed above, when the probe passes through the EOX, its polarization becomes elliptical. The probe polarization state is properly analyzed with the help of an ellipsometer, which includes an achromatic quarter-wave plate ($\lambda/4$), a Wollaston prism (WP) and a balanced photodiode detector (BPD) (see subsection 2.8.1 for more details on the BPD). The union of these three elements allows to measure the ellipticity of an optical field by looking at the difference between the power of each polarization component. The full operational principle of such a scheme is depicted in fig. 2.10(b).

The quarter-wave plate placed after the EOX turns the linear polarization of the probe into a circular one. Afterwards, the Wollaston prism separates the two orthogonal polarization components, which are then redirected to the two inputs of the balanced photodiode detector. In the bottom lines of fig. 2.10(b) there is a representation of the evolution of the polarization state of the probe pulse with and without the THz field, respectively. When $E_{\Omega,x} = 0$, the probe polarization is not modified and it stays linear; after the $\lambda/4$ the polarization is perfectly circular, meaning that the two orthogonal polarizations separated by the WP present the same power and the BPD outputs a null differential photocurrent $\Delta I/I$. On the other hand, when $E_{\Omega,x} \neq 0$, the birefringence of the EOX induces a phase shift $\Delta\varphi$ between the two probe polarization components and turns the linear polarization into an elliptical one. It follows that after the $\lambda/4$ the probe polarization is not purely circular as in the previous case, which leads to a power imbalance of the orthogonal polarization components and, thus, to a non-zero differential photocurrent $\Delta I/I$.

To obtain the dependence of $\Delta I/I$ on the THz field E_Ω, we consider the geometry discussed above and presented in panel (a) of fig. 2.10 [60]. In such case, the incoming probe field

$E'_{\omega,in}$, linearly polarized along y is expressed in the $(x' - y')$ basis as

$$E'_{\omega,in} = \frac{1}{\sqrt{2}} \begin{pmatrix} E_\omega \\ E_\omega \end{pmatrix} \tag{2.63}$$

As presented in eq. 2.61, the refractive index variations along the directions x' and y' are, respectively, $\Delta n_{x'} = -\Delta n_{y'} = \frac{1}{2} n_0^3 r_{41} E_{\Omega,x} \equiv \Delta n$, therefore, after the propagation through the EOX, the probe electric field is

$$E'_{\omega,EOX} = \frac{E_\omega}{\sqrt{2}} \begin{pmatrix} e^{i\frac{\Delta\varphi}{2}} \\ e^{-i\frac{\Delta\varphi}{2}} \end{pmatrix} \tag{2.64}$$

with $\Delta\varphi$ as defined in eq. 2.62. After the quarter-wave plate, with fast axis oriented in such a way to add a $\pi/2$ phase contribution to the x' direction, and projecting the field back on the (x, y) coordinate system via a 45° clockwise rotation, we obtain

$$E_{\omega,\lambda/4} = \frac{1}{\sqrt{2}} \begin{pmatrix} 1 & -1 \\ 1 & 1 \end{pmatrix} \frac{E_\omega}{\sqrt{2}} \begin{pmatrix} ie^{i\frac{\Delta\varphi}{2}} \\ e^{-i\frac{\Delta\varphi}{2}} \end{pmatrix} = \frac{E_\omega}{2} \begin{pmatrix} ie^{i\frac{\Delta\varphi}{2}} - e^{-i\frac{\Delta\varphi}{2}} \\ ie^{i\frac{\Delta\varphi}{2}} + e^{-i\frac{\Delta\varphi}{2}} \end{pmatrix} \tag{2.65}$$

At this point, since the Wollaston prism separates the two orthogonal polarization components, x and y, we can compute the resulting current signals I_x, I_y as

$$
\begin{aligned}
I_x &\propto \left| E_{\omega,\lambda/4,x} \right|^2 = \frac{E_\omega^2}{2} \left(1 + \sin(\Delta\varphi) \right) \\
I_y &\propto \left| E_{\omega,\lambda/4,y} \right|^2 = \frac{E_\omega^2}{2} \left(1 - \sin(\Delta\varphi) \right)
\end{aligned}
\tag{2.66}
$$

It follows that the normalized differential current signal is given by

$$\frac{\Delta I}{I} = \frac{I_x - I_y}{I_x + I_y} = \sin(\Delta\varphi) \approx \frac{\omega L}{c} n_0^3 r_{41} E_{\Omega,x} \propto E_{\Omega,x} \tag{2.67}$$

where the approximation $\sin(\Delta\varphi) \approx \Delta\varphi$ holds for small nonlinear phase shifts, i.e. $\Delta\varphi \ll 1$. Therefore, we notice that the obtained differential signal $\Delta I/I$ is linearly proportional to the THz field E_Ω and by varying the relative time delay between E_Ω and E_ω we are able to retrieve the entire sub-cycle time evolution of the terahertz electric field.

2.6.3 Terahertz-Field-Induced Second-Harmonic

In the previous subsection we presented a very efficient and established free-space technique to field-resolve a THz transient. Nevertheless, the nature of the electro-optic effect limits

the choice of materials to be used to the non-centrosymmetric class, being related to the second-order nonlinear susceptibility. On the other hand, there is another approach to coherently measure THz field pulses that is based on a four-wave mixing (FWM) process, hence a third-order nonlinear optical phenomena, observable in both centrosymmetric and non-centrosymmetric media [35] (see end of section 2.4 for a more detailed explanation). This implies that a broader class of materials is accessible to achieve such measurements. The aforementioned process is known as terahertz-field-induced second-harmonic (TFISH).

In the presence of an intense static electric field, the symmetry of a centrosymmetric medium is broken and an effective field-driven quadratic nonlinearity is induced. For this reason, under proper circumstances it is possible to generate second-harmonic radiation starting from an intense probe pulse, phenomenon that otherwise would be forbidden in the electric dipole approximation [35, 38] in a $\chi^{(3)}$ medium. In a similar fashion, reminding that a terahertz transient can be regarded as quasi-static with respect to the duration of the ultrafast probe, when a THz field propagates through the medium at the same time as the probe pulse, frequency doubling can be achieved.

To explain the FWM process we will exploit the same qualitative description of nonlinear frequency mixing introduced in section 2.4, which models the material as a two-level system and each excitation and relaxation of the medium involves a photon exchange. According to four-wave mixing theory [35], a photon from the THz field, at central frequency Ω, interacts with two photons from the probe at central optical frequency ω (see fig. 2.11(a)). As a result, there are two possible parametric processes that leads to the TFISH generation. In the first
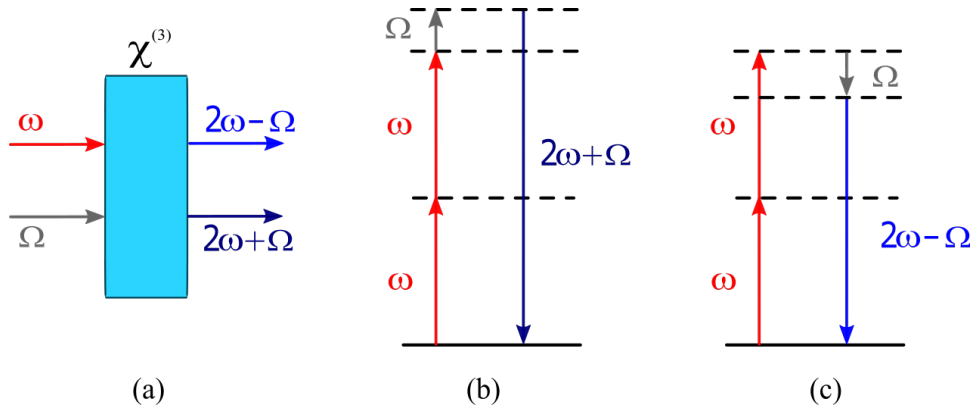

Figure 2.11 Four-wave mixing phenomena. (a) probe ω and THz Ω fields at the input of a $\chi^{(3)}$ induce an effective second-order nonlinearity and generate the TFISH $2\omega \pm \Omega$ via two parametric processes. (b) and (c) energy levels diagrams for four-wave mixing SFG and DFG phenomena, respectively.

one, depicted in panel (b) of fig. 2.11, the three photons add up to generate one at frequency

$$2\omega_+ = \omega + \omega + \Omega \tag{2.68}$$

where the "+" is used to highlight the resemblance with the sum-frequency generation (SFG) treated in subsection 2.4.1. In the second one, represented in fig. 2.11(c), two probe photons ω are annihilated to give rise to a THz photon Ω and another at frequency

$$2\omega_- = \omega + \omega - \Omega \tag{2.69}$$

In this last case, we used the "-" to recall the difference-frequency generation (DFG), where a pump (ω) and a signal beam (Ω) interact to generate signal and idler ($2\omega_-$).

Regardless of the actual parametric process, i.e. SFG or DFG, the electric field E_{TFISH} associated to the TFISH is somehow proportional to the probe field E_ω and the THz field E_Ω

$$E_{TFISH} \propto \chi^{(3)} E_\omega E_\omega E_\Omega \tag{2.70}$$

where $\chi^{(3)}$ represents the third-order nonlinear susceptibility. Since E_{TFISH} is linearly proportional to E_Ω, if we decide to detect the TFISH by measuring its intensity, I_{TFISH}, we get a signal that is proportional to the THz field intensity I_Ω. Hence, the phase information of the THz transient is lost and the detection is incoherent. On the other hand, by linearly mixing the TFISH with an optical local oscillator (LO) field E_{LO}, obtained for instance via second-harmonic generation of the fundamental probe beam, the resulting intensity measured with a photodetector is given by

$$I_{2\omega} \propto |E_{LO} + E_{TFISH}|^2 = |E_{LO}|^2 + \left|\chi^{(3)} E_\omega^2 E_\Omega\right|^2 + 2\mathrm{Re}\left\{\chi^{(3)} E_\omega^2 E_\Omega E_{LO}^*\right\} \tag{2.71}$$

where it is evident that the third term presents the desired linear proportionality with the applied THz field E_Ω. Now, to get a proper coherent detection, i.e. retrieve both intensity and phase information of E_Ω, we need to isolate the term of interest from the other contributions. The first term in the expression, $|E_{LO}|^2$, is the DC contribution from the LO and it can be easily filtered out with the help of a lock-in amplifier (see subsection 2.8.2 for an in-depth analysis) by modulating the THz beam. The second term, $\left|\chi^{(3)} E_\omega^2 E_\Omega\right|^2$, is proportional to the intensity of the TFISH, and in turn to the intensity of the THz field I_Ω. Now, depending on the strength of the LO, the detection system is either incoherent or coherent [26, 28]. Indeed, with a very low intensity LO, the second term dominates over the third one and thus $I_{2\omega} \propto I_\Omega$. Conversely, when the LO is relatively intense, i.e. $|E_{LO}| \gg |E_\Omega|$, the third term

becomes the dominant one and $I_{2\omega} \propto E_\Omega$, achieving coherent detection.

Under these conditions, considering to be able to change the relative delay τ between the THz and probe pulses, the resulting time-resolved cross-correlation signal $S_{2\omega}(\tau)$ reduces to

$$S_{2\omega}(\tau) \propto \text{Re}\left\{\int E_\omega^2(t)E_{LO}^*(t)E_\Omega(t-\tau)dt\right\} \tag{2.72}$$

Taking advantage of the fact that we can express each electric field as the product of their absolute values times a phase term, i.e. $E_\omega(t) = |E_\omega(t)|\,e^{i\phi_\omega}$ and $E_{LO}(t) = |E_{LO}(t)|\,e^{i\phi_{LO}}$, eq. 2.72 can be rewritten as

$$S_{2\omega}(\tau) \propto \text{Re}\left\{\int \left|E_\omega^2(t)\right| |E_{LO}^*(t)|\,e^{i(2\phi_\omega - \phi_{LO})}E_\Omega(t-\tau)dt\right\}$$
$$\propto \cos(\Delta\phi)\int I_\omega^2(t)E_\Omega(t-\tau)dt \tag{2.73}$$

where we introduced $\Delta\phi \equiv 2\phi_\omega - \phi_{LO}$ and we exploited the relation $|E_{LO}^*(t)| \propto |E_\omega^2(t)| \propto I_\omega(t)$. This implies that this technique is sensitive to the phases of the optical beams and with proper adjustments in the detection systems it is possible to adjust $\Delta\phi$ such that it gives the highest sensitivity, i.e. $\Delta\phi = m\pi$, with m integer value.

2.7 Diffraction and Collection of a Terahertz Beam

In the previous parts we discussed efficient strategies to generate and coherently detect THz transients with strong signal-to-noise ratios and broad spectra. However, all of this is possible if the generated terahertz beam is properly collected and focused in the detection crystal to drive either EOS or TFISH generation, allowing the detection. This task is far from trivial and it requires particular precautions, as it will be detailed in section 3.2.

In particular, a major cause of losses of the THz beam is due to the very strong divergence of low THz frequencies [58], i.e. smaller than 10 THz, and here below we provide an approximate model to estimate the collection efficiency of the THz beam using an off-axis parabolic mirror (OAPM) with diameter D and effective focal length f. Considering a Gaussian pump beam with w_p as $1/e^2$ beam waist, when focused it generates a THz beam, Gaussian as well, with central frequency Ω and radius $w_{\Omega,0}$ equal to $w_p/\sqrt{2}$ [35, 38]. To get a first estimate of the collected fraction of power, we assume that the wavelength is much smaller than the THz beam waist, $w_{\Omega,0}$, i.e. when $kw_{\Omega,0} \gg 1$, with k the corresponding wave vector. Under this assumption, known as paraxial approximation, this beam propagates following the laws of Gaussian optics [4], and the evolution of the beam radius $w_\Omega(z)$ (still at $1/e^2$) as a function

of the propagation distance z from the focus is given by

$$w_\Omega(z) = w_{\Omega,0}\sqrt{1 + \left(\frac{z}{z_R}\right)^2}, \quad z_R = \frac{\Omega w_{\Omega,0}^2}{2c} \tag{2.74}$$

with z_R representing the Rayleigh range, defined as the distance from the waist at which the area of the cross section is doubled. If the collimating element is placed at a distance $z = f$, the corresponding beam radius $w_\Omega(f)$ can be approximated to

$$w_\Omega(f) \approx w_{\Omega,0}\frac{f}{z_R} = \frac{2cf}{\Omega w_{\Omega,0}} \tag{2.75}$$

as long as the condition $f \gg z_R$ is respected, which is generally true in real cases.

Since the beam intensity distribution is Gaussian, the fraction of power $T_{parax}^2(D,\Omega)$ collected by the circular OAPM with diameter D at a distance f from the focal point can easily be calculated by integrating the Gaussian power distribution over the mirror's surface and dividing the result by the total power, obtained with integration of the same integrand over the whole space

$$T_{parax}(D,\Omega) = \frac{P(D,f)}{P_0} = \frac{\int_0^{D/2} \exp[-2r^2/w_\Omega^2(f)]r\,dr}{\int_0^\infty \exp[-2r^2/w_\Omega^2(f)]r\,dr} \tag{2.76}$$

where $P(D,f)$ and P_0 are the collected and total power, respectively, and r represents the radial coordinate. Solving the integrals, we obtain an amplitude transfer function $t_{parax}(NA,\Omega)$ equal to

$$t_{parax}(NA,\Omega) = \sqrt{T_{parax}^2(NA,\Omega)} = \left\{1 - \exp\left[-\frac{\Omega^2 w_{\Omega,0}^2(NA)^2}{2c^2}\right]\right\}^{1/2} \tag{2.77}$$

where we introduced the numerical aperture (NA) of the OAPM, defined as $NA = D/2f$.

Actually, if the pump beam is tightly focused, e.g. $w_p = 10\mu m$, the paraxial approximation does no longer hold for THz frequencies lower than 10 THz, making the previous analysis invalid. In other words, for the aforementioned low frequencies, the corresponding wavelengths are comparable or even larger than the beam waist, i.e. $kw_{\Omega,0} < 1$, making the beam diverge much more rapidly than predicted by the paraxial approximation in eq. 2.74. In such a regime, Bethe's diffraction theory [58,61] is better suited to describe the propagation of the THz beam: the typical diffraction length z_B is now given by

$$z_B = \frac{k^2 w_{\Omega,0}^3}{2} = \frac{\Omega^2 w_{\Omega,0}^3}{2c^2} \tag{2.78}$$

To obtain an accurate result for the collection of power in this condition, one would need to follow the rather complicate Bethe's analysis [61]. For the current work, it is sufficient to use a heuristic function, introduced by Faure *et al.* [58], which determines the amplitude transfer function $t_{coll}(NA, \Omega)$ after the collection

$$t_{coll}(NA, \Omega) = \left\{ 1 - \exp\left[-\frac{2(NA)^2 z_{coll}^2}{w_{\Omega,0}^2} \right] \right\}^{1/2}, \quad \text{with } z_{coll} = \begin{cases} z_B & \text{if} \quad k w_{\Omega,0} < 1 \\ z_R & \text{if} \quad k w_{\Omega,0} > 1 \end{cases} \tag{2.79}$$

2.8 Electronic Detection Techniques

Now we can discuss some of the electronic detection methods that are employed in the measurement of THz waves. These techniques are of fundamental importance because they allow to separate the weak signal from a very noisy background, leading to a high SNR.

2.8.1 Balanced Photodetection

Balanced photodetection is a technique able to detect very small differences in optical power between two optical input signals, while suppressing most part of their common fluctuations [62]. Indeed, a large source noise for experiments where the signals are very weak is due to the intensity noise, which basically consists in fluctuations of the optical intensity of the light source. Hence, by operating the difference between two inputs that originates from the same source, this noise can be largely canceled out and the system is said to have a good common mode rejection.

The working principle is rather straightforward: looking at the electronic circuit shown in panel (a) of fig. 2.12, two photodiodes are placed in series, in such a way that the generated photocurrents cancel each other when the same amount of light hits the two diodes. Then, the resulting differential signal passes through a transimpedance amplifier, which converts and amplifies the current signal into a voltage one.

2.8.2 Lock-in Detection

Sensitive experiments often requires to retrieve very weak signals from extremely noisy backgrounds. State-of-the-art systems are able to accurately measure signals that are million times weaker than the surrounding noise components [63]. An example of such techniques is the lock-in amplifier based detection.

Lock-in amplifiers employ a homodyne detection scheme together with low-pass filtering, resulting into a behavior similar to a high-performance tunable band-pass filter. Indeed,
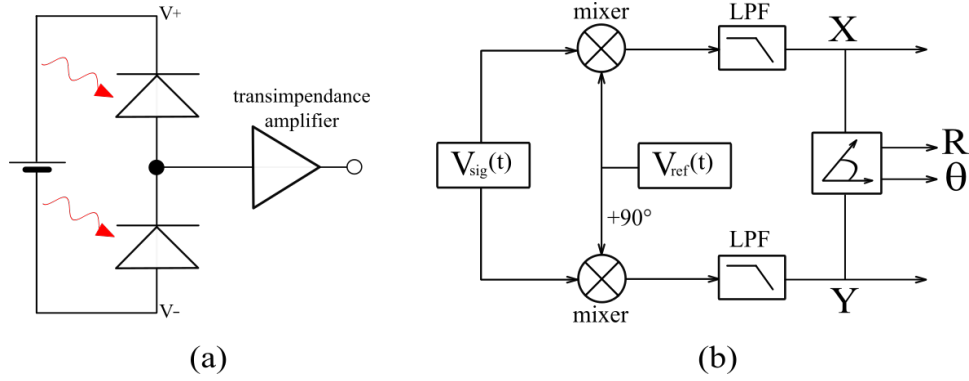
Figure 2.12 (a) Basic electronic circuit of a balanced photodetector: the differential current signal, originating from the two diodes placed in series, goes through the transimpedance amplifier and is converted into a voltage signal. (b) Basic scheme of a lock-in detection system: the signal to be measured $V_{sig}(t)$ is split in two and mixed with the two quadratures of the reference signal $V_{ref}(t)$; the resulting mixed signal undergoes low-pass filtering (LPF). Depending on the case, both cartesian and polar components of the signal are available.

this method allows to isolate the signal centered at the frequency of interest f_{sig} from all the other unwanted frequency components. The working principle is shown in fig. 2.12(b): the input signal $V_{sig}(t)$ is split in two parts and then separately multiplied, respectively, with the reference signal $V_{ref}(t)$ and with a 90° phase-shifted copy of it. V_{ref} is either a pure sinusoid or a square wave, oscillating at the same frequency of $V_{sig}(t)$. For this reason, above we referred to a homodyne scheme, given that $f_{ref} = f_{sig}$. The output of the mixers consequently presents strong frequency components at DC and at $2f_{sig}$, as it will be shown below. Subsequently, an adjustable low-pass filter (LPF) is applied to each branch in order to suppress all the undesired frequency components. At this point, the in-phase X and quadrature Y components of the signal are obtained and, if needed, they can be easily converted into the amplitude R and phase θ components via a trivial transformation from cartesian to polar coordinates.

To intuitively understand why such a combination of frequency mixing and low-pass filtering is able to efficiently reconstruct the signal, we will follow an analysis that moves across the time and the frequency domains [64]. Let us consider a weak sinusoidal signal oscillating at f_{sig}: fig. 2.13(a) represents the signal in the time domain, while fig. 2.13(b) shows the signal spectral components, computed via Fourier transform. The sinusoidal component of the trace coincides with the Dirac delta functions at $+f_{sig}$ and $-f_{sig}$; then we remark the presence of a direct current (DC) smaller peak due to the input signal's DC offset and some noise at other frequencies. Fig. 2.13(c) illustrates the spectrum of the signal after mixing (also called demodulation), which is essentially a copy of the spectrum shown in panel (b), but with the

Dirac delta functions shifted towards lower frequencies by an amount equal to f_{sig}. Hence, we notice that the signal we are interested in, originally centered at f_{sig}, is now centered around zero-frequency. In addition, the dashed line represents the transfer function of the LPF, which means that only the small bandwidth $2f_{BW}$ "survives", while the noise and other unwanted components are canceled out. Finally, by operating an inverse Fourier transform, we obtain the time dependence of the mixed and filtered signal: fig. 2.13(d) reports the signal after the mixer (blue line) as a function of time and the same signal but after the low-pass filter (black line), which corresponds exactly to the DC component contained within the LPF bandwidth in panel (c).
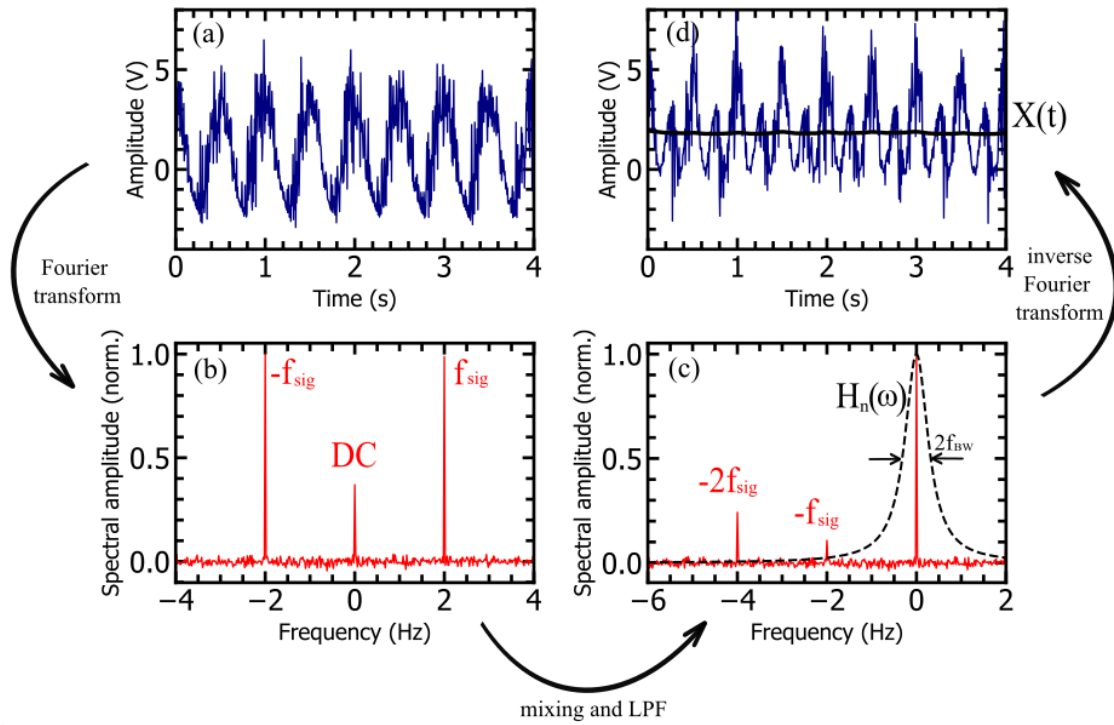

Figure 2.13 Representation in time and frequency domain before and after the lock-in demodulation process and low-pass filtering. (a) Time representation of input signal V_{sig} oscillating at f_{sig} superimposed with noise. (b) Spectral components of the signal shown in (a) obtained via Fourier transform. (c) Representation in the Fourier domain of the frequency-mixing with the reference signal, which causes a shift by $-f_{sig}$ of the spectral components in (b). $H_n(\omega)$ is the transfer function of the LPF with bandwidth $2f_{BW}$. (d) Time domain picture of the input signal mixed with the reference signal V_{ref} before (blue trace) and after (black trace) low-pass filtering.

As an additional proof that the demodulation results in a down-shifting of the spectral components by f_{sig}, we can look at the process in the time domain. The input sinusoidal

signal oscillating at f_{sig} can be written as

$$V_{sig}(t) = \sqrt{2}R\cos\left(2\pi f_{sig}t + \theta\right) = \frac{R}{\sqrt{2}}\left(e^{i(2\pi f_{sig}t+\theta)} + e^{-i(2\pi f_{sig}t+\theta)}\right) \qquad (2.80)$$

Similarly, the complex reference signal (assuming $f_{sig} = f_{ref}$) can be expressed as

$$V_{ref}(t) = \sqrt{2}e^{-i(2\pi f_{sig}t)} \qquad (2.81)$$

The signal resulting from the mixing is then

$$Z(t) = V_{sig}(t)V_{ref}(t) = R\left[e^{i\theta} + e^{-i(2\pi 2 f_{sig}t+\theta)}\right] \qquad (2.82)$$

where it is evident the presence of a DC component and one at twice the signal frequency. The choice of the LPF bandwidth is non-trivial. On the one hand, the filter bandwidth must be much smaller than the signal frequency in order to efficiently suppress the input DC-offset (which is moved at f_{sig} after mixing) and to get a better noise reduction. On the other hand, the smaller is the bandwidth the longer is the integration time, which translates in a longer waiting time between two measurements. Hence, there is a practical limitation on the minimum filter bandwidth, dictated by the maximum possible time taken for each measurement. In addition, in an ideal case the response function of the LPF is a perfect step function, such that the transmission of the frequency components below f_{BW} is 1, while for all the other frequencies the transmission is 0. However, it is impossible to realize this kind of LPF, because it implies that its response would extend to infinite in both time directions. A good feasible solution is to imply cascaded RC filters, which are easy to implement in both analog and digital domains. The frequency response $H_n(\omega)$ of a nth order filter, which means that n RC filters are put in series, is well approximated by the following equation

$$H_n(\omega) = \left(\frac{1}{1 + i\omega\tau}\right)^n \qquad (2.83)$$

where $\tau = RC$ is defined as the time constant of a LPF with resistance R and capacitance C. The bandwidth of an RC filter corresponds to the cut-off frequency f_{-3dB}, which is defined as the frequency at which the signal power is reduced by one half, or equivalently, by $-3dB$. Hence, looking at eq. 2.83, it is clear that to get a smaller bandwidth we need a higher time constant, in other words a longer integration time, as it was previously stated. Finally, the higher is the order of the RC filter, the more its transfer function resembles a perfect step function, but once again the larger is the time required by the LPF to work properly, increasing the waiting time between two measurements.

CHAPTER 3   EXPERIMENTAL SETUP

In this chapter we describe in details the elements included in the conceived experimental setup, represented in fig. 3.1. After characterizing the excitation source used to drive the experiment, we introduce the optical components needed to generate THz transients via OR and to demonstrate the functionality of a proof-of-principle field-resolved detection scheme
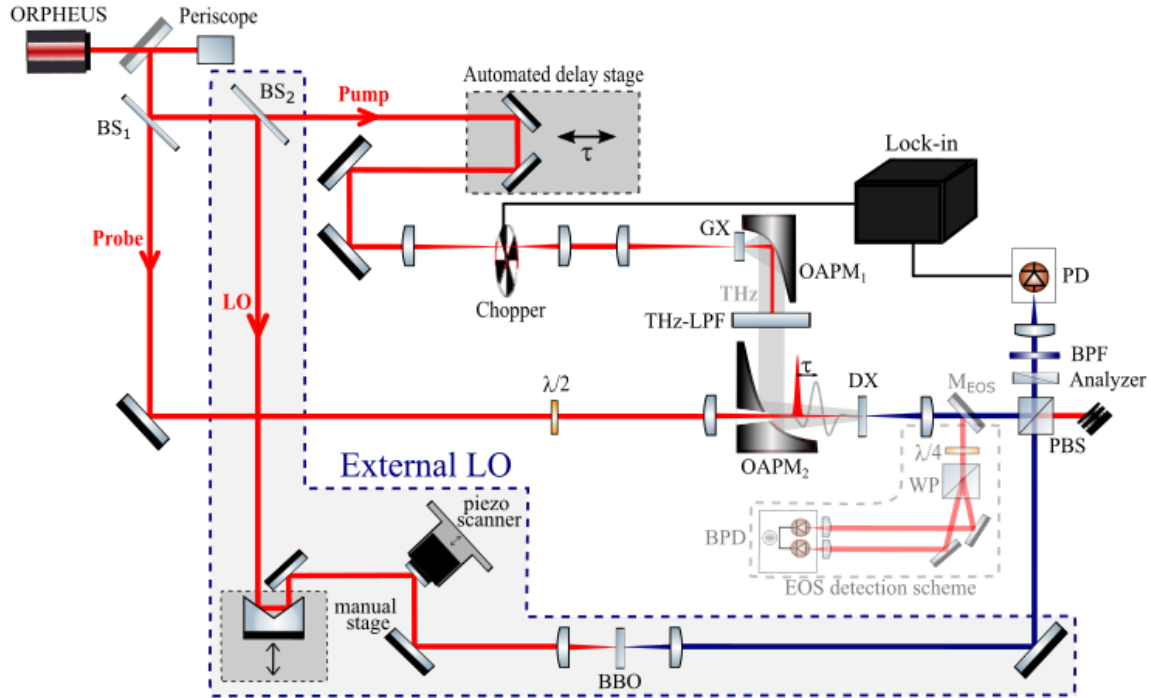

Figure 3.1 Scheme of the experimental setup for generation, via OR of ORPHEUS' idler laser pulses (sec. 3.1), and resolution of terahertz (THz) transients via homodyne detection of the TFISH signal, generated in solid-state media. ORPHEUS' pulses are split in three by the two beamsplitters (BS$_{1,2}$): the pump beam generates THz signal inside the generation crystal (GX), which is then collected and refocused on the detection crystal (DX) by a pair of 90° off-axis parabolic mirrors (OAPM$_{1,2}$). The linear polarization of the probe beam is rotated with a half-wave plate ($\lambda/2$) to get the best phase matching for the FWM process (see appendix A). The local oscillator (LO) field can be obtained either from the DX itself or via SHG in a beta-barium borate (BBO) crystal, in which case it is recombined with the TFISH field via a polarizing beamsplitter (PBS). Afterwards, an analyzer and an optical band-pass filter (BPF) help in isolating the desired interference term, detected by a photodetector (PD). In parallel, the THz source can be characterized via an EOS detection scheme, constituted by a quarter-wave plate ($\lambda/4$), a Wollaston prism (WP), a balanced photodetector (BPD), and accessible when the mirror M$_{\text{EOS}}$ is in place.

for THz fields, based on terahertz-field-induced second-harmonic generation (TFISH) in solid-state media. The generated THz pulses are also characterized by an electro-optic sampling (EOS) scheme, built in parallel to the main detection scheme, with the goal to yield a benchmark of the THz source [3, 28, 46, 56].

3.1   Laser System

The laser source used in this work (see fig. 3.1) is the output beam (idler) of a broad bandwidth collinear two-stage optical parametric amplifier (ORPHEUS-F) from the company Light Conversion. The OPA is pumped with pulses coming from a femtosecond laser system (PHAROS), provided by the same company.

PHAROS laser system includes a Kerr lens mode-locked oscillator (refer to section 2.2) and a regenerative amplifier. Both units present ytterbium-doped potassium gadolinium tungstate (Yb:KGW) as gain medium. The output pulses are characterized by a duration of around 260 fs and by a spectrum with central wavelength at 1026 nm and full width at half maximum (FWHM) of 8.2 nm. The pulse energy is 20 μJ and the repetition rate can be tuned from single shot up to 1 MHz with the help of a computer-controlled pulse picker located at the output of the regenerative amplifier.

ORPHEUS produces two output beams, the signal and the idler, and it emits pulses with central wavelength tunable over the range 650 - 2500 nm. The duration of the pulses depends on the chosen wavelength, and in general it varies between 40 and 60 fs. Similarly, the energy of the pulses at the output is wavelength-dependent, since it is dictated by the efficiency of the OPA process.

ORPHEUS contains the typical subunits presented in appendix B within a thermally-stabilized compact housing. In order to avoid the damaging of nonlinear crystals and optical components within ORPHEUS, a 75% beamsplitter redirects roughly 14.6 μJ pulses coming from PHAROS to the OPA input. Then, this pump beam is split in two: a small part is focused on a sapphire plate to generate a stable single-filament white-light seed, while the remaining large fraction is dedicated to generate SH, which will act as the pump source for the two successive OPA processes. The white-light beam passes through a temporal dispersion system where the pulse is dispersed in time due to group velocity dispersion. In other words, the spectral components of the pulse are delayed with respect to each other since they present different group velocities inside the dispersive medium. The delay of the white-light pulse can be tuned via a motorized stage, allowing to temporally overlap only a certain spectral region of white light with the pump pulse inside the nonlinear crystal, where the first amplification

stage (preamplifier) takes place. This stage consists in a non-collinear OPA because the two beams intersect each other at a precise angle, with the goal to exploit at best the phase matching of the nonlinear process and get amplification over a large bandwidth. This way, the preamplifier produces stable and broadband seed pulses ready to be further amplified in the second (collinear) amplification stage. Due to the collinear nature of the second OPA stage, amplified idler and signal beams are spatially overlapped and they propagate along the same direction. As a consequence, proper dichroic mirrors are used to separate them: signal wavelengths are reflected, while idler ones are transmitted.

Finally, both idler and signal pulses need to be compressed to obtain the corresponding transform-limited duration. In particular, amplified signal pulses present positive dispersion, which can be compensated via prism pair compressor [4,34,65]. On the other hand, amplified idler pulses are characterized by negative dispersion. Hence, pulse compression is achieved simply by adding a slab of material with normal dispersion along the idler beam path.

3.1.1 Choice of the Fundamental Wavelength and Corresponding Pulse Duration

The advantage of using an OPA as laser source is that there is a certain flexibility in the choice of the wavelength that will be used to realize the experiment. Phase matching simulations for the four-wave mixing (FWM) processes responsible for TFISH generation show that for the centrosymmetric materials particularly suited for this technique (e.g. diamond, as discussed in subsection 2.5.2), the larger is the wavelength of the fundamental beam the better is the phase matching. This in turn means that larger crystal thicknesses can be adopted, leading to a larger contribution to the signal to be measured, without losing in terms of detection bandwidth.

Even though more details regarding the FWM phase matching calculations are provided in appendix A, we can sum up those results by saying that, considering terahertz frequencies below 10 THz, the coherence length is around 25 μm when the excitation source wavelength is 1.55 μm, while it increases by roughly a factor of 2, 4 and 10 when the fundamental wavelength is, respectively, 2, 2.5 and 3.2 μm. Unfortunately, the laser source introduced above cannot be pushed in the mid-IR, and the energy curve of the OPA's idler pulses is such that at 2.5 μm the pulse energy is only of 100 nJ, which would likely lead to very weak nonlinear signals, and thus to low signal-to-noise ratios, making the finding of the desired signal and its optimization rather difficult. Furthermore, from an experimental point of view, the alignment of all the optical elements in the setup is significantly simplified when using wavelengths in the telecommunication window, i.e. around 1.55 μm, because it is easy to see the laser beam

with proper laser viewing cards. This, together with the fact that at 1.55 μm the pulses from ORPHEUS' idler are more energetic and that the detection of THz via electro-optic sampling in ZnTe has already been demonstrated [46], convinced us to choose this wavelength as excitation source for our THz measurement system. Additionally, achieving proof-of-principle THz generation and detection at this wavelength is of fundamental importance in the outlook of transferring this free-space setup onto an integrated photonic device because all the advantages of fiber laser technology can be immediately exploited. Regarding the non-optimal phase matching at 1.55 μm, the coherence length can be substantially improved by employing properly-cut birefringent materials, such as silicon carbide, as the medium responsible for the FWM. From now on, unless specifically stated otherwise, the laser source is considered to be centered at 1.55 μm.

At this point, it is important to completely characterize the laser pulses that will be used as excitation source for multiple reasons. Firstly, having an accurate estimate of the pulse width allows us to get an idea of the range of THz frequencies that can be generated and detected, since the THz spectral bandwidth is intrinsically related to the optical pump pulse duration, as discussed in section 2.6. Secondly, the nonlinear processes exploited in this work require to keep peak intensity values within a certain range: high enough to make the nonlinear effect relevant, but not too high to cause damages to the nonlinear media. Hence, reminding that the peak intensity is related to both the temporal and spatial profiles of the pulse, once the

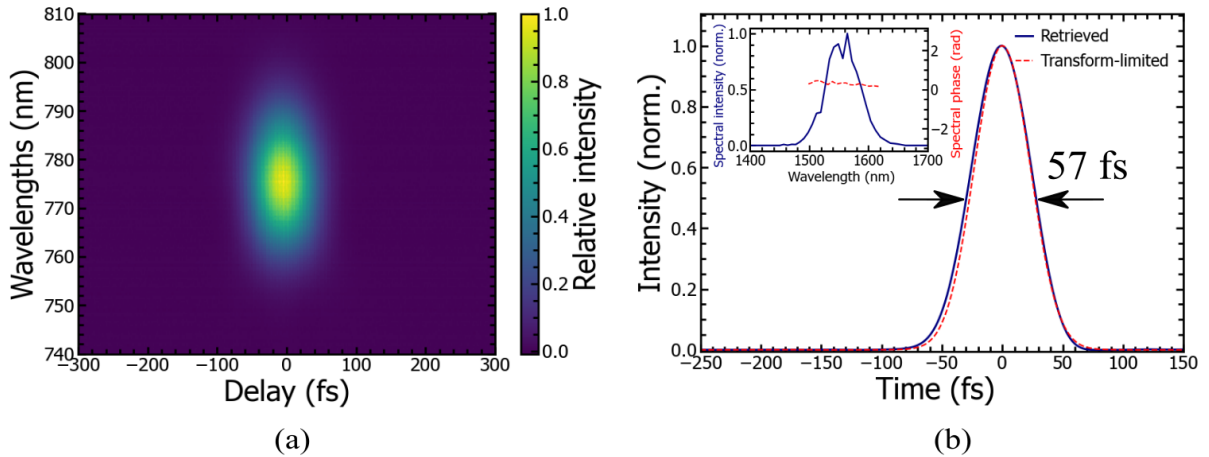Figure 3.2 SHG-FROG measurement of ORPHEUS' idler centered at 1.55 μm. (a) Acquired FROG trace, presenting the spectral intensity as a function of the relative delay. (b) Reconstructed pulse (blue line) in the temporal domain, with FWHM of 57 fs approximately, and corresponding transform-limited pulse (red line) with FWHM of 54 fs. The retrieved spectral intensity and phase are presented in the inset.

temporal width is known, we can determine the proper spatial focusing needed to achieve those values. Finally, characterizing the spectral phase helps us to understand if the pulse presents the shortest duration achievable for a given spectral width, i.e. if it is close to the transform-limited duration.

The full characterization of the pulse electric field (more details in section 2.3), in terms of spectral intensity and phase, was executed using a home-built portable SHG frequency-resolved optical gating (SHG-FROG) [37], already available in the lab. The FROG trace is presented in panel (a) of fig. 3.2, while panel (b) depicts the retrieved temporal profiles of the actual pulse and of the corresponding transform-limited one. The measurement proves that the pulse is already well compressed by ORPHEUS' bulk compressor, given the actual duration (57 fs) being very close to the Fourier-limited duration (54 fs). Furthermore, the rather flat profile of the spectral phase, presented in the inset, indicates a weak *GVD* and *TOD*, suggesting that the small difference (less than 5%) in pulse width is probably due to dispersion terms higher than the third, which are not easily compensated with standard compensation techniques [4, 34]. For these reasons, added to the fact that the gain in peak intensity by reducing the pulse duration would be likely counteracted by the losses of non-ideal optical elements in dispersion compensation strategies, we decide to not further compress the pulse.

Given the measured pulse duration, in the following we will focus our attention to terahertz signals with spectra below 10 THz, roughly, since this is the range of frequencies that we can realistically generate and detect, as mentioned at the end of subsection 2.6.1.

3.2   Terahertz Generation-Detection System Design

The laser beam coming out of ORPHEUS' idler port, whose $1/e^2$ diameter is of 4 mm, is redirected to the region of the optical table where the setup is located with the help of silver-coated flat mirrors. Then, as shown in fig. 3.1, the beam is sent to a periscope in order to change its elevation: ORPHEUS' board outputs a beam at a height of 125 mm with respect to the optical table, but in order to reduce the noise induced by vibrations of the optical elements as much as possible, we decide to lower it to 75 mm. This height is the minimum one that does not pose any experimental issues, in particular it guarantees proper bouncing on mirrors mounted on the linear translation stage employed in this setup, which will be discussed later. The periscope is built by gluing two right-angle prism mirrors to a home-built aluminum enclosing structure, which helps in getting a safer and less fragile element.

Afterwards, a set of two irises is placed to allow a first alignment into the main setup with the help of a couple of mirrors located along the beam path. At this level, the energy of the laser pulses is around 500 nJ, and the difference with respect to the nominal energy of 550 nJ is attributed to the multiple reflections on mirrors located in between the OPA's output and the beginning of the setup. BS_1 is the beamsplitter that marks the entrance of the THz generation and detection setup, splitting the energy of the laser pulses roughly in half: the tabulated reflectance of such beamsplitter is actually 53% for s-polarized light, which is the polarization of the OPA's idler, while proper anti-reflection coating on the wedged back surface minimizes spurious back-reflections and it guarantees close to 46.5% in transmission. The beamsplitter is a 5 mm thick calcium fluoride (CaF_2), material that has basically negligible dispersion ($GVD \leq 100$ fs^2/mm [66]) throughout the entire near and mid-IR regions, leaving the possibility to make the current setup work also with fundamental wavelengths in those regions. From now on, the reflected beam is referred to as the pump, while the transmitted one is the probe beam. The choice of the beamsplitting ratio is to ensure sufficiently energetic pulses in both arms since each one has to drive nonlinear optical effects: the pump pulses are the source of THz via OR, while the probe ones generate the TFISH to coherently detect the THz field.

Let us focus on the pump branch. After being reflected by BS_1, the pump beam reaches the delay stage, whose goal is to control the temporal delay τ between pump and probe pulses, achieving full reconstruction of the THz transient. Two mirrors are mounted at a right angle on top of the M-403.6DG cost-optimized linear translation stage, provided by Physik Instrumente. This Python-controllable stage has a travel range of 150 mm with minimum incremental motion of 0.2 μm and repeatability of 1 μm. From a time delay perspective, this translates to minimum temporal increments of 1.3 fs, with repeatability of 6.7 fs, and a 0.12 fs time resolution, enabling sampling of an optical signal at 10 THz with less than 0.12% uncertainty of its period.

After the delay stage and another pair of irises, used to adjust the alignment of the pump arm independently, an optical chopper blade is positioned along the beam path in order to modulate the generated THz beam and improve the signal-to-noise ratio (SNR) via lock-in detection (see subsection 2.8.2 for more details). Indeed, this rotating wheel alternates cut through and dark sections, blocking and letting through the pump beam with a frequency set by the Thorlabs chopper controller MC2000B. Ideally, we would like the modulation frequency to be as high as possible to move out of the region where noise is pretty intense due to mechanical or ambient noise sources. However, the chopper is intrinsically limited to few kHz, in terms of maximum frequencies that it can reach, and this comes at the cost of creating rather intense air turbulences and mechanical vibrations. In fact, to partially

alleviate the noise due to the fast rotation, we can employ blades with a larger number of slots. For instance, for a given modulation frequency, if the number of slots is 100 instead of 10, the angular velocity is reduced by a factor of 10. The price to pay is that the width of the slot gets significantly smaller, requiring the use of an optical telescope to reduce the size of the beam and ensure proper on-off modulation. For this reason, the Thorlabs chopper blade MC1F10HP, with 1.36 mm wide slots in the external region, is placed in the focal point of a lens with 80 mm focal length, which reduces the beam diameter well below the size of the slot.

Once the beam is properly recollimated, it is focused onto the generation crystal (GX), responsible of generating THz transients via OR, as introduced in sections 2.5 and 2.6. The GX is mounted on a manual 3D linear translation stage with micrometer precision, which gives the opportunity to fine-tune the transverse (x-y plane) and longitudinal (z axis, corresponding to beam propagation direction) positions of the crystal with respect to the beam focal point.

Finding the proper focusing condition for the pump beam is not trivial. Although a smaller focused beam waist is beneficial to boost the spatial compression and thus the pulse peak intensity, favoring the nonlinear process inside the GX, other constraints impose a minimal focus size. Indeed, we need to consider that when a pulse with energy of about 200 nJ, as in our case, is strongly focused in a nonlinear crystal, multiple processes can take place at the same time, besides the desired phenomenon, causing a complicate interplay of nonlinear effects. For instance, when high enough peak intensities are reached, higher order nonlinear processes become relevant inducing self-phase modulation, self-focusing (see subsection 2.4.2) and sometimes even multi-photon absorption, which might all result in distortion and losses of the THz signal. Not to mention that these phenomena increase the possibility of optical and thermal damages to the GX. Furthermore, according to eq. 2.79, a smaller pump beam waist implies a reduction of the collected THz power as a result of a stronger divergence. In order to quantify the losses of the THz signal due to finite extension of the collimating element (OAPM$_1$), whose characteristics are described below, the frequency-dependent amplitude collection efficiency is computed and presented for multiple focused pump beam $1/e^2$ diameters ($2w_p$) in fig. 3.3.

We immediately realize that for frequencies below 1 THz the collection efficiency is lower than 10% when $2w_p$ is 25 and 50 μm (blue and orange lines), hence these focusing conditions cause significant losses that risk to seriously complicate the detection of the signal. On the other hand, looking at the other two curves (green and red), at 1 and 2 THz the two efficiencies are both larger than 25% and 60%, respectively, and they approach 100% around 4 THz.
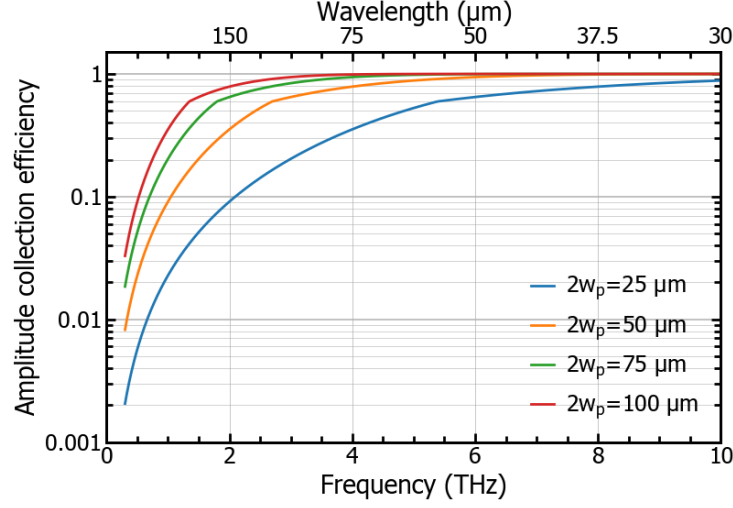
Figure 3.3 Amplitude collection efficiency of the generated THz beam, in the frequency range of interest, by an off-axis parabolic mirror with 20.3 mm focal distance and 38.1 mm diameter ($NA = 0.94$) for multiple focused pump beam waists w_p. Each curve is computed exploiting the heuristic function introduced in eq. 2.79 and the sharp variation (e.g. around 5.5 THz for the blue line) corresponds to the frequency at which Bethe's approximation is replaced by the paraxial approximation (see section 2.7).

Hence, both conditions constitute viable options. However, since the peak intensity scales quadratically with the inverse of the beam waist w_p, the best option consists in a focused beam diameter of 75 μm because the increase in peak intensity overcomes the smaller collection efficiency, assuming that the saturation threshold is not yet reached.

With a collimated pump beam diameter of 4 mm, exploiting the laws of Gaussian optics [4], the focal length needed to achieve the aforementioned beam waist diameter is 150 mm. However, to keep the setup more compact, the optical telescope mentioned above can be set so that the output beam has a size equal to half of the input one, by using a collimating lens with half the focal length of the focusing one. This way, the focusing element right before the GX in fig. 3.1 is a 75 mm lens and the $1/e^2$ beam diameter is confirmed to be of about 77 μm, measured with a CMOS camera. All the lenses mentioned so far are made of calcium fluoride in order to minimize the dispersion added to the pump beam.

The generated THz signal is collected and recollimated by a 90° off-axis parabolic mirror (OAPM$_1$), located at a distance from GX equal to its focal length. OAPMs are the best suited optical elements for collection of THz beams because they do not add any chromatic dispersion, avoiding distortion of the THz pulse due to dispersive propagation and absorption, and they minimize geometrical aberrations, typically induced by spherical mirrors and lenses.

In particular, spherical aberrations is a relevant issue for the range of THz frequencies that we aim to generate, i.e. below 10 THz, because they tend to diverge more strongly than higher THz frequencies, according to Bethe's diffraction theory introduced in section 2.7. In other words, lower frequencies achieve significantly larger spot size at the level of the collimating element and therefore they would suffer more from this type of aberration if spherical surfaces were employed.

As a consequence of the rapid divergence of the low THz frequencies, the collimating OAPM is chosen to have the largest possible numerical aperture (NA), defined as the ratio of the diameter over twice the focal length of the mirror, with the goal to collect the largest portion of the generated THz beam. At the same time, we must not discount the experimental issues that a large NA inherently brings: the size and focal length of $OAPM_1$ must allow to physically place it exactly at the focal distance from the GX, otherwise the collimation is compromised. The best candidate commercially available to fit our needs is a gold-coated OAPM from Newport, with an effective focal length f_{OAPM_1} and a diameter D_{OAPM_1} of 20.3 and 38.1 mm, respectively, as illustrated in panel (a) of fig. 3.4. The NA is then 0.94. The focal point is displaced from the mechanical axis, yielding complete access to the reflector focus area. The root mean square (RMS) reflected wavefront error is smaller than $\lambda/2$ at 633 nm, and thus smaller than $\lambda/190$ for the longest wavelength that we are interested in generating.

Once we ensure the proper generation and collection of the THz transient, the following step is to recombine this beam with the probe in a collinear geometry, dumping the residual pump beam before the recombination. These two operations are fundamental for the success

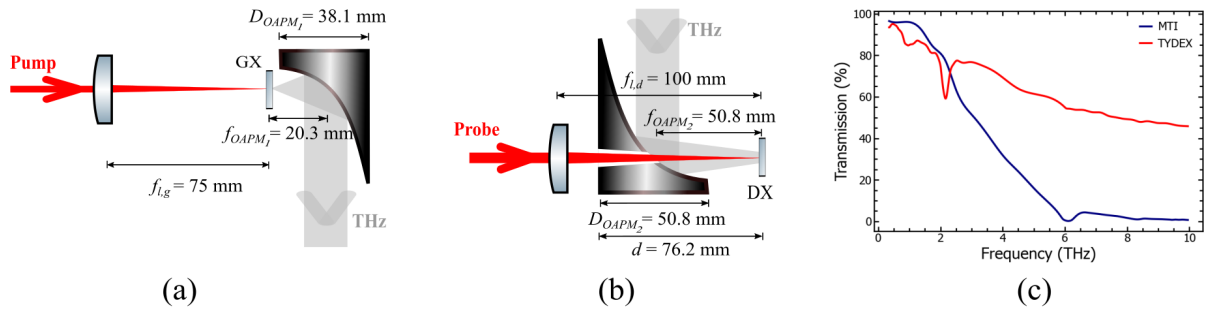Figure 3.4 (a) Specifications of the lens and the OAPMs used, respectively, to focus the pump beam on the generation crystal (GX) and collimate the resulting THz beam. (b) Characteristics of the OAPM that focuses the THz beam on the detection crystal (DX) and of the lens responsible of focusing the probe at the same focal plane. (c) Transmission of the selected THz low-pass filters as a function of frequency [67, 68].

of such pump-probe experiment, but highly non-trivial. First, without recombination of the THz and probe beams, the nonlinear process exploited as THz detection cannot take place. Second, the light collected by OAPM$_1$ includes both the THz beam and the residual of the fundamental beam which is not converted. If the latter reaches the photodetector, it will give rise to a strong linear interference with the probe beam, hiding entirely the weaker interaction between the THz and probe beam.

Hence, ideally we would need a special dichroic mirror, capable of reflecting wavelengths in the near-IR region while transmitting only the desired THz radiation, achieving both tasks at once. However, given the excitation wavelenght used in this work, i.e. 1550 nm, a material with such properties is not available and we are forced to keep the actions of recombination and filtering separated. For the former, we can take advantage of the substantially large diameter of the THz beam and employ a 90° OAPM with a small through hole for the probe beam, strategy that is commonly used in THz generation-detection setup [27, 28]. This way, the collinear superposition is obtained and the loss of THz radiation is rather limited. A lens placed along the probe path before OAPM$_2$ allows to focus it in the same focal plane of the THz beam.

Since the lens must be physically located before the parabolic mirror, its focal distance is intrinsically limited by the focal length and thickness of the OAPM, otherwise it would be impossible to get overlap of the two foci. Therefore, OAPM$_2$ needs to present a rather short focal distance to achieve tight focusing of both the THz and the probe beam, which we remind has to be intense enough to efficiently drive a third-order nonlinearity to generate TFISH. Additionally, OAPM$_2$ has to present a diameter larger or equal than the one of OAPM$_1$ to completely collect the incoming THz beam. The best compromise available on the market is a gold-coated OAPM with through hole from Thorlabs, with diameter D_{OAPM_2} and focal length f_{OAPM_2} of 50.8 mm, earning $NA = 0.5$. The RMS reflected wavefront error is smaller than $\lambda/2$ at 633 nm, hence the same discussion presented for OAPM$_1$ holds. The probe goes through an achromatic half wave-plate used to rotate its linear polarization along the desired axis to improve phase matching of the four-wave mixing. Then, it is focused using a CaF$_2$ lens with a focal length $f_{l,d}$ of 100 mm, which is the shortest distance physically exploitable (at least larger than the distance d between the input of the through hole and the focus) that respects our criteria, as depicted in fig. 3.4(b). OAPM$_2$'s hole has an 8 mm diameter as entry port in the back of the mirror (on the left side of fig. 3.4(b)) that tapers down to 3 mm diameter as exit port in the mirror reflective surface (on the right side of fig. 3.4(b)).

Regarding the filtering of the pump residual, we place a THz low-pass filter (THz-LPF in fig. 3.1) made of a material that is opaque and diffusive for visible and near-IR wavelengths,

while almost completely transparent for THz radiation. More specifically, two filters have been selected as possible THz-LPF: one provided by Microtech Instruments Inc. (MTI) and the other from Tydex. The respective transmission in the THz range is reported in panel (c) of fig. 3.4. The first one presents a transmission larger than 80% below 2 THz, gradually decreasing to less than 10% at 6 THz, after which the transmission is rather compromised. The rejection of the fundamental beam is fairly high, since only 0.1% of the radiation in this spectral range is transmitted. The second one works well (between 40% and 80% transmission) up to 10 THz, but the rejection ratio for the residual of the pump beam is worse than the other filter, letting through up to 1% of the radiation. Therefore, if the detected signal contains frequency components up to 10 THz, Tydex's filter is theoretically better suited, while for THz spectra below 4 THz MTI's product should be a better option because it potentially leads to a slightly higher SNR, having higher THz transmission in this range and better extinction ratio for the leakage.

It is worth mentioning that the pre-alignment of the second off-axis parabolic mirror is rather tricky due to the presence of the hole on its reflecting surface. Obviously, since the THz beam is out of the spectral response of any CMOS camera, it cannot be used to adjust the alignment of $OAPM_2$. This leaves us with the only option of temporally removing the THz-LPF and using as a reference the non-converted fundamental beam, which is detectable with the camera. However, the collimated pump beam size is so small that the fraction "surviving" the hole is not enough to reach the sensitivity threshold of the camera. To solve this issue, a neat strategy consists in placing a pinhole at the generation focal point, exactly in the center of the beam transverse profile, with a smaller diameter compared to the pump beam waist (77 μm). This induces a stronger divergence, leading to a larger size of the collimated beam and thus to a greater fraction reflected by $OAPM_2$, able to be imaged with the camera.

As for the GX, the detection crystal position can be fine-tuned along the x, y, z axes with the help of a manual 3D linear translation stage with micrometer precision. This time however, in addition to the these degrees of freedom, also a manual rotation stage (coarse and fine rotation over 360° and ±5°, respectively) is added to give the possibility to adjust the angle of incidence θ, between the wave vector and the optical axis (see fig. 2.8), by rotating the DX around the axis perpendicular to the optical table. This is particularly important when the material used as DX is birefringent (see subsection 2.4.3) because it allows to find the best phase matching angle and optimize the detection efficiency.

The remaining part of the setup is dedicated to the coherent detection of the THz transients. The main THz detection scheme used in this work is based on the mixing of the TFISH
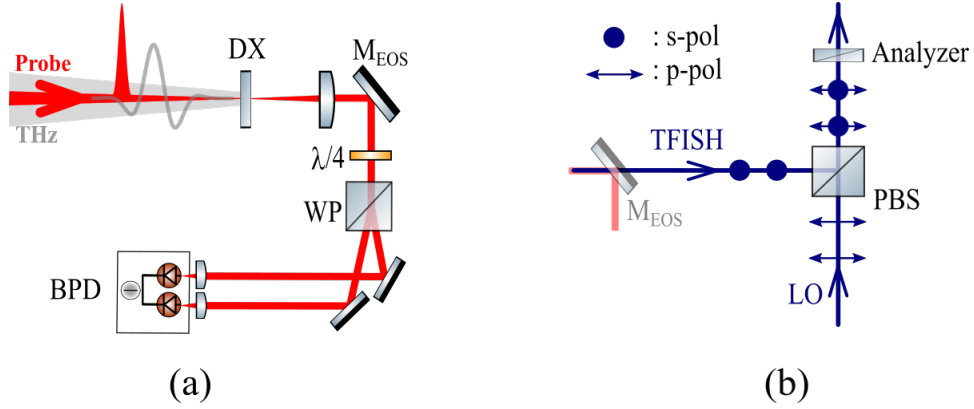
Figure 3.5 Details regarding the part of the setup dedicated to the detection of THz transients. (a) Probe beam is deviated towards the EOS detection scheme when the mirror M_{EOS} is in place: the beam encounters in sequence an achromatic quarter-wave plate ($\lambda/4$) and a Wollaston prism (WP), before being detected by a balanced photodetector (BPD). (b) Recombination of the s-polarized TFISH and p-polarized external LO beams at the polarizing beamsplitter (PBS) to get both beams at the same output port. Afterwards, the linear interference is made possible with an analyzer at 45°.

signal generated in solid-state media with a second-harmonic bias serving as local oscillator field. However, in order to optimize the generation (e.g. orientation of the GX, position of the GX with respect to the focus, etc.) and get a first characterization of the terahertz source we assemble the very common and easy-to-implement electro-optic sampling (EOS) detection scheme. By building the two setup in parallel, we are able to check that the generation branch is constantly optimized, reducing the amount of complications encountered in achieving demonstration of the functionality of this proof-of-principle TFISH scheme. To rapidly switch from one scheme to the other it is sufficient to simply remove or place back a mirror (M_{EOS}) mounted on top of a pair of magnetic plates which guarantees high repeatability thanks to a "ball and v-groove" design.

M_{EOS} is positioned right after the lens collimating the probe beam at the output of the DX and when in place it directs the beam towards the EOS ellipsometer, as shown in fig. 3.5(a). As discussed in subsection 2.6.2, the first element encountered is an achromatic quarter-wave plate, oriented with the retarder fast axis at 45° with respect to the probe polarization to change the polarization state from linear to circular. The two crossed polarization components are spatially separated by 20° after passing through a calcite Wollaston prism. This wide separation angle is required to align the splitted beams onto the indium gallium arsenide (InGaAs) diodes pair of the PDB450C adjustable gain balanced amplified photodetector. This Thorlabs' detector presents a wavelength range between 800 and 1700 nm, a common

mode rejection ratio of more than 25 dB and five transimpedance gain (bandwidth) settings, ranging between 10^3 V/A (150 MHz) and 10^7 V/A (100 kHz). Since the diodes' active area is of 0.3 x 0.3 mm^2 and they are only 20 mm away from each other, two half-inch lenses with 20 mm focal length channel the entire power of the beam onto the photodiodes.

When M_{EOS} is removed, the THz transient can be detected via TFISH generation. If the medium responsible for the four-wave mixing (FWM) is a non-centrosymmetric material, then the local oscillator (LO) field, required to achieve coherent detection of THz fields (subsection 2.6.3), can be generated within the same crystal and it is intrinsically copropagating with the TFISH. In other words, the TFISH and LO are created within the same medium, which is possible because of the symmetry of the considered material (see section 2.4). On the other hand, when the DX is a centrosymmetric medium, it is not possible to produce the SH bias internally, which means that we need to employ an additional nonlinear material, this time with non-zero $\chi^{(2)}$. Instead of placing such a crystal along the probe path, in between the focusing lens onto the DX and OAPM$_2$, we decide to take a small fraction of the pump pulses, right after BS$_1$, and generate the SH bias "externally". This way, it is easier to manipulate the intensity, the phase and the polarization of the LO field than it would be by placing a BBO along the probe arm. It also allows to reserve the entire amount of energy of the probe pulses to drive the FWM, which is a higher order nonlinear process and thus it requires higher peak intensities to be relevant. Therefore, to sum up, we need the third beam (LO) only if the DX is not able to provide itself the SH bias.

The small fraction of pump energy is reflected away by the beamsplitter BS$_2$, which is a 5 mm thick CaF$_2$ wedged plate with uncoated front surface: as a consequence of Fresnel reflection (see section 2.1), with an incidence angle of 45°, s-polarized light presents a power reflection coefficient of about 8%. In other words, 8% of the 250 nJ are redirected in the LO arm to get a sufficiently strong second-harmonic out of a beta-barium borate (BBO) crystal and therefore yield a LO field with enough power to almost saturate the photodiode (PD), even considering the losses due to all the optical elements found along the path. This way, we can exploit the full dynamic range of the PDA36A2 switchable gain photodetector from Thorlabs.

When the LO is externally generated, the probe and LO branches are recombined via a polarizing beamsplitter (PBS) cube. The advantage of using a PBS instead of a regular 50:50 beamsplitter is that it allows to obtain the signal of interest uniquely in one of the two outputs, provided that the two fields are kept on crossed polarization states, avoiding to lose half of the signal. The LO field is obtained via second-harmonic generation in a 300μm-thick BBO crystal, with cut angle chosen to optimize type-I phase matching at 1.55 μm. To boost

even more the conversion efficiency and obtain a strong LO beam, the fundamental beam is tightly focused, down to roughly 20 μm as beam waist diameter, with a lens that has 40 mm focal length. The achieved peak intensity in the focal point does not pose any issue in terms of damage or saturation because the power of the fundamental pulses is less than 10 mW. Keeping in mind that the fundamental beam is s-polarized, the SH resulting from type-I phase matching is p-polarized, which implies that the LO is transmitted through the PBS. On the other hand, the orientation of the DX must be set to have TFISH generated along the s-polarization so that it gets reflected by the PBS and copropagates with the LO, as pictured in fig. 3.5(b).

The length of the LO arm can be finely adjusted to match the length of the probe path, yielding perfect temporal overlap of the pulses, by varying the relative position of the retroreflecting prism mirror mounted on top of a manual linear translation stage. However, the synchronization of the TFISH and LO is not enough to guarantee a successful THz detection: the signal resulting from the linear mixing, expressed in eq. 2.73, depends on the relative phase difference $\Delta\phi$ between the fundamental probe field and the SH bias. A possible way to adjust $\Delta\phi$ consists in varying the difference in path length Δz between the two arms by a distance as small as a fraction of the wavelength λ_f of the fundamental beam (since a $\Delta z = \lambda_f/2$ induces $\Delta\phi = \pi$). For this reason, one of the mirror along the LO arm is glued on top of a high-precision piezo-driven platform (S-310.10 from Physik Instrumente): this piezoelectric transducer has a resolution of 100 nm and a travel range of 6 μm.

Coherent detection of the THz field is achieved via linear interference of the SH bias with the TFISH field. Since the two fields are cross-polarized, after the PBS we place an adjustable analyzer roughly at 45°: its goal is to project the polarization of the two pulses along the same direction and to precisely control their relative amplitudes. The analyzer consists in a Glan-Thompson calcite prism [69] with 40° field of view, put inside a rotation mount for the fine-tuning of the polarization axis angle. Afterwards, any unwanted spectral components is suppressed by a band-pass filter (BPF) with central wavelength of 775 nm and passband of 50 nm. Then, the interference signal is detected with a silicon-based switchable gain photodetector (PDA36A2), who operates in a wavelength range between 350 and 1100 nm, with eight gain (bandwidth) configurations: from $1.51 \cdot 10^3$ V/A (12 MHz) up to $4.75 \cdot 10^6$ V/A (3 kHz).

The output of the photodetector (or of the balanced photodetector when using the EOS detection scheme) is connected to a lock-in amplifier, together with the reference signal from the chopper modulator, to make sure that the field-dependent TFISH component is predominantly detected (see subsection 2.6.3) and improve the SNR, as already mentioned.
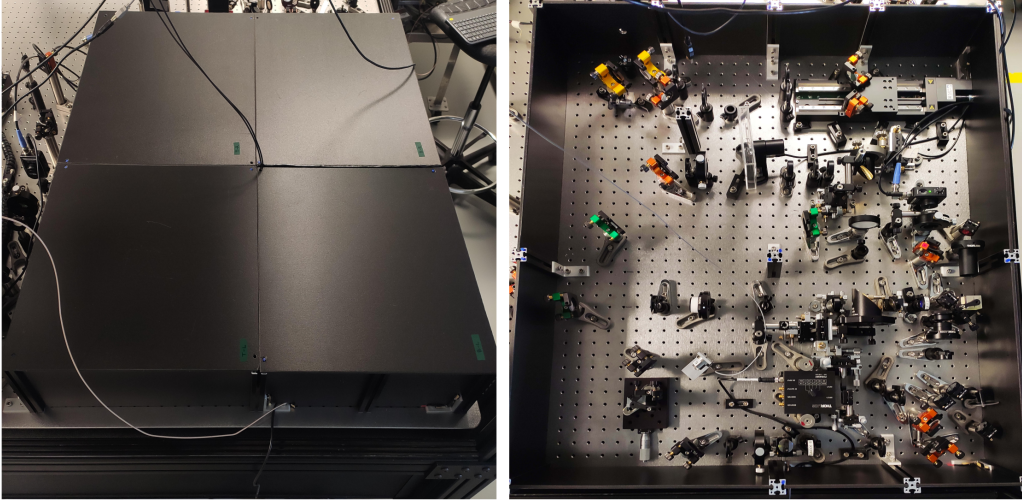
Figure 3.6 Top view of the custom modular enclosure structure with (left) and without (right) the top PVC panels.

In this work we use the Zurich Instruments' MFLI 500 kHz digital lock-in amplifier. The demodulated signal output is acquired through a homemade Python graphical user interface (GUI), which controls at the same time the automated linear translation stage and the lock-in to properly store the pump-probe measurement data.

Finally, the whole THz generation-detection setup is surrounded by a tailored modular optical enclosure, made of black opaque PVC panels and aluminum rails. The main reason behind this enclosed structure is to isolate as much as possible the setup from perturbations and noise sources coming from the lab environment, which easily affect the stability of the interference between the TFISH and the external LO, as discussed in section 3.4. At the same time, the enclosure prevents the accumulation of dust on the optical elements and it protects the system from accidental impacts. The modularity of the enclosure allows to easily remove and place back each panel, as depicted in fig. 3.6, granting a quick access to each part of the setup at any time.

3.3 Determination of the Zero Time Delay

Once the optical elements constituting the experimental setup, represented in fig. 3.1, are put in place, one of the first challenges to overcome in order to ensure a successful pump-probe experiment is the finding of the so-called zero delay position of the delay stage. The zero delay is the position for which the optical path of the pump beam matches exactly the probe's one, resulting in the temporal overlap of the pump and probe pulses. Of course,

one could rightfully suggest to carefully measure the geometrical length of each arm with a measuring tape. However, we have to remember that the pulse width is of few tens of femtoseconds, implying that the difference in path length has to be less than 30 μm to yield the temporal overlap. Needless to say, this level of precision is practically unattainable with a measuring tape, especially considering that the length of each arm is more than a meter long and that the beam bounces on multiple mirrors. Nevertheless, this is helpful to get a first rough estimate of the position of the zero delay. In principle, any interferometric technique, linear or nonlinear, allows to find the zero time delay in a precise and unique fashion. In our case we decide to exploit a nonlinear approach because on top of the zero delay determination it also grants the possibility to optimize the quality of the spatial overlap of the two beams at the detection spot (DX). Indeed, the strongest nonlinear signal is achieved only when the beams are focused at the same focal plane and their cross sectional areas are perfectly superposed.

In particular, we use a $\chi^{(2)}$ medium, e.g. a BBO crystal, as DX and since the two beams are recombined in a collinear geometry, the upconverted signal detected with a photodetector gives rise to the well-known second-order interferometric autocorrelation (IAC) trace. An example of such a measured trace is reported in fig. 3.7, recognizable by the presence of a DC offset and of two oscillatory terms, one at double the frequency of the other, which is a typical feature of such experiments [70]. Additionally, this approach yields an estimate of the actual duration of the pulses (see section 2.3) at the level of the detection spot, after
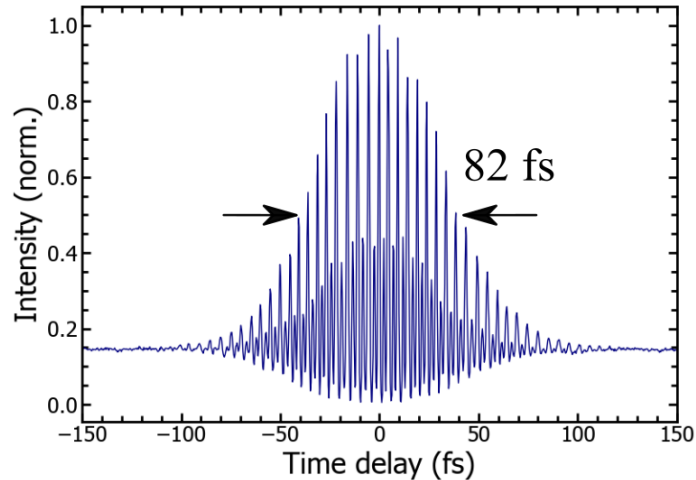

Figure 3.7 Measured second-order interferometric autocorrelation trace, showing the intensity of the up-converted signal as a function of the relative delay between the two pulses.

propagating through all the dispersive elements encountered along the setup. Assuming a Gaussian envelope shape, the FWHM of the IAC trace is of about 82 fs, which in turn means a FWHM of the pulse equal to $82/\sqrt{2} = 58$ fs. This is only 1 fs longer than the duration (57 fs) measured with FROG, proving that the pulse width before the setup and at the DX is basically unchanged due to the very low dispersion introduced by the chosen optical elements.

3.4 Effect of the Enclosure System on the Interference Stability

Optical interference has always been known to be easily affected by environmental conditions surrounding the optical setup [4], in particular when the two beams of the interferometer encounter multiple elements (mirrors, lenses, substrates, etc.) and propagate for a long distance before being recombined. This is due to the fact that the cross-correlation term resulting from the interferometry depends on the relative phase term ($\Delta\phi$ in eq. 2.73) of the optical fields, whose fluctuations can be even more detrimental than amplitude variations for this category of experiments.

When the LO is generated within the same medium as the TFISH, we expect the fluctuations of the relative phase term to be irrelevant because the two beams share the same exact optical path, hence the phase variations of the two fields are likely correlated. On the other hand, when the LO is generated in a separate arm everything described above risks to seriously compromise the detection of THz transients. For this reason, special care must be taken in order to minimize as much as possible the random phase fluctuations induced, for instance, by mechanical vibrations, air turbulences, dust particles crossing the beam line, etc. This is where the optical enclosure showed in fig. 3.6 comes into play and this section aims to show the effect on the phase fluctuations of the presence or absence of the box on top of the experimental setup.

At this stage, the LO is generated in the external LO arm (refer to fig. 3.1) while the TFISH field is replaced by the second-harmonic generated in another BBO crystal (placed at the DX spot). This way, the interference is really strong and easy to detect with a spectrometer. The signal resulting from the linear mixing is spectrally resolved and its temporal evolution is recorded by acquiring the spectrum every 5 seconds over a total interval of 180 seconds, which is generally the time required to scan and acquire the entire THz transient in this work. Panels (a) and (b) of fig. 3.8 present the evolution in time of the spectra (along the y-axis) acquired without and with the enclosure in place, respectively. The presence of spectral fringes is due to the fact that we willingly kept a given delay between the two pulses in order to easily perceive phase fluctuations, which manifest as a variation of the fringe spectral position. Without going through the entire calculations [34], the power spectrum
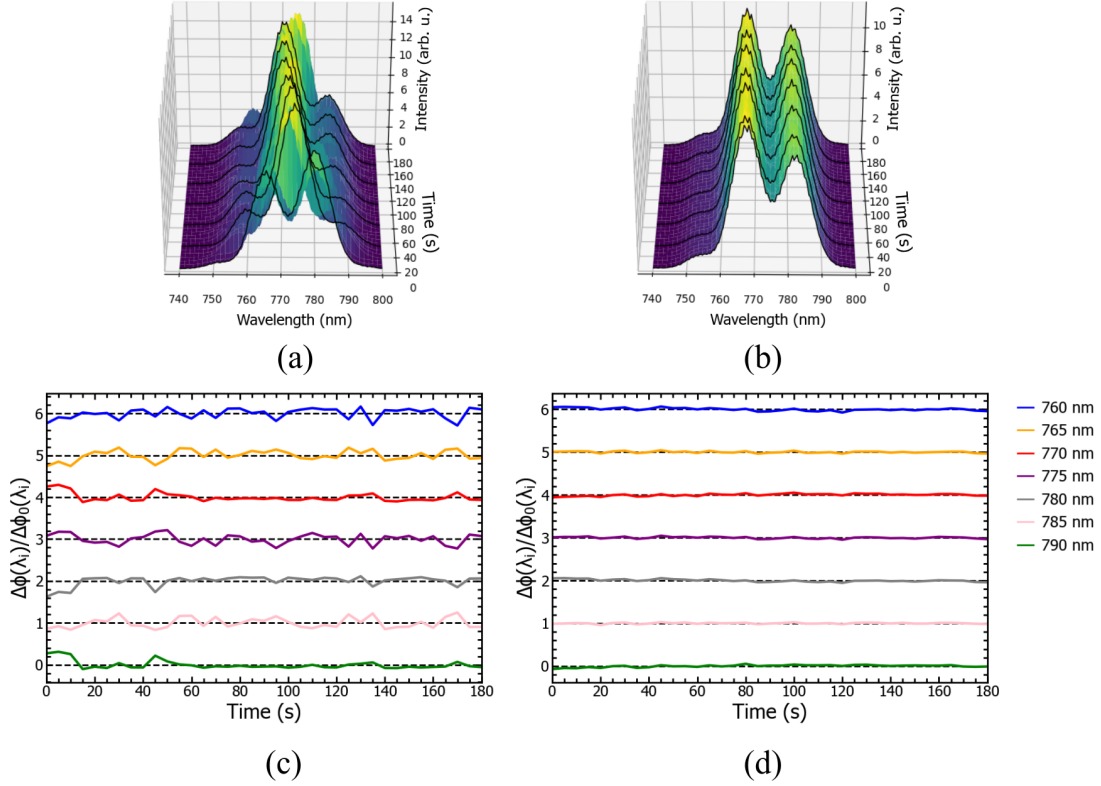
Figure 3.8 Effect of the optical enclosure on the stability of the interference. (a) Temporal evolution of the power spectrum recorded while setup is exposed to the lab environment. (b) Same as panel (a), but this time it is recorded with the modular box put in place. Panels (c) and (d) present the evolution of the relative phase term $\Delta\phi$, normalized to an arbitrary value $\Delta\phi_0$ (depicted with dashed lines), for a set of seven wavelengths λ_i, listed on the right, in absence and presence of the enclosure, respectively.

$|A_{tot}(\lambda)|^2$ of the two combined pulses, delayed by τ with respect to each other, is given by the following equation

$$|A_{tot}(\lambda)|^2 = |A_1(\lambda)|^2 + |A_2(\lambda)|^2 + 2\,|A_1(\lambda)|\,|A_2(\lambda)|\cos\left[\frac{2\pi c}{\lambda}\tau + \Delta\phi(\lambda)\right] \qquad (3.1)$$

where λ is the wavelength, $A_{1,2} = |A_{1,2}|\,e^{i\phi_{1,2}(\lambda)}$ are the spectra of the two fields, written as the product of an amplitude and a phase term, and $\Delta\phi(\lambda)$ is the relative phase term. When the delay τ between the pulses is around 150 fs, the product $\omega\tau$ is such that a modulation appears on top of the spectrum. Ideally, for a given configuration of the setup, $\Delta\phi$ should be constant, but the presence of noise sources and perturbations makes it dependent on time.

Hence, the term $\Delta\phi(\lambda)$ can be expressed as

$$\Delta\phi(\lambda, t) = k\Delta x + \phi_{noise}(t) \tag{3.2}$$

where we distinguish between a constant phase contribution, due to the path length difference Δx times the wave vector k, and a time-dependent term, $\phi_{noise}(t)$.

Looking at the two surface plots of fig. 3.8, it is evident from a qualitative point of view that the enclosure considerably helps in reducing the phase instabilities: when the setup is exposed to the environment (panel (a)), the fringes move constantly over the spectrum within the 180 s, while when the box is in place (panel (b)) the fringes are still for the entirety of the acquisition. To get a more quantitative estimate, we analyze the time evolution of the spectral intensity $|A_{tot}(\lambda_i, t)|^2$, each normalized to its mean value, for a set of seven wavelengths λ_i, from 760 to 790 nm with interval of 5 nm, which is the region where the spectrum is more intense. Now, since we are interested in the term $\phi_{noise}(t)$, we translate the fluctuations in intensity with respect to the mean into variations of the phase $\Delta\phi(\lambda_i)$ with respect to an arbitrary value $\Delta\phi_0(\lambda_i)$, corresponding to the phase needed to get the mean of $|A_{tot}(\lambda_i, t)|^2$. Fig. 3.8(c) and (d) represent those ratios for each wavelength (they are translated along the y-axis for the sake of clarity) in the case of absence and presence of the enclosure, respectively, while in table 3.1 we report the normalized standard deviation of $\Delta\phi(\lambda_i)$ for each wavelength in the two cases. The statistic shows that when the setup is isolated by the enclosure, the amplitude of the phase fluctuations are reduced by more than a factor of 4, highlighting once more the importance of building an enclosure system for our experiment.

Table 3.1 Normalized standard deviation σ of the phase fluctuations for multiple wavelength, recorded when the setup is exposed to the lab environment and when it is fully covered by the enclosure.

	λ_i (nm)	760	765	770	775	780	785	790
$\dfrac{\sigma[\Delta\phi(\lambda_i)]}{\Delta\phi_0(\lambda_i)}$	w/o box	0.123	0.121	0.100	0.122	0.118	0.123	0.101
	w/ box	0.033	0.020	0.026	0.021	0.028	0.015	0.026

CHAPTER 4   DEMONSTRATION OF COHERENT DETECTION OF TERAHERTZ TRANSIENTS

After careful and thorough alignment of the setup described in chapter 3, we are able to coherently measure the THz transients via homodyne detection of the terahertz-field-induced second-harmonic signal (TFISH) produced in solid-state media. This chapter is divided in two parts. In the first section we present the characterization of the THz source via electro-optic sampling, with analysis of the temporal and spectral dependence. Then, in the second section, we use these results as benchmark for the measurement obtained via the main detection scheme of this work, i.e. the TFISH-based system, and we show some of the most relevant features of such process, including the quadratic dependence of the TFISH signal on the fundamental probe intensity and the ability to measure both quadratures of the field.

4.1   Terahertz Field-Resolved Detection via Electro-Optic Sampling

Fig. 4.1 presents the temporal and spectral representation of a THz transient generated via optical rectification and detected via electro-optic sampling, exploiting as nonlinear medium for both processes a 500 μm thick ZnTe crystal with <110> crystalline orientation.

The choice of ZnTe as nonlinear crystal has the goal to yield a temporal trace with a high signal-to-noise ratio (SNR), since this kind of medium presents one of the highest figure of merits for the nonlinear processes of OR and EOS [2, 3]. On top of that, the substantial thickness (500 μm) contributes in generating and detecting a stronger THz field because it improves the global nonlinear efficiency. The measured field SNR, defined as the ratio between the peak-to-peak value and twice the standard deviation of the signal demodulated by the lock-in amplifier in the absence of the THz field, is roughly 100 with chopper modulation at 2.25 kHz and with integration time for each data point of 500 ms.

However, increase in crystal thickness comes at the price of reducing the phase matching bandwidth, constraining the THz spectrum to low frequencies. This is confirmed by the spectrum shown in panel (b) of fig. 4.1, which presents strong frequency components filling the region from 0.5 to 2.5 THz, with some weak components extending up to 3.5 THz. Interestingly, the spectrum is not flat across this range, but shows a significant drop in amplitude around 1.5 THz. In order to understand the physical causes behind this "dip", we compare the measured spectrum with the expected one, computed considering the phase matching function of the nonlinear process (subsection 2.4.3) in the ZnTe substrate described
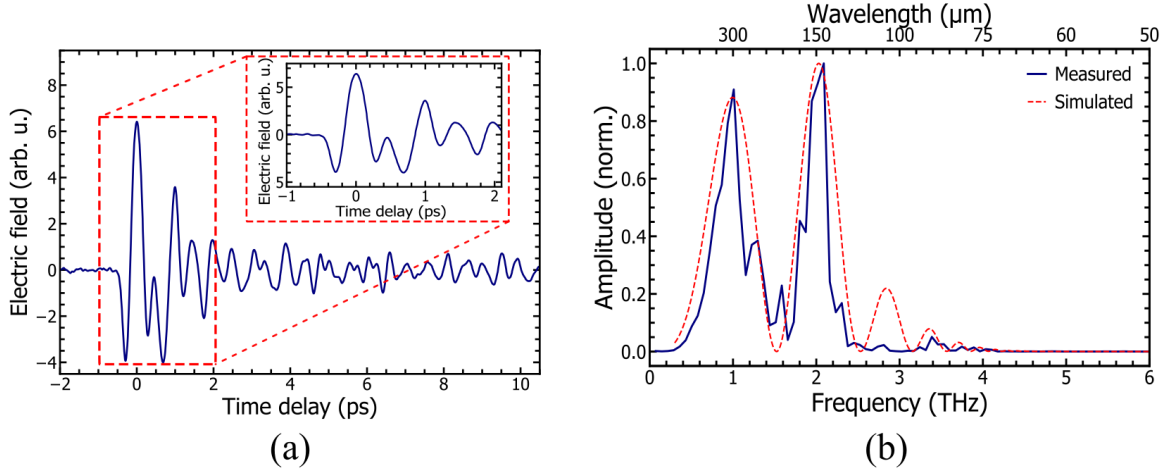
Figure 4.1 THz coherent detection yielded with 500 μm thick ZnTe as both the generation and detection crystal. The parameters of this pump-probe acquisition are the following: minimum temporal increment 10 fs, 500 ms integration time for each data point, chopper modulation at 2.25 kHz. (a) Time-resolved THz field transient, with emphasis on the main field oscillation (inset). (b) Corresponding measured (blue line) and computed (red dashed line) power spectrum, taking into account the phase matching, the THz collection fraction and the MTI's THz-LPF transmission.

above (500 μm thickness), the collection fraction of the generated THz beam (section 2.7) and the transmission of MTI's filter, which is the THz-LPF employed in the measurement (fig. 3.4(c)). From a qualitative standpoint, the experimental result matches quite well the behavior of the simulated one, especially because both of them present the significant drop around 1.5 THz. Since the filter's transmission and the THz collection function are rather flat functions below 2 THz, we can suppose that the "dip" observed in the measured spectrum is a consequence of the phase mismatch of the nonlinear process taking place in the 500 μm thick ZnTe. Indeed, while the velocity matching is satisfied in ZnTe for low THz frequencies for pumping at 800 nm [3], when the fundamental wavelength is at 1550 nm the pump and THz pulse propagate at different velocities.

This hypothesis seems to be further confirmed by the apparent distortion of the THz temporal waveform, because the mismatch in the velocities causes a destructive interference between the induced nonlinear contributions [3, 71]. As highlighted in the inset of fig. 4.1(a), around a delay of 400 fs there is a small hump that gives rise to two consecutive dips, suggesting that the detected THz pulse presents a multicycle structure. To help proving this latter sentence, in fig. 4.2 we reproduce the same trace $E(t)$ measured via EOS (blue line), together with the other quadrature $Q(t) \equiv H\left(E(t)\right)$ (red line), computed via Hilbert transform of the measured
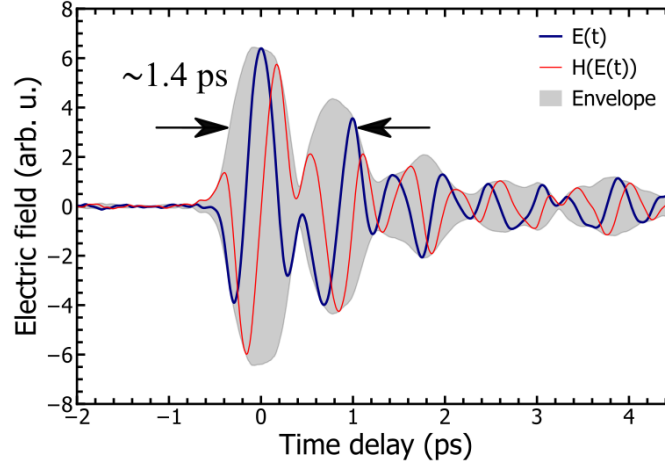
Figure 4.2 Temporal representation of both quadratures: the blue line $E(t)$ is the trace measured via EOS, the red one is the Hilbert transform $H\left(E(t)\right)$ computed from the measured transient $E(t)$. The gray filled region corresponds to the envelope of the measured field.

transient, and the corresponding envelope (gray filled region). From a mathematical point of view, the Hilbert transform is easily obtained by moving to the spectral domain via Fourier transform, applying a $\pm\pi/2$ phase shift to each frequency component (with the sign of this shift depending on the sign of the considered frequency) and finally moving back to the time domain via inverse Fourier transform [72]. Once the quadratures are both known, it is straightforward to compute the corresponding envelope as $\sqrt{E^2(t) + Q^2(t)}$ [73]. Focusing on the envelope, which is characterized by a FWHM of roughly 1.4 ps, we notice that it includes two crests with amplitude larger than half the peak value, and the cycles are indeed separated by the hump around 400 fs.

Another feature that we observe in the temporal trace of fig. 4.1 is the long oscillatory tail after the trailing edge, i.e. for positive delays. This behavior is observed quite often in THz time domain measurements, especially when the spectral amplitude is concentrated at low THz frequencies [9]. It has been demonstrated [9, 28, 74, 75] that in presence of water vapor, the detected THz transient is followed by long-lasting oscillations, while when the system is purged with dry air such tail is strongly reduced. These oscillations are therefore a consequence of the combined action of the dispersion and absorption of the multiple narrow water vapor lines, some of which fall exactly in this frequency range [9, 74].

The current implementation of the setup does not allow to control the humidity level around the system, hence a direct measurement of the THz field with small and large concentrations of water vapor is not possible, which could have directly tested the hypothesis. Nevertheless,

we believe that the oscillations are a consequence of the free induction decay of coherently-excited resonances in water because some of them correspond exactly to the structures on top of the spectrum of fig. 4.1(b): for instance, the deep narrow features at 1.16, 1.41, 1.67 THz are all aligned with strong water vapor absorption lines observed in the work of Xin *et al.* [74].

At this stage we recognize that we are limited in terms of spectral resolution in order to potentially distinguish those absorption lines, and to solve this issue we can acquire pump-probe scans for larger time delays, as reported in fig. 4.3(a). However, the corresponding spectrum (panel (b)) now presents a comb-like structure on top of the previous THz spectrum. The accurate periodicity of these spectral oscillations brings us to consider them as etalon fringes due to the fact that the DX behaves as a Fabry-Pérot cavity. Indeed, when the THz pulse propagates through the crystal, it undergoes Fresnel reflections at each interface due to the difference in refractive index (refer to section 2.1). Hence, at the output of the DX, the main THz pulse is followed by another less intense pulse, that we define as "echo", with a relative delay corresponding to the round-trip time T_{FP} inside the crystal. This situation is summarized in the inset of fig. 4.3(a). In the case of a 500 μm thick ZnTe (with refractive index around 1-2 THz taken from [51]), the echo arrives roughly after 11 ps, matching the time-delay of the feature highlighted in the temporal trace. Therefore, the expected period of the spectral fringes, inversely proportional to T_{FP}, is of about 0.09 THz, which matches
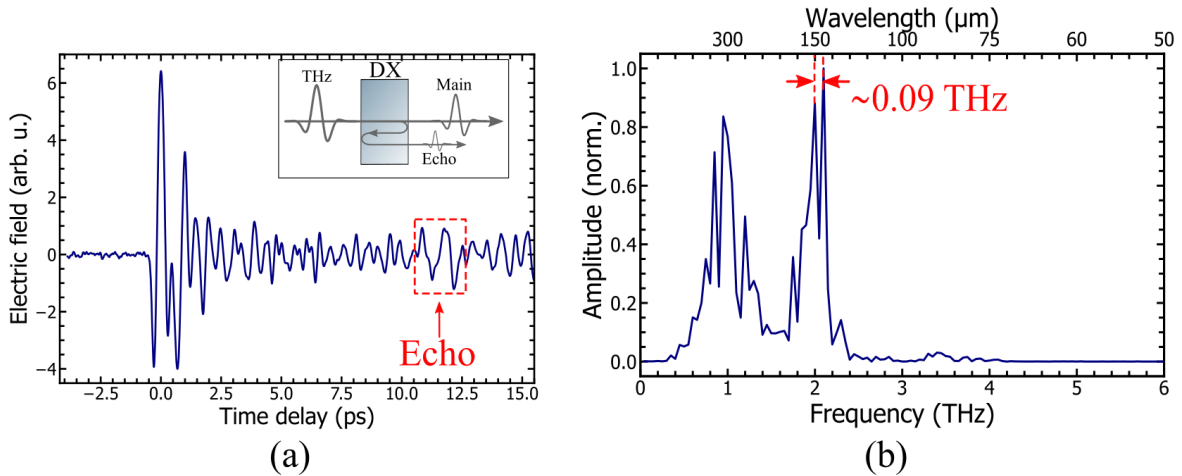

Figure 4.3 (a) Presence of an echo in the time-resolved EOS signal around a delay of 11 ps, consistent with a round trip inside a 500 μm thick ZnTe crystal. The inset schematizes the Fabry-Pérot effect that the THz pulse undergoes when propagating through DX. (b) Power spectrum modulated by fast oscillations, with period of 0.09 THz.

the comb-like structure's period of the measured THz spectrum.

Therefore, the strong spectral modulation induced by the Fabry-Pérot effect partially hides the water vapor absorption lines, complicating our analysis. In principle, there are some strategies to avoid this issue (e.g. adding an index-matched substrate to move the echo at much longer time delays [76]), but since the full resolution of all the absorption lines is not the focal point of this work, we decide to not go further in this analysis.

4.2 Terahertz Field-Resolved Detection via TFISH

Given the range of frequencies generated and detected via EOS, mainly founded between 0.5 and 2.5 THz, we decide to use a non-centrosymmetric crystal to achieve a first proof-of-principle detection of THz fields via terahertz-field-induced second-harmonic (TFISH) mixing with a second-harmonic bias (LO). This way, we can take advantage of the birefringence of properly chosen crystals to get a decent phase matching for the FWM process of the fundamental wavelength of 1550 nm and the aforementioned range of THz frequencies. In turn, a decent phase matching means that the nonlinear phenomenon is efficient over a longer thickness, resulting into a stronger and easier to be detected signal. As shown in appendix A, a silicon carbide (4H-SiC) substrate, with customized cut such that the <0001> axis (optical axis) is oriented at 90° with respect to the <1120> axis, grants a coherence length for one of the FWM processes larger than 500 μm for THz frequencies up to 2 THz.

In fig. 4.4 we report the temporal and spectral dependences of a THz transient generated via optical rectification in a 500 μm thick ZnTe crystal (same as for the EOS case) and detected via homodyne detection of the TFISH, with both the FWM signal and the SH bias generated inside a 500 μm thick 4H-SiC sample, with the orientation detailed above. This is possible because the DX is non-centrosymmetric, hence second-order nonlinearities are admitted. Unless differently indicated, the following measurements are all executed using the same aforementioned GX and DX. The SNR of the trace measured with the same chopper and lock-in settings as described above, is roughly 25, which is a factor of 4 lower with respect to the one characterizing the EOS trace, but it still allows to clearly measure and identify the THz transient in the pump-probe scan. The lower SNR can be caused by multiple aspects, among which the higher order of the nonlinear process ($\chi^{(3)}$-based instead of $\chi^{(2)}$-based) exploited for the THz detection leads to a lower peak-to-peak of the upconverted signal. In parallel, the level of noise is higher since in the current configuration the signal detection is not balanced, which means that the fluctuations of the laser intensity are not canceled out as it happens in the EOS detection.
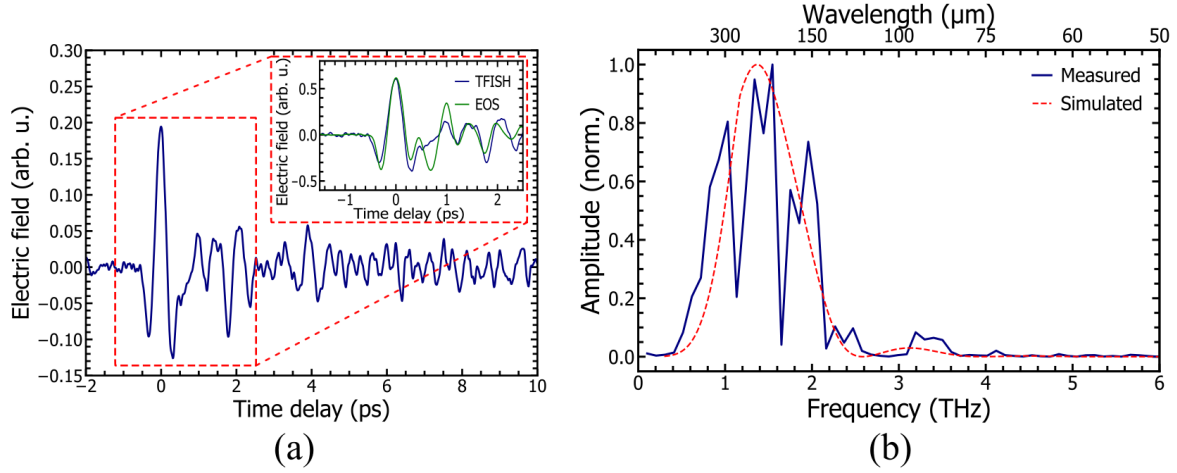
Figure 4.4 THz coherent detection yielded with 500 μm thick ZnTe and 4H-SiC as GX and DX, respectively. The parameters of this pump-probe acquisition are the following: minimum temporal increment 10 fs, 500 ms integration time for each data point, chopper modulation at 2.25 kHz. (a) Time-resolved THz field transient, with emphasis on the main field oscillations (inset): the TFISH trace (blue line) is compared with the EOS one (green line), with both traces normalized to the respective peak-to-peak value to facilitate the comparison. (b) Power spectrum (blue trace) of the TFISH-based THz measurement compared to the expected simulated spectral dependence (red dashed curve).

The main fraction of the power spectrum is still contained in the region 0.5-2.5 THz, with some components around 3.5 THz. However, one of the first thing that catches our eyes when comparing the TFISH-detected THz spectrum with respect to the one measured with EOS (see fig. 4.1(b)) is the absence of the wide drop of spectral amplitude around 1.5 THz, which is now replaced by strong narrow dips around 1.16 and 1.67 THz. As done in the previous section, we decide to compute a response function that takes into consideration the phase matching of the TFISH process in the currently employed 4H-SiC substrate, the transmission of the MTI's filter (same as for EOS, see fig. 3.4(c)) and the THz collection fraction. Conversely to EOS, the simulated spectral dependence, presented as the red dashed line in fig. 4.4(b), appears uniform across the range 0.5-2.5 THz. This does not surprise us because the orientation of the 4H-SiC cut is chosen exactly to guarantee a coherence length for the DFG-FWM (see subsection 2.6.3) larger than 500 μm for this entire range of THz frequencies. In this model we take into account only the DFG process because it is expected to be dominant over SFG due to the better phase matching and preliminary measurements, reported in section 5.2, able to isolate the contribution of each FWM process prove that the DFG gives indeed a much stronger TFISH signal. Therefore, from a qualitative point of view,

we believe that the absence of the wide absorption dip can be explained with better phase matching conditions of the exploited nonlinear process, which we remind to be associated to a third-order nonlinearity. Additionally, to some extent, the same argument can be used to justify the fact that the acquired temporal trace does not show the same multicyclic waveform shape as observed in EOS measurements. This is emphasized in the inset of panel (a) of fig. 4.1, where we observe that the blue line (TFISH) reproduces only the first main oscillatory cycle of the green trace (EOS), but not the second.

Nevertheless, this first analysis is not able to explain the appearance of the narrow dips in the measured spectrum of fig. 4.4, nor the features that emerge in the temporal trace on a consistent basis, clearly observable around delays of 2 and 4 ps. The Fabry-Pérot effect does not seem to be the reason behind such effects because the short delay at which the first feature is located does not match the expected round trip time of the THz pulse inside the 500 μm thick 4H-SiC substrate, which is still around 11 ps because the refractive index in the THz range is similar to the ZnTe's one [51, 77]. Now, one could hypothesize the presence of unforeseen imperfections in the substrate that could induce Fresnel reflections and create an effective thinner cavity. However, the measured spectrum does not show the periodic modulation typically associated to etalon fringes, hence we do not believe this to be the cause.

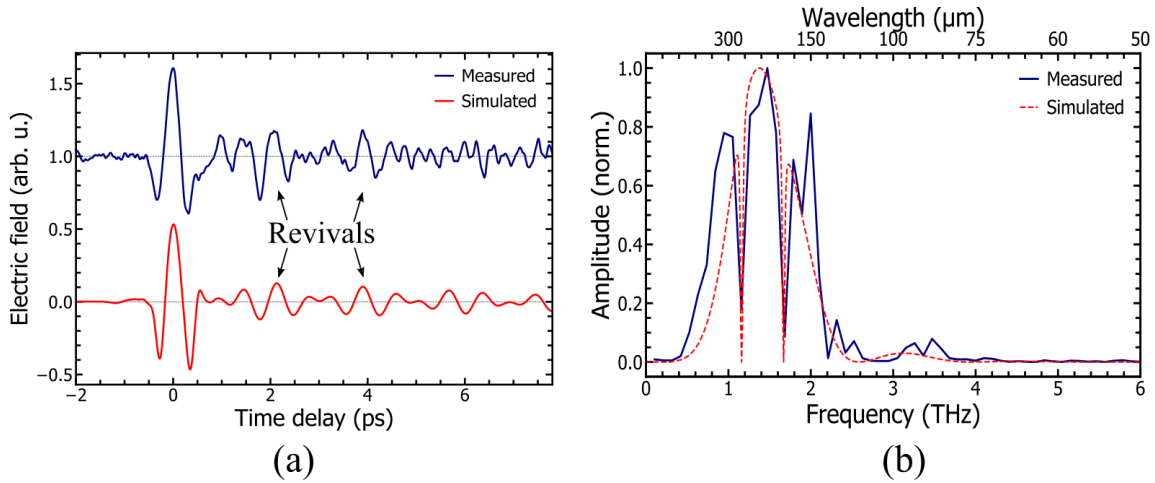Interestingly, the main narrow spectral drops occur around 1.16 and 1.67 THz, which are

Figure 4.5 (a) Comparison between TFISH measured trace (blue) and simulated temporal dependence (red) considering the presence of water vapor resonances, obtained via Fourier transform of the dashed spectrum in panel (b), which presents also the spectral amplitude of the corresponding measured trace (blue).

among some of the strongest water vapor resonances [74]. To understand the potential overall effect of those absorption lines on the temporal dependence of the THz transient, we develop a simplified model consisting in computing the Fourier transform of the spectrum obtained as the product of the previous response function (reported in fig. 4.4(b)) and of the frequency-dependent susceptibility $\chi(\omega)$ of the water vapor. The latter function is modeled following the approach suggested by Rasekh *et al.* [75], but considering standard state conditions, a propagation of the THz in air of roughly 50 cm and taking into account only the resonances discussed above, i.e. at 1.16 and 1.67 THz. Some of the useful parameters are taken from HITRAN database [78]. The resulting spectral amplitude is depicted with a red dashed line in panel (b) of fig. 4.5, while the comparison between the simulated and measured temporal trace is reported in panel (a). We notice that the presence of water vapor not only causes the long oscillatory tail, typical of the free induction decay of the resonances, but it also gives rise to a beating pattern on top of the tail as a consequence of the interference between the absorption lines. The periodic shift between constructive and destructive interference creates features that we define as "revivals", whose amplitude gradually decreases at longer delays. Even though our model does not entail all the vapor resonances observed in the range 0.5-2.5 THz, it already reproduces rather well the period at which the revivals appear in the measured trace, i.e. roughly every 2 ps. The amplitude of the revivals at delays larger than 6 ps is too weak to be clearly distinguishable with the limited SNR of the detection.

4.2.1 Dependence of the Peak TFISH on the Fundamental Probe Intensity

In order to further verify that the detection of the THz field is indeed achieved via the generation of the TFISH, we study the dependence of the measured time-resolved cross-correlation signal $S_{2\omega}$ on the fundamental probe intensity I_ω. As discussed in subsection 2.6.3, according to FWM theory [28], $S_{2\omega}$ is proportional to the product of the probe intensity and the SH bias field, which in turn is proportional to I_ω, hence we expect a quadratic dependence between $S_{2\omega}$ and I_ω [53]

$$S_{2\omega}(\tau) \propto \cos(\Delta\phi) \int I_\omega^2(t) E_\Omega(t-\tau)dt \tag{4.1}$$

From an experimental point of view, we record the peak values of the signal demodulated by the lock-in, corresponding to the zero pump-probe delay, for multiple probe intensities, whose value is measured with a powermeter and converted from power to peak intensity knowing the duration (58 fs) of the pulse and the beam waist (25 μm) at the DX. The various data points and the associated quadratic fit are reported in fig. 4.6. The excellent fit, with coefficient of determination R^2 of 0.997, thus constitutes an additional proof that
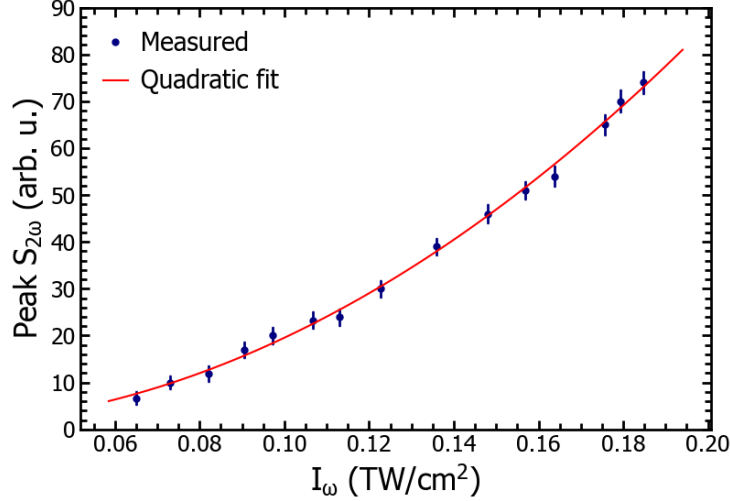
Figure 4.6 Dependence of the peak values of the TFISH time-resolved cross-correlation $S_{2\omega}$ on the fundamental probe intensity I_ω. Each point corresponds to the peak value of $S_{2\omega}$ averaged over a minute of acquisition, while the associated error bar represents the standard deviation of such acquisition.

the observed phenomenon is the four-wave mixing of the fundamental probe and THz pulses.

4.2.2 Linear Mixing with Internal or External Local Oscillator

As briefly discussed above, an intrinsic feature of the homodyne detection of TFISH in non-centrosymmetric materials is that the LO field can be generated within the same crystal that produces the FWM process [53], without the need of the external LO arm presented in fig. 3.1. Nevertheless, with such strategy it is not possible to fully control at the same time the intensity, the polarization and the phase of the LO field, without compromising the efficiency of the TFISH process. This is where the external LO arm comes into play, because it implies an easy and independent manipulation of all the detailed properties of the LO field, maintaining the highest efficiency of the FWM signal. An example of application where the full control of the SH bias is of fundamental importance is the sampling of quantum THz electric fields because such control grants access to both quadratures (see subsection 4.2.3), needed to sample the quantum fields beyond the bare vacuum [29–31].

For these reasons, we demonstrate that the coherent detection of the THz transient generated in our setup is possible following both approaches, as proved in fig. 4.7. The experimental conditions are identical (nonlinear media, modulation frequency, lock-in parameters), with the exception of the field considered as SH bias. The THz filed is clearly identifiable in each
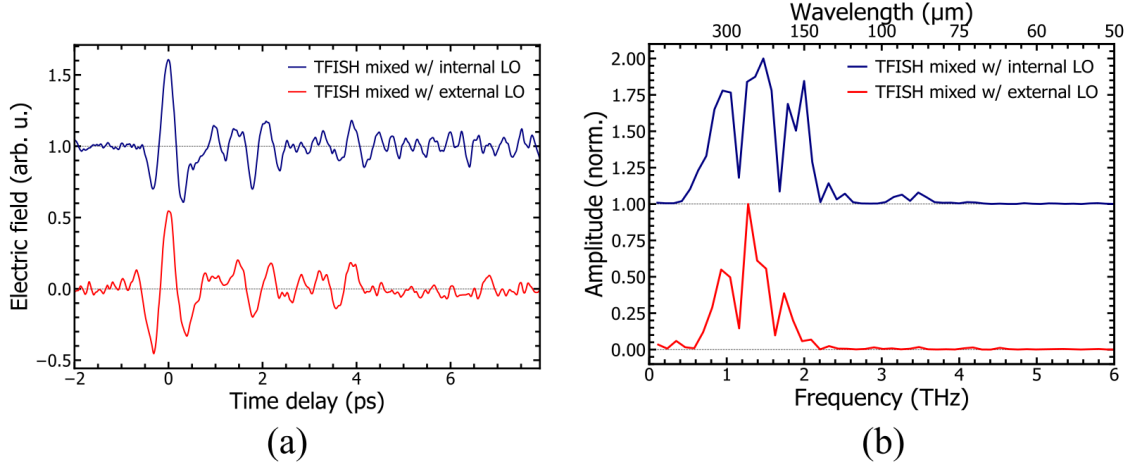
Figure 4.7 Comparison between TFISH traces measured via mixing with LO generated "internally" (blue) and "externally" (red), both normalized to the respective peak-to-peak value. (a) Time-resolved transients measured with the two strategies with (b) corresponding spectra. In both plots, the translation along the y-axis of the zero-ordinate (dashed line) for the blue trace is done for the sake of clarity.

scan, with the SNR of the red trace (external LO) slightly lower than the one of the blue trace (internal LO). The spectral bandwidth of the detected field is fairly comparable, with most part of the spectrum concentrated below 2.5 THz in both cases. Another common characteristic is the presence of strong absorption lines falling close to the water vapor resonances at 1.16 and 1.67 THz, as described in section 4.2, whose interference is likely the cause behind the appearance of revivals in the temporal traces.

Therefore, besides some minor differences in the SNR, we have shown that from a fundamental point of view both strategies lead to a successful measurement of the THz transient. However, it is important to point out that in the current version of the setup, even when the enclosure system is in place, the strategy relying on the external LO suffers from instabilities of the interference, which affects the repeatability of the measurement and a shift of the DC component of the trace over the acquisition period. With this said, we recognize that it does not constitute a major issue for the technique because it can be solved in future implementations by replacing the free space propagation with propagation into waveguides (see section 5.2).

4.2.3   Control of the Phase of the Detected Field

At this point we test the possibility to control the phase of the detected THz transient by acting on the relative phase term $\Delta\phi$ [28], which we remind to be determined by the difference between the phase of the fundamental field and of the SH bias. Due to a better stability of the interference, we employ as LO the SH radiation generated within the 4H-SiC substrate. The variation of $\Delta\phi$ is thus achieved by modifying the orientation of the 4H-SiC optical axis with respect to the fixed polarization of the probe beam, since the birefringence of this material leads to a variation in the relative delay, and in turn of the phase, between the two fields.

In particular, it is interesting to change $\Delta\phi$ by $\pi/2$ because the detected signal $Q(t)$ corresponds to the quadrature of the in-phase signal $E(t)$, measured before the phase change. As mentioned at the end of subsection 2.5.2, coupling to both quadratures is fundamental especially for quantum tomography of light in the time domain [30]. In order to verify that $Q(t)$ is indeed the quadrature, we can compare it with the Hilbert transform of $E(t)$, which is the mathematical operation that gives access to the quadrature, as discussed previously.
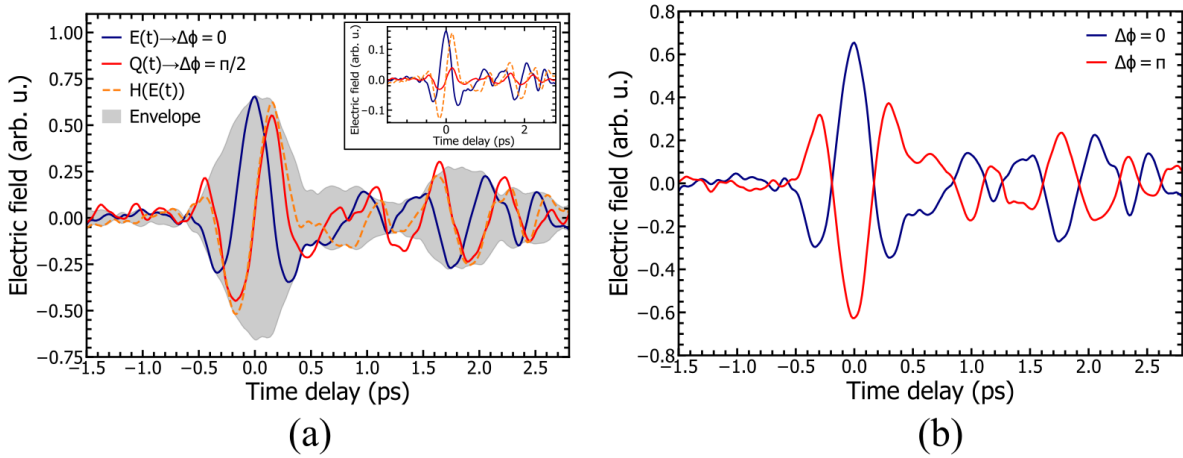

Figure 4.8 Time resolved THz field transient detected via linear mixing of the TFISH signal and the SH bias generated within the DX, applying different relative phase terms $\Delta\phi$ between the probe and the LO fields. (a) Successful measurement of the two quadratures of the field (blue and red lines), denoted respectively as $E(t)$ and $Q(t)$, by changing $\Delta\phi$ by $\pi/2$. The orange dashed line depicts the Hilbert transform of $E(t)$, indicating the expected behavior of the quadrature $Q(t)$, whereas the gray filled region represents the envelope of the pulse. The inset shows the raw amplitude of the measured signals, which are normalized to the respective peak-to-peak amplitude in the main diagram to facilitate the analysis. (b) Nearly perfect inversion of polarity of the TFISH measured trace when $\Delta\phi$ varies by π.

In panel (a) of fig. 4.8, we show that our setup is able to measure the two quadratures of a THz field, because from a qualitative point of view the measured quadrature $Q(t)$ (red trace) reproduces rather well the expected behavior, obtained via Hilbert transform of the other quadrature $E(t)$ (blue trace) and represented by the orange dashed line. In particular, the red and orange curves resemble each other in terms of the shape of the main oscillation cycle and the time delays at which the largest positive and negative peaks are located. The minor deviations from the theoretical trace in the trailing edge of the THz transient could be attributed to a slight under-rotation (or over-rotation) of $\Delta\phi$ and to the very low SNR that characterizes the red trace. Indeed, in panel (a) all the traces are normalized to the respective peak-to-peak value to facilitate the comparison, while the original traces are reported in the inset. There, it is evident how weaker is the detected transient corresponding to $Q(t)$ with respect to $E(t)$, and this is a drawback of employing as LO the SH bias generated inside the DX. In such configuration, to induce a relative phase variation we can only change the orientation of the 4H-SiC optical axis, but doing so we unavoidably affect the efficiency of the TFISH generation since the phase matching conditions of the FWM get modified as well. On the other hand, the strategy based on the external LO does not present this issue because in principle we can achieve full control of the intensity, the polarization and the phase of the LO field, without compromising the efficiency of the TFISH process.

A further confirmation that $Q(t)$ closely coincides with the theoretical quadrature comes from the fact that the red trace nicely fits in the gray filled region, which represents the envelope of the measured THz pulse. The envelope is computed in the same way explained in section 4.1, i.e. as $\sqrt{E^2(t) + H^2\left(E(t)\right)}$, using as H the computed Hilbert transform. As suggested above, due to the poor SNR and to $\Delta\phi$ being slightly different from $\pi/2$, in some points the red trace goes out of the envelope. The envelope also supports what stated in section 4.2, regarding the absence of the multicyclic waveform observed in the EOS measurements (see fig. 4.2).

Another insightful proof that the phase of the detected field can be controlled is shown in fig. 4.8(b): the evident inversion of polarity between the blue trace, corresponding to the maximum obtainable signal and associated to $\Delta\phi = 0$, and the one measured with an additional π-shift applied (red line) matches the behavior predicted by eq. 4.1. This offers a convenient strategy both to ensure the detection of the maximum obtainable signal and to calibrate the relative phase $\Delta\phi$.

CHAPTER 5   CONCLUSION

5.1   Summary

The main goal of this work was to conceive, build and characterize an optical setup capable of generating THz transients and temporally resolving them via homodyne detection of the terahertz-field-induced second-harmonic (TFISH) signal in solid-state media. The upconverted signal is obtained as a result of a third-order nonlinear process that can take place in either centrosymmetric or non-centrosymmetric materials. In order to reduce the number of challenges and unforeseen complications associated with this rather new detection technique, we decided to build in parallel the widely diffuse and easy-to-implement electro-optic sampling (EOS) setup. This way we were able to get a first characterization of the low-frequency transients generated via optical rectification (OR) and keep it as a reference for the TFISH-based detection.

The designed system was put together by precisely aligning every optical element necessary to the experiment. A first part of the fundamental beam, the pump, is directed to the generation of the THz transient via OR and successively recombined with the other part of the fundamental beam, the probe, inside the detection crystal (DX). A mirror mounted on a quick-release magnetic base gives alternate access to the regions of the setup dedicated to EOS and TFISH detection, respectively. The entire THz generation-detection system is surrounded by a modular enclosure, which proved to considerably improve the stability of the interference between the probe beam and the one generating the local oscillator field.

Employing 500 μm thick ZnTe substrates as both the GX and DX, the EOS scheme detected THz fields with SNR of 100 (500 ms integration time for each data point) and the corresponding spectrum mainly comprised between 0.5 and 2.5 THz, with some weak components up to 3.5 THz. Qualitatively, the measured spectrum matches quite well the expected behavior, obtained via numerical simulations of the system's response function, which takes into account some of the factors that are mostly affecting this spectral region. In particular, the spectral dip observed around 1.5 THz appears to be associated with the phase mismatch of the nonlinear phenomenon taking place in the 500 μm thick ZnTe. Additionally, the long oscillatory tail following the trailing edge of the THz pulse indicates that coherently-excited water vapor resonances are causes of distortion for the measured transient.

Detection of the low-frequency transients, still generated via OR in the aforementioned ZnTe substrate, was achieved via homodyne detection of the TFISH signal (SNR of 25, with 500

ms integration time for each data point) induced in a 500 μm thick substrate of 4H-SiC with customized cut. While the bandwidth of the measured power spectrum was comparable to the one obtained with EOS detection, the spectrum did not present the wide dip around 1.5 THz. Its absence can potentially be explained with the different phase matching function on the detection side, since both the medium and the exploited nonlinear process are different with respect to the EOS case. The presence of long-lasting oscillations after the trailing edge, as happened for EOS and typically observed in low-frequency THz time-resolved measurements, added to the appearance of two narrow strong drops in the spectral density, which correspond to some of the strongest tabulated water vapor resonances, convinced us that the generated THz field excites some of the vibrational modes of water molecules, met along the path in between the generation and detection spots.

In order to further prove that the detection of THz transients was indeed achieved via TFISH generation, we showed that the dependence of the peak value of the TFISH signal on the fundamental intensity is quadratic, as expected from theory, and that it is possible to control the phase of the detected field by acting on the probe and LO phase terms. In particular, when a π-shift was applied the THz field polarity was almost perfectly inverted, while a $\pi/2$ phase shift gave us access to the other quadrature of the field, confirming the possibility to measure both quadratures of the electric field. Finally, the coherent detection was demonstrated using as LO either the SH bias obtained from the $\chi^{(2)}$ process within the 4H-SiC or with the external optical bias obtained via frequency-doubling in a BBO crystal. To the best of our knowledge, this constitutes the first successful demonstration of THz detection using such approach, with an excitation source in the telecommunication window and without requiring highly-energetic pulses (in the order of 100 nJ).

5.2 Limitations and Future Research

Being a proof-of-principle demonstration of THz field-resolved detection via TFISH generation, the current performance of the setup in terms of bandwidth and sensitivity is not yet comparable with state-of-the-art THz detection systems, but it has the potential to be substantially improved.

As shown in fig. 4.5(b), the detected bandwidth with the current implementation is limited below 4 THz. Among the limiting factors, the main ones are the type and thickness of the substrates used as generation and detection crystals, the driving pulse temporal width and the transmission of the optical filter (THz-LPF) responsible of suppressing the pump leakage.

On the detection side, phase matching calculations reported in appendices A show that

a birefringent material like 4H-SiC provides an optimal phase matching, but only over a limited bandwidth, outside of which the efficiency of the desired nonlinear process drops very sharply. While this is advantageous to test the system functionality, providing a stronger and easier to identify TFISH signal, since a thicker substrate can be employed, it strongly limits the detected bandwidth within this narrow window. For this reason, once the detection system is proved to be working with a decent SNR, we can switch to thinner substrate of the same material, gaining a broader phase matching response function without requiring major changes in the setup because the optical properties of the medium are the same. Once this is achieved, an additional improvement consists in replacing the 4H-SiC with a material characterized by a low refractive index dispersion like diamond, which translates in a broadband phase matching function. Even though the coherence length is lower than the one given by 4H-SiC, this material already showed promising results when Matsubara *et al.* [56] demonstrated ultrabroadband detection, up to 100 THz, using 10 fs pulses.

In parallel, a similar approach can be applied to the generation side. The currently employed 500 μm thick ZnTe substrate provides relatively strong THz transients, but the corresponding bandwidth is limited for the same reasons detailed above. Hence, as a first step, a thinner sample of ZnTe can be used as generation source or if we aim for high THz frequencies, i.e. larger than 30 THz, we can employ more suited nonlinear materials, like thin slabs of GaSe [17]. However, it is worth to point out that to reach this spectral region, shorter pulses from the excitation source are mandatory because, even admitting ideal phase matching, there is an intrinsic superior limit set by the duration of the pump and probe pulses. Obviously, this procedure implies the availability of a laser source emitting such broadband pulses and here is where operating at the telecommunication wavelength comes to play in our favor: nowadays fiber lasers oscillating at 1.55 μm and emitting pulses with duration of few femtoseconds are readily available at reasonable prices.

No matter the material used as GX, as long as the process exploited for THz generation is optical rectification there will always be a gap in the spectrum due to the TO phonon resonances. Since one of the advantages of the TFISH-based technique in centrosymmetric media is the absence of the resonance band in the detected spectra, in order to prove such aspect we need a gap-free THz source as well. An interesting technique able to solve this issue without requiring extremely energetic pulses, conversely to THz generation in laser-induced plasma (refer to subsection 2.5.1), is the spintronic emission. This novel method for THz generation is based on the conversion of spin currents into charge currents, induced by the passage of a femtosecond optical pump through a sequence of very thin (at the nm scale) ferromagnetic and non-magnetic layers [79].

Another element that needs to be modified in the outlook of gaining a larger bandwidth signal is what we defined in chapter 3 as THz low-pass filter: its function is to block any pump leakage without affecting the THz signal. The currently used THz-LPF (provided by MTI) is characterized by a high extinction ratio in the optical range, but its transmission in the THz range is decent only below 4 THz, as reported in fig. 3.4(c). TYDEX's polyethylene filter could be a feasible candidate for the system functionality at higher frequencies in terms of THz transmission, but it is not able to strongly suppress the pump leakage, adding substantial distortion to the detected signal due to the pump-probe linear interference. Another potential solution could be to place a germanium (Ge) window after the collimating off-axis parabolic mirror, since germanium transmits radiation with wavelength above 1.6 μm. However, to ensure the highest achievable THz transmission and beam quality, particular care must be taken to keep the impurities concentration in the Ge sample as low as possible. In addition, to further increase the beam transmission, the wafer should be placed with an angle of incidence equal to the THz Brewster's angle [4], which is the angle that guarantees total transmission for the p-polarized field component.

In the perspective of switching to thinner substrates to broaden the bandwidth, it is likely that we end up reducing the strength of the upconverted nonlinear signal. Therefore, it is fundamental to improve the sensitivity of the detection system, or in other words, to increase the SNR. One way to achieve this consists in trying to reduce the noise by acting on the electronic aspects of the detection. For instance, the frequency at which the desired signal is modulated directly affects the amount of noise that will appear in the demodulated signal and, generally, the goal is to be in the spectral region where white noise dominates over the flicker noise [80]. At the moment, modulation is obtained using a mechanical chopper, which not only poses a limit in terms of the highest achievable frequency to the order of few kHz, but it also adds substantial noise associated to mechanical vibrations and air turbulences. Specifically for the TFISH homodyne detection with the external SH bias, high frequency lock-in operation could also be attained by applying a sinusoidal behavior to the interference phase term $\Delta\phi$ with the help of the piezo scanner placed along the external LO path, as depicted in fig. 3.1. Indeed, when the phase term $\Delta\phi$ in eq. 2.73 oscillates between $2m\pi$ and $(2m + 1)\pi$, with m integer number, the polarity of the measured signal is periodically inverted, resulting in a factor 2 improvement of the signal. This happens because at each half period the signal switch from positive to negative, instead of alternating between null and non-null as in the chopper case.

In the current TFISH setup implementation, the homodyne signal is measured with a simple photodetector, implying that any fluctuation in the driving laser intensity contributes to the noise in the measured trace. On the other hand, in the EOS scheme we take advantage of

the balanced detection to suppress any common-mode components, globally reducing the noise contributions. In principle, balanced detection can be exploited even for the TFISH detection but we need to ensure that the desired signal does not get suppressed by the difference operation. Indeed, splitting the beam, already including both TFISH and LO, with a simple beamsplitter leads to a null signal because both arms contain the same information. Conversely, using a polarizing beamsplitter and keeping the TFISH field linearly polarized along one of the two orthogonal directions, while rotating the LO's linear polarization at 45° with respect to the TFISH's one, results in a non-zero signal since only the LO background is removed, whereas the information associated to the TFISH homodyne mixing "survives" because it is contained in only one branch.

Alternatively, splitting of the LO's optical spectrum could potentially lead to a successful balanced detection of the TFISH signal. In particular, taking into consideration that the two parametric processes of FWM for TFISH generation, i.e. the DFG and SFG processes as introduced in subsection 2.6.3, are spectrally translated with respect to the central wavelength 2ω of the SH bias, we could use a spectral filter with cut-on (or cut-off) wavelength exactly equal to 2ω. Provided that the efficiency of one of the two FWM processes is very low with respect to the other, then in one branch we obtain the mixing between the TFISH and the LO, while in the other we basically get only the LO, leading to successful balanced detection.

Curiously, the requirement to efficiently generate only one of the two parametric process for TFISH is not difficult to be satisfied. As discussed in appendix A, the chosen cut for the 4H-SiC substantially favors the DFG over the SFG due to velocity matching arguments. Furthermore, preliminary measurements exploiting spectral filtering confirmed that the contribution of the DFG to the detected TFISH signal is substantially stronger than for the SFG case. As a matter of fact, spectral filtering appears to be beneficial even in the case of detection with a single photodetector when the two FWM processes do not present the same efficiency. The measurements were done using the same configuration described in section 3.2, but replacing the optical band-pass filter with a long-pass filter (775nm-LP) and a short-pass filter (775nm-SP), respectively. Indeed, looking at fig. 5.1, we notice that the signal detected when using the 775nm-LP is roughly 4 times larger, in terms of peak-to-peak value, than when using the short-pass filter. It also suggests that, when the entire optical spectrum is detected (unfiltered), there might be destructive interference between the DFG and SFG contributions, likely due to their velocity mismatch, since the signal obtained (rescaled to take into account that the collected LO power is twice the one of the LP/SP filtered one) is much weaker than in the case of LP filtering. Actually, the difference between the LP filtered signal and the unfiltered one is not only in strength, but also in terms of waveform, as it can be observed comparing the blue and black traces. The situation is even more complicated by
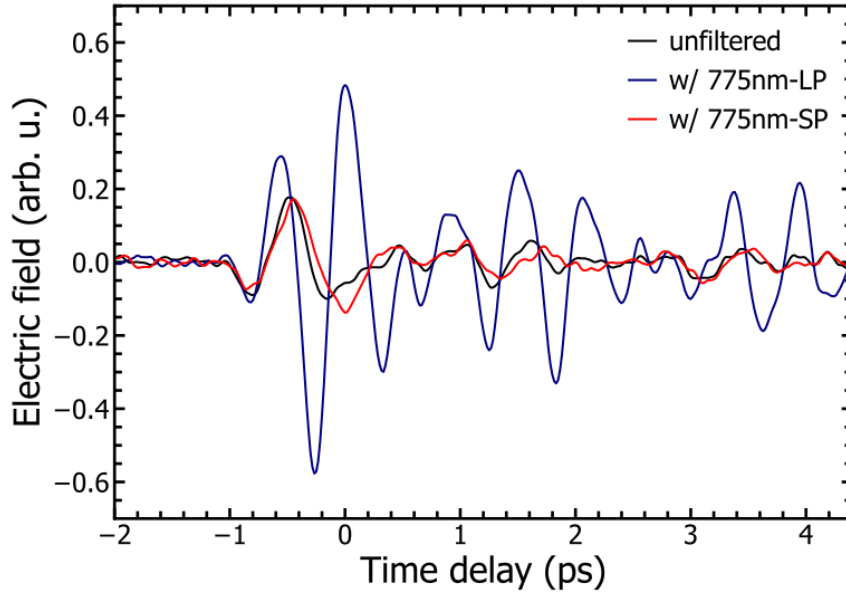
Figure 5.1 Effect of spectral filtering on TFISH detection efficiency. The time-resolved transients are reported for the case of no optical filtering (in black), long-pass filtering with cut-on wavelength at 775 nm (in blue) and short-pass filtering with cut-off wavelength at 775 nm (in red). To get a fair comparison of the signal strength, the traces are rescaled to the same noise floor.

the fact that the spectrum of the SH bias generated within the 4H-SiC sample, which behaves as LO, is spectrally modulated since the type I and II SH components are slightly delayed with respect to each other as a consequence of the substrate birefringence. Although this topic requires further analysis and modeling, especially for this "nonlinear" birefringence, to retrieve a more complete picture of the processes happening inside the substrate, it already shows significant results in terms of sensitivity improvements.

Finally, one of the most interesting features of the detection technique proposed in this work is the possibility to independently control the optical properties of the LO field (e.g. intensity, polarization, phase) since the SH bias is generated in a separate arm. However, as discussed in subsection 4.2.2, in the current state of the setup the interference between TFISH and LO suffers substantially from the environment noise and instabilities, even with the enclosure in place. As a consequence, delicate measurements that rely on the relative phase term $\Delta\phi$, such as the detection of the quadratures or the polarity inversion, are difficult to realize and hardly repetitive. While we are confident that reducing the free-space propagation distance in between the splitting and recombination of the probe and external LO branches

could already make this issue less relevant, we believe that the instabilities should be almost completely suppressed by potentially replacing the free-space propagation with propagation into waveguides.

Even though there are still challenges to overcome for realizing an integrated device for the THz range, like the fact that waveguides able to efficiently confine THz radiation are yet to be developed, such transition seems to be very promising for the mid-IR region. Indeed, the great interest for this spectral interval has led to a considerable progress in the availability of laser sources and integrated photonic devices [81]. Not to mention, phase matching simulations of the TFISH generation in centrosymmetric materials, e.g. diamond (see appendix A), suggest that this process is actually more efficient when the low-frequency field enters the mid-IR range. Hence, everything looks to be set to try exploring this alternative implementation.

To conclude, this present work demonstrates four-wave mixing scheme as particularly advantageous for integrated and quantum photonic applications. Engineering of waveguide dispersion, transmission, and nonlinear coupling together with on- and off-chip light coupling form many important engineering tasks which will be investigated with future generations of this detection scheme. Integrated and quantum photonics in the mid-IR and terahertz frequency range are particularly attractive not only for device initialization and low-energy photonic footprint, but also promise the most efficient on-chip cooling strategies enabling next-generation quantum sensing, communication, and computing, with the immeasurable economic impact those advances entail.

REFERENCES

[1] X.-C. Zhang, *Introduction to THz Wave Photonics.* [Online]. Available: https://link.springer.com/book/10.1007/978-1-4419-0978-7

[2] Y.-S. Lee, *Principles of Terahertz Science and Technology.* [Online]. Available: https://link.springer.com/book/10.1007/978-0-387-09540-0

[3] M. C. Hoffmann and J. A. Fülöp, "Intense ultrashort terahertz pulses: generation and applications," *Journal of Physics D: Applied Physics*, vol. 44, no. 8, p. 083001, Feb. 2011, publisher: IOP Publishing. [Online]. Available: https://doi.org/10.1088/0022-3727/44/8/083001

[4] B. E. Saleh and M. C. Teich, *Fundamentals of photonics*, 3rd ed. john Wiley & sons, 2019.

[5] A. Stingl *et al.*, "Generation of 11-fs pulses from a Ti:sapphire laser without the use of prisms," *Optics Letters*, vol. 19, no. 3, pp. 204–206, Feb. 1994, publisher: Optica Publishing Group. [Online]. Available: https://opg.optica.org/ol/abstract.cfm?uri=ol-19-3-204

[6] R. J. Mears *et al.*, "Low-noise erbium-doped fibre amplifier operating at 1.54μm," *Electronics Letters*, vol. 23, no. 19, pp. 1026–1028, Sep. 1987, publisher: IET Digital Library. [Online]. Available: https://digital-library.theiet.org/content/journals/10.1049/el_19870719

[7] C. Fattinger and D. Grischkowsky, "Terahertz beams," *Applied Physics Letters*, vol. 54, no. 6, pp. 490–492, Feb. 1989, publisher: American Institute of Physics. [Online]. Available: https://aip.scitation.org/doi/10.1063/1.100958

[8] Q. Wu and X. Zhang, "Free-space electro-optic sampling of terahertz beams," *Applied Physics Letters*, vol. 67, no. 24, pp. 3523–3525, Dec. 1995, publisher: American Institute of Physics. [Online]. Available: https://aip.scitation.org/doi/10.1063/1.114909

[9] M. v. Exter, C. Fattinger, and D. Grischkowsky, "Terahertz time-domain spectroscopy of water vapor," *Optics Letters*, vol. 14, no. 20, pp. 1128–1130, Oct. 1989, publisher: Optica Publishing Group. [Online]. Available: https://opg.optica.org/ol/abstract.cfm?uri=ol-14-20-1128

[10] H. Elayan *et al.*, *Terahertz Communication: The Opportunities of Wireless Technology Beyond 5G*, Apr. 2018.

[11] R. J. Mattauch and T. W. Crowe, "GaAs Schottky devices for submillimeter wavelengths," *International Journal of Infrared and Millimeter Waves*, vol. 8, no. 10, pp. 1235–1241, Oct. 1987. [Online]. Available: https://doi.org/10.1007/BF01011074

[12] T. Y. Chang, T. J. Bridges, and E. G. Burkhardt, "cw SUBMILLIMETER LASER ACTION IN OPTICALLY PUMPED METHYL FLUORIDE, METHYL ALCOHOL, AND VINYL CHLORIDE GASES," *Applied Physics Letters*, vol. 17, no. 6, pp. 249–251, Sep. 1970, publisher: American Institute of Physics. [Online]. Available: https://aip.scitation.org/doi/abs/10.1063/1.1653386

[13] C. Sirtori *et al.*, "Quantum cascade lasers: The semiconductor solution for lasers in the mid- and far-infrared spectral regions," *physica status solidi (a)*, vol. 203, no. 14, pp. 3533–3537, 2006, _eprint: https://onlinelibrary.wiley.com/doi/pdf/10.1002/pssa.200622389. [Online]. Available: https://onlinelibrary.wiley.com/doi/abs/10.1002/pssa.200622389

[14] R. Köhler *et al.*, "Terahertz semiconductor-heterostructure laser," *Nature*, vol. 417, no. 6885, pp. 156–159, May 2002, number: 6885 Publisher: Nature Publishing Group. [Online]. Available: https://www.nature.com/articles/417156a

[15] D. H. Auston and P. R. Smith, "Generation and detection of millimeter waves by picosecond photoconductivity," *Applied Physics Letters*, vol. 43, no. 7, pp. 631–633, Oct. 1983, publisher: American Institute of Physics. [Online]. Available: https://aip.scitation.org/doi/10.1063/1.94468

[16] T. Löffler *et al.*, "Large-area electro-optic ZnTe terahertz emitters," *Optics Express*, vol. 13, no. 14, pp. 5353–5362, Jul. 2005, publisher: Optica Publishing Group. [Online]. Available: https://opg.optica.org/oe/abstract.cfm?uri=oe-13-14-5353

[17] C. Kübler, R. Huber, and A. Leitenstorfer, "Ultrabroadband terahertz pulses: generation and field-resolved detection," *Semiconductor Science and Technology*, vol. 20, no. 7, pp. S128–S133, Jun. 2005, publisher: IOP Publishing. [Online]. Available: https://doi.org/10.1088/0268-1242/20/7/002

[18] R. A. Kaindl *et al.*, "Broadband phase-matched difference frequency mixing of femtosecond pulses in GaSe: Experiment and theory," *Applied Physics Letters*, vol. 75,

no. 8, pp. 1060–1062, Aug. 1999, publisher: American Institute of Physics. [Online]. Available: https://aip.scitation.org/doi/10.1063/1.124596

[19] R. Huber *et al.*, "Generation and field-resolved detection of femtosecond electromagnetic pulses tunable up to 41 THz," *Applied Physics Letters*, vol. 76, no. 22, pp. 3191–3193, May 2000, publisher: American Institute of Physics. [Online]. Available: https://aip.scitation.org/doi/10.1063/1.126625

[20] Y. Zhang, K. Li, and H. Zhao, "Intense terahertz radiation: generation and application," *Frontiers of Optoelectronics*, vol. 14, no. 1, pp. 4–36, Mar. 2021. [Online]. Available: https://doi.org/10.1007/s12200-020-1052-9

[21] D. J. Cook and R. M. Hochstrasser, "Intense terahertz pulses by four-wave rectification in air," *Optics Letters*, vol. 25, no. 16, pp. 1210–1212, Aug. 2000, publisher: Optica Publishing Group. [Online]. Available: https://opg.optica.org/ol/abstract.cfm?uri=ol-25-16-1210

[22] S. Kono, M. Tani, and K. Sakai, "Coherent detection of mid-infrared radiation up to 60 THz with an LT-GaAs photoconductive antenna," *IEE Proceedings - Optoelectronics*, vol. 149, no. 3, pp. 105–109, Jun. 2002, publisher: IET Digital Library. [Online]. Available: https://digital-library.theiet.org/content/journals/10.1049/ip-opt_20020262

[23] D. Turan *et al.*, "Telecommunication-Compatible Bias-Free Photoconductive Source with a 5 THz Radiation Bandwidth," in *Conference on Lasers and Electro-Optics (2020), paper SM4F.3*. Optica Publishing Group, May 2020, p. SM4F.3. [Online]. Available: https://opg.optica.org/abstract.cfm?uri=CLEO_SI-2020-SM4F.3

[24] A. Leitenstorfer *et al.*, "Detectors and sources for ultrabroadband electro-optic sampling: Experiment and theory," *Applied Physics Letters*, vol. 74, no. 11, pp. 1516–1518, Mar. 1999, publisher: American Institute of Physics. [Online]. Available: https://aip.scitation.org/doi/10.1063/1.123601

[25] A. Nahata and T. F. Heinz, "Detection of freely propagating terahertz radiation by use of optical second-harmonic generation," *Optics Letters*, vol. 23, no. 1, pp. 67–69, Jan. 1998, publisher: Optica Publishing Group. [Online]. Available: https://opg.optica.org/ol/abstract.cfm?uri=ol-23-1-67

[26] J. Dai, X. Xie, and X.-C. Zhang, "Detection of Broadband Terahertz Waves with a Laser-Induced Plasma in Gases," *Physical Review Letters*, vol. 97, no. 10,

p. 103903, Sep. 2006, publisher: American Physical Society. [Online]. Available: https://link.aps.org/doi/10.1103/PhysRevLett.97.103903

[27] N. Karpowicz *et al.*, "Coherent heterodyne time-domain spectrometry covering the entire "terahertz gap"," *Applied Physics Letters*, vol. 92, no. 1, p. 011131, Jan. 2008, publisher: American Institute of Physics. [Online]. Available: https://aip.scitation.org/doi/10.1063/1.2828709

[28] C.-Y. Li *et al.*, "Broadband field-resolved terahertz detection via laser induced air plasma with controlled optical bias," *Optics Express*, vol. 23, no. 9, pp. 11 436–11 443, May 2015, publisher: Optica Publishing Group. [Online]. Available: https://opg.optica.org/oe/abstract.cfm?uri=oe-23-9-11436

[29] S. Gundogdu *et al.*, "Self-referenced subcycle metrology of quantum fields," Jan. 2022, arXiv:2201.10487 [physics, physics:quant-ph]. [Online]. Available: http://arxiv.org/abs/2201.10487

[30] S. Virally and B. Reulet, "Unidimensional time-domain quantum optics," *Physical Review A*, vol. 100, no. 2, p. 023833, Aug. 2019, publisher: American Physical Society. [Online]. Available: https://link.aps.org/doi/10.1103/PhysRevA.100.023833

[31] P. Sulzer *et al.*, "Determination of the electric field and its Hilbert transform in femtosecond electro-optic sampling," *Physical Review A*, vol. 101, no. 3, p. 033821, Mar. 2020, publisher: American Physical Society. [Online]. Available: https://link.aps.org/doi/10.1103/PhysRevA.101.033821

[32] E. Hecht, *Optics*. Reading, Mass.: Addison-Wesley, 2002.

[33] D. R. Paschotta, "Time-Bandwidth Product." [Online]. Available: https://www.rp-photonics.com/time_bandwidth_product.html

[34] A. Weiner, *Ultrafast optics*. John Wiley & Sons, 2011, vol. 72.

[35] R. Boyd and D. Prato, *Nonlinear Optics*. Elsevier Science, 2008. [Online]. Available: https://books.google.ca/books?id=uoRUi1Yb7ooC

[36] R. Trebino *et al.*, "Measuring ultrashort laser pulses in the time-frequency domain using frequency-resolved optical gating," *Review of Scientific Instruments*, vol. 68, no. 9, pp. 3277–3295, Sep. 1997, publisher: American Institute of Physics. [Online]. Available: https://aip.scitation.org/doi/10.1063/1.1148286

[37] D. Kane and R. Trebino, "Characterization of arbitrary femtosecond pulses using frequency-resolved optical gating," *IEEE Journal of Quantum Electronics*, vol. 29, no. 2, pp. 571–579, Feb. 1993, conference Name: IEEE Journal of Quantum Electronics.

[38] R. Sutherland, *Handbook of Nonlinear Optics*, ser. Optical Science and Engineering. Taylor & Francis, 2003. [Online]. Available: https://books.google.ca/books?id=ccXo3WrHp2UC

[39] Y. C. Shen *et al.*, "Generation and detection of ultrabroadband terahertz radiation using photoconductive emitters and receivers," *Applied Physics Letters*, vol. 85, no. 2, pp. 164–166, Jul. 2004, publisher: American Institute of Physics. [Online]. Available: https://aip.scitation.org/doi/10.1063/1.1768313

[40] A. D. Koulouklidis *et al.*, "Observation of extremely efficient terahertz generation from mid-infrared two-color laser filaments," *Nature Communications*, vol. 11, no. 1, p. 292, Jan. 2020, number: 1 Publisher: Nature Publishing Group. [Online]. Available: https://www.nature.com/articles/s41467-019-14206-x

[41] K. Y. Kim *et al.*, "Terahertz emission from ultrafast ionizing air in symmetry-broken laser fields," *Optics Express*, vol. 15, no. 8, pp. 4577–4584, Apr. 2007, publisher: Optica Publishing Group. [Online]. Available: https://opg.optica.org/oe/abstract.cfm?uri=oe-15-8-4577

[42] N. Karpowicz, X. Lu, and X.-C. Zhang, "Terahertz gas photonics," *Journal of Modern Optics*, vol. 56, no. 10, pp. 1137–1150, Jun. 2009, publisher: Taylor & Francis _eprint: https://doi.org/10.1080/09500340902985361. [Online]. Available: https://doi.org/10.1080/09500340902985361

[43] E. Matsubara, M. Nagai, and M. Ashida, "Coherent infrared spectroscopy system from terahertz to near infrared using air plasma produced by 10-fs pulses," *JOSA B*, vol. 30, no. 6, pp. 1627–1630, Jun. 2013, publisher: Optica Publishing Group. [Online]. Available: https://opg.optica.org/josab/abstract.cfm?uri=josab-30-6-1627

[44] H. J. Bakker *et al.*, "Distortion of terahertz pulses in electro-optic sampling," *JOSA B*, vol. 15, no. 6, pp. 1795–1801, Jun. 1998, publisher: Optica Publishing Group. [Online]. Available: https://opg.optica.org/josab/abstract.cfm?uri=josab-15-6-1795

[45] F. Blanchard *et al.*, "Generation of 1.5 μJ single-cycle terahertz pulses by optical rectification from a large aperture ZnTe crystal," *Optics Express*, vol. 15, no. 20, pp.

13 212–13 220, Oct. 2007, publisher: Optica Publishing Group. [Online]. Available: https://opg.optica.org/oe/abstract.cfm?uri=oe-15-20-13212

[46] O. Hatem, "Optimizing the electro-optic detection of terahertz waves by ZnTe at 780 and 1560-nm probe-beam wavelengths," *Journal of Nonlinear Optical Physics & Materials*, Mar. 2019, publisher: World Scientific Publishing Company. [Online]. Available: https://www.worldscientific.com/doi/epdf/10.1142/S0218863518500431

[47] G. Chang *et al.*, "Power scalable compact THz system based on an ultrafast Yb-doped fiber amplifier," *Optics Express*, vol. 14, no. 17, pp. 7909–7913, Aug. 2006, publisher: Optica Publishing Group. [Online]. Available: https://opg.optica.org/oe/abstract.cfm?uri=oe-14-17-7909

[48] K. L. Vodopyanov, "Optical generation of narrow-band terahertz packets in periodically-inverted electro-optic crystals: conversion efficiency and optimal laser pulse format," p. 14, 2006.

[49] J. Hebling *et al.*, "Velocity matching by pulse front tilting for large-area THz-pulse generation," *Optics Express*, vol. 10, no. 21, pp. 1161–1166, Oct. 2002, publisher: Optica Publishing Group. [Online]. Available: https://opg.optica.org/oe/abstract.cfm?uri=oe-10-21-1161

[50] S.-G. Park, M. R. Melloch, and A. M. Weiner, "Comparison of terahertz waveforms measured by electro-optic and photoconductive sampling," *Applied Physics Letters*, vol. 73, no. 22, pp. 3184–3186, Nov. 1998, publisher: American Institute of Physics. [Online]. Available: https://aip.scitation.org/doi/10.1063/1.122712

[51] G. Gallot *et al.*, "Measurements of the THz absorption and dispersion of ZnTe and their relevance to the electro-optic detection of THz radiation," *Applied Physics Letters*, vol. 74, no. 23, pp. 3450–3452, Jun. 1999, publisher: American Institute of Physics. [Online]. Available: https://aip.scitation.org/doi/10.1063/1.124124

[52] G. Sharma *et al.*, "Terahertz detection using spectral domain interferometry," *Optics Letters*, vol. 37, no. 20, pp. 4338–4340, Oct. 2012, publisher: Optica Publishing Group. [Online]. Available: https://opg.optica.org/ol/abstract.cfm?uri=ol-37-20-4338

[53] J. Chen, P. Han, and X.-C. Zhang, "Terahertz-field-induced second-harmonic generation in a beta barium borate crystal and its application in terahertz detection," *Applied Physics Letters*, vol. 95, no. 1, p. 011118, Jul. 2009, publisher: American Institute of Physics. [Online]. Available: https://aip.scitation.org/doi/10.1063/1.3176439

[54] A. Tomasino *et al.*, "Solid-state-biased coherent detection of ultra-broadband terahertz pulses," *Optica*, vol. 4, no. 11, pp. 1358–1362, Nov. 2017, publisher: Optica Publishing Group. [Online]. Available: https://opg.optica.org/optica/abstract.cfm?uri=optica-4-11-1358

[55] A. Tomasino *et al.*, "Ultra-broadband terahertz coherent detection via a silicon nitride-based deep sub-wavelength metallic slit," *APL Photonics*, vol. 3, no. 11, p. 110805, Nov. 2018, number: 11 Publisher: AIP Publishing. [Online]. Available: https://aip.scitation.org/doi/10.1063/1.5052628

[56] E. Matsubara, M. Nagai, and M. Ashida, "Coherent detection of ultrabroadband infrared pulses using a single crystal of diamond," *Applied Physics Express*, vol. 14, no. 3, p. 032005, Feb. 2021, publisher: IOP Publishing. [Online]. Available: https://doi.org/10.35848/1882-0786/abdef4

[57] G. Gallot and D. Grischkowsky, "Electro-optic detection of terahertz radiation," *JOSA B*, vol. 16, no. 8, pp. 1204–1212, Aug. 1999, publisher: Optica Publishing Group. [Online]. Available: https://opg.optica.org/josab/abstract.cfm?uri=josab-16-8-1204

[58] J. Faure *et al.*, "Modelling Laser-Based Table-Top THz Sources: Optical Rectification, Propagation and Electro-Optic Sampling," *Optical and Quantum Electronics*, vol. 36, no. 8, pp. 681–697, Jun. 2004. [Online]. Available: https://doi.org/10.1023/B:OQEL.0000039617.85129.c2

[59] S. Namba, "Electro-Optical Effect of Zincblende," *JOSA*, vol. 51, no. 1, pp. 76–79, Jan. 1961, publisher: Optica Publishing Group. [Online]. Available: https://opg.optica.org/josa/abstract.cfm?uri=josa-51-1-76

[60] C. Riek, D. V. Seletskiy, and A. Leitenstorfer, "Femtosecond measurements of electric fields: from classical amplitudes to quantum fluctuations," *European Journal of Physics*, vol. 38, no. 2, p. 024003, Jan. 2017, publisher: IOP Publishing. [Online]. Available: https://doi.org/10.1088/1361-6404/aa53a2

[61] H. A. Bethe, "Theory of Diffraction by Small Holes," *Physical Review*, vol. 66, no. 7-8, pp. 163–182, Oct. 1944, publisher: American Physical Society. [Online]. Available: https://link.aps.org/doi/10.1103/PhysRev.66.163

[62] D. R. Paschotta, "Balanced photodetection." [Online]. Available: https://www.rp-photonics.com/balanced_photodetection.html

[63] S. R. Systems, "About Lock-In Amplifiers." [Online]. Available: https://www.thinksrs. com/downloads/pdfs/applicationnotes/AboutLIAs.pdf

[64] Z. Instruments, "Principles of lock-in detection and the state of the art," 2016. [Online]. Available: https://www.zhinst.com/americas/en/resources/ principles-of-lock-in-detection

[65] G. Cerullo, S. D. Silvestri, and C. Manzoni, "Optical Parametric Amplifiers," in *Encyclopedia of Modern Optics (Second Edition)*, second edition ed., B. D. Guenther and D. G. Steel, Eds.   Oxford: Elsevier, 2018, pp. 290–301. [Online]. Available: https://www.sciencedirect.com/science/article/pii/B9780128035818096326

[66] I. H. Malitson, "A Redetermination of Some Optical Properties of Calcium Fluoride," *Applied Optics*, vol. 2, no. 11, pp. 1103–1107, Nov. 1963, publisher: Optica Publishing Group. [Online]. Available: https://opg.optica.org/ao/abstract.cfm?uri=ao-2-11-1103

[67] "Terahertz Low Pass Filters (MTI)." [Online]. Available: https://mtinstruments.com/ MicroTech_Resources/THz-Low-Pass-Filters-graph-cleaned.pdf

[68] "THz Materials (TYDEX)." [Online]. Available: https://www.tydexoptics.com/pdf/ THz_Materials.pdf

[69] D. R. Paschotta, "Polarizers." [Online]. Available: https://www.rp-photonics.com/ polarizers.html

[70] J.-C. M. Diels *et al.*, "Control and measurement of ultrashort pulse shapes (in amplitude and phase) with femtosecond accuracy," *Applied Optics*, vol. 24, no. 9, pp. 1270–1282, May 1985, publisher: Optica Publishing Group. [Online]. Available: https://opg.optica.org/ao/abstract.cfm?uri=ao-24-9-1270

[71] L. Guiramand *et al.*, "Time-frequency analysis of two-photon absorption effect during optical rectification in a ZnTe crystal pumped at 1.024 µm," *Optics Letters*, vol. 46, no. 24, pp. 6047–6050, Dec. 2021, publisher: Optica Publishing Group. [Online]. Available: https://opg.optica.org/ol/abstract.cfm?uri=ol-46-24-6047

[72] "Hilbert transform," Aug. 2022, page Version ID: 1105932609. [Online]. Available: https://en.wikipedia.org/w/index.php?title=Hilbert_transform&oldid=1105932609

[73] M. Born and E. Wolf, *Principles of Optics: Electromagnetic Theory of Propagation, Interference and Diffraction of Light.*   CUP Archive, Feb. 2000.

[74] X. Xin *et al.*, "Terahertz absorption spectrum of para and ortho water vapors at different humidities at room temperature," *Journal of Applied Physics*, vol. 100, no. 9, p. 094905, Nov. 2006, publisher: American Institute of Physics. [Online]. Available: https://aip.scitation.org/doi/10.1063/1.2357412

[75] P. Rasekh *et al.*, "Terahertz Nonlinear Spectroscopy of Water Vapor," *ACS Photonics*, vol. 8, no. 6, pp. 1683–1688, Jun. 2021, publisher: American Chemical Society. [Online]. Available: https://doi.org/10.1021/acsphotonics.1c00056

[76] M. Knorr *et al.*, "Ultrabroadband etalon-free detection of infrared transients by van-der-Waals contacted sub-10-µm GaSe detectors," *Optics Express*, vol. 26, no. 15, pp. 19059–19066, Jul. 2018, publisher: Optica Publishing Group. [Online]. Available: https://opg.optica.org/oe/abstract.cfm?uri=oe-26-15-19059

[77] M. Naftaly *et al.*, "Silicon carbide - a high-transparency nonlinear material for THz applications," *Optics Express*, vol. 24, no. 3, pp. 2590–2595, Feb. 2016, publisher: Optica Publishing Group. [Online]. Available: https://opg.optica.org/oe/abstract.cfm?uri=oe-24-3-2590

[78] I. E. Gordon *et al.*, "The HITRAN2016 molecular spectroscopic database," *Journal of Quantitative Spectroscopy and Radiative Transfer*, vol. 203, pp. 3–69, Dec. 2017. [Online]. Available: https://www.sciencedirect.com/science/article/pii/S0022407317301073

[79] T. Seifert *et al.*, "Efficient metallic spintronic emitters of ultrabroadband terahertz radiation," *Nature Photonics*, vol. 10, no. 7, pp. 483–488, Jul. 2016, number: 7 Publisher: Nature Publishing Group. [Online]. Available: https://www.nature.com/articles/nphoton.2016.91

[80] R. F. Voss and J. Clarke, "Flicker ($\frac{1}{f}$) noise: Equilibrium temperature and resistance fluctuations," *Physical Review B*, vol. 13, no. 2, pp. 556–573, Jan. 1976, publisher: American Physical Society. [Online]. Available: https://link.aps.org/doi/10.1103/PhysRevB.13.556

[81] Y. Zou *et al.*, "Mid-infrared silicon photonic waveguides and devices [Invited]," *Photonics Research*, vol. 6, no. 4, pp. 254–276, Apr. 2018, publisher: Optica Publishing Group. [Online]. Available: https://opg.optica.org/prj/abstract.cfm?uri=prj-6-4-254

[82] R. P. Mildren, "Intrinsic Optical Properties of Diamond," in *Optical Engineering of Diamond*, 1st ed., R. P. Mildren and J. R. Rabeau, Eds. Wiley, Apr. 2013, pp. 1–34. [Online]. Available: https://onlinelibrary.wiley.com/doi/10.1002/9783527648603.ch1

[83] M. P. Fischer *et al.*, "Coherent field transients below 15 THz from phase-matched difference frequency generation in 4H-SiC," *Optics Letters*, vol. 42, no. 14, pp. 2687–2690, Jul. 2017, publisher: Optica Publishing Group. [Online]. Available: https://opg.optica.org/ol/abstract.cfm?uri=ol-42-14-2687

[84] S. Wang *et al.*, "4H-SiC: a new nonlinear material for midinfrared lasers," *Laser & Photonics Reviews*, vol. 7, no. 5, pp. 831–838, 2013, _eprint: https://onlinelibrary.wiley.com/doi/pdf/10.1002/lpor.201300068. [Online]. Available: https://onlinelibrary.wiley.com/doi/abs/10.1002/lpor.201300068

[85] G. Cerullo and S. De Silvestri, "Ultrafast optical parametric amplifiers," *Review of Scientific Instruments*, vol. 74, no. 1, pp. 1–18, Jan. 2003, publisher: American Institute of Physics. [Online]. Available: https://aip.scitation.org/doi/10.1063/1.1523642

APPENDIX A   PHASE MATCHING CALCULATIONS FOR TFISH GENERATION

In this section we discuss how to compute the phase matching conditions for terahertz-field-induced second-harmonic (TFISH) generation and then we present the corresponding frequency-dependent coherence length in two different nonlinear materials: diamond and silicon carbide (SiC).

We remind that the coherence length l_c is directly related to the wavevector mismatch Δk via

$$l_c = \frac{\pi}{|\Delta k|} \tag{A.1}$$

and the expression of the phase mismatch, which is a consequence of the momentum conservation, depends on the actual nonlinear process. In subsection 2.6.3 we showed that there are two possible parametric four-wave mixing (FWM) processes that lead to TFISH generation, which we define as sum-frequency-generation (SFG) and difference-frequency generation (DFG). The photons resulting from the FWM of the fundamental ω and THz Ω photons present frequency given by

$$2\omega_\pm = 2\omega \pm \Omega \tag{A.2}$$

where the "+" stands for the SFG, while the "−" for the DFG. The momentum conservation dictates that

$$\Delta k_\pm = 2\frac{n_\omega \omega}{c} \pm \frac{n_\Omega \Omega}{c} - \frac{n_{2\omega\pm}(2\omega \pm \Omega)}{c} \tag{A.3}$$

with n_i representing the refractive index of the chosen material at the corresponding frequency $(i = \omega, \Omega, 2\omega_\pm)$.

Diamond is a centrosymmetric material very promising for THz detection due to its excellent transparency and low dispersion across the entire infrared range. Nevertheless, to ensure efficient TFISH generation the coherence length l_c (see subsection 2.4.3) across the THz range of interest should be as high as possible: ideally, the thickness of the nonlinear material is chosen equal to the coherence length, hence the strength of the nonlinear signal is intrinsically determined by l_c. Being an isotropic dispersive material, the phase matching is strongly dependent on the choice of the frequency, or wavelength, of the fundamental. In panels (a) and (b) of fig. A.1 we report the coherence lengths for the DFG and SFG, respectively, FWM processes as function of the THz frequency for multiple choices of the fundamental

wavelength λ_p in the near and mid-IR. We observe that for a given λ_p, l_c is barely dependent on the THz frequency, slightly increasing (decreasing) at higher frequencies for DFG (SFG). On the other hand, by moving from a fundamental beam in the near-IR (1.55 μm) to one in the mid-IR (3.2 μm), the coherence length gradually increases, up to almost a factor of 10. Therefore, it looks like the only way to get a coherence length larger that 100 μm is to choose an excitation source in the mid-IR.
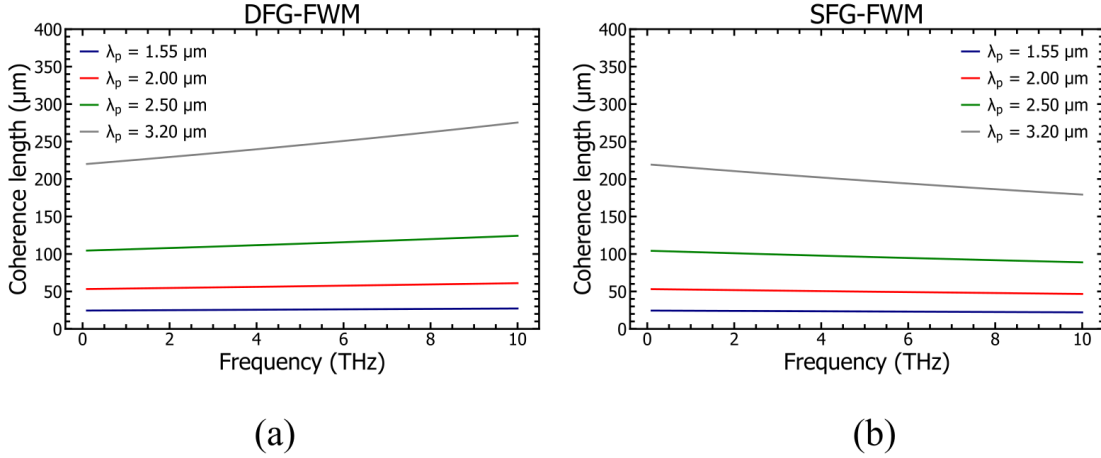

Figure A.1 Simulations of phase matching conditions for TFISH generation in diamond. The resulting frequency-dependent coherence length is reported for multiple excitation wavelengths (λ_p) for the DFG (panel (a)) and SFG (panel(b)) four-wave mixing processes. Refractive index data for diamond taken from [82].

Silicon carbide proved to be another crystal with outstanding properties for nonlinear optics applications in the terahertz range [83], in particular its polymorph with hexagonal symmetry, i.e. 4H-SiC. Conversely to diamond, 4H-SiC is a uniaxial birefringent crystal and this property can be exploited to get proper phase matching over the range of interest, even for the widely diffused excitation sources in the near-IR (e.g. at 1.55 μm). Indeed, provided that the various fields participating in the FWM process are oscillating along the required polarizations, the orientation of the cut of the 4H-SiC substrate can be chosen so that the mismatch in refractive index due to dispersion is compensated by the birefringence, according to eq. 2.46.

The 4H-SiC used in this work is cut in such a way that the angle between the <0001> axis (optical axis) and the <1120> axis is of 90°, as shown in panel (a) of fig. A.2. The choice is due to the fact that with this orientation, which is commercially available, using a 1.55 μm excitation source, the DFG process presents a decent phase matching up to 5 THz. Indeed, looking at fig. A.2(b) we observe that the coherence length is larger than 100 μm in this

frequency range, implying that a substrate with such thickness, which is already enough to induce detectable upconverted signals, can be used without compromising the bandwidth. Additionally, by varying the incidence angle between the wavevector and the optical axis, the phase matched frequency (which is around 1.65 THz in the presented plot) can be adjusted across the entire interval 0.1-10 THz. For this to happen, the required polarizations are (o = ordinary, e = extraordinary):

- $\omega = e$
- $\Omega = o$
- $2\omega_\pm = o$

With this orientation of the 4H-SiC, the SFG results less efficient than the DFG one, but the situation can be easily reversed by varying the angle of cut or the incidence angle.
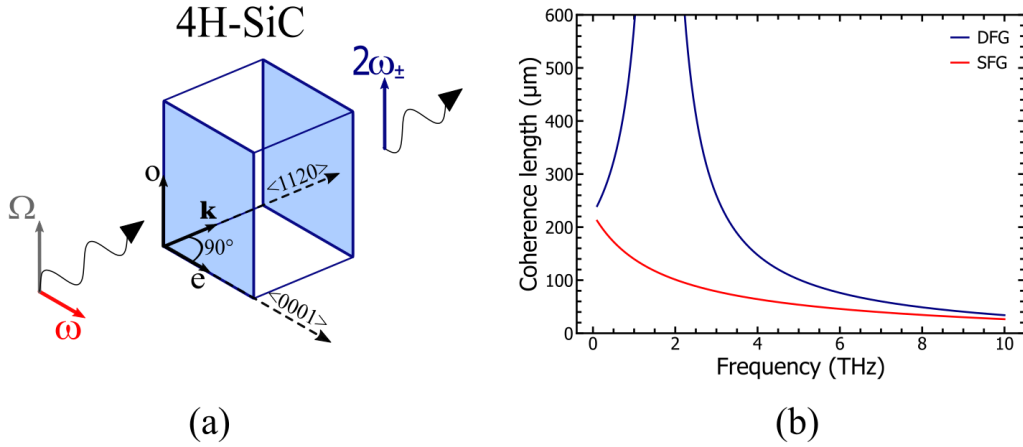

(a)   (b)

Figure A.2 Simulations of phase matching conditions for TFISH generation in 4H-SiC. (a) Orientation of cut of the 4H-SiC substrate employed in this work, with required polarization of the fundamental (ω), THz (Ω) and TFISH ($2\omega_\pm$) beams along either the ordinary (o) or extraordinary (e) axes. (b) Corresponding frequency-dependent coherence length of DFG (blue line) and SFG (red line) FWM processes considering the fundamental wavelength to be at 1.55 μm. Refractive index data for 4H-SiC taken from [77, 84].

APPENDIX B   COLLINEAR OPTICAL PARAMETRIC AMPLIFIER

The following part contains an insight regarding the architecture of an optical parametric amplifier (OPA). Generally, the structure of an OPA system can be divided into three subunits [65, 85], as shown in fig. B.1:

1. *Seed pulse generation stage*: a weak and broadband pulse at the signal frequency is generated exploiting a nonlinear process. This seed pulse will initiate the OPA process.

2. *Parametric amplification stage*: it is the section where the energy from the intense pump beam (or from one of its higher order harmonics) is transferred to the weak seed beam. Typically, it includes multiple gain stages.

3. *Pulse compression stage*: it has the goal to obtain pulse with duration close to the transform-limited (TL) condition.
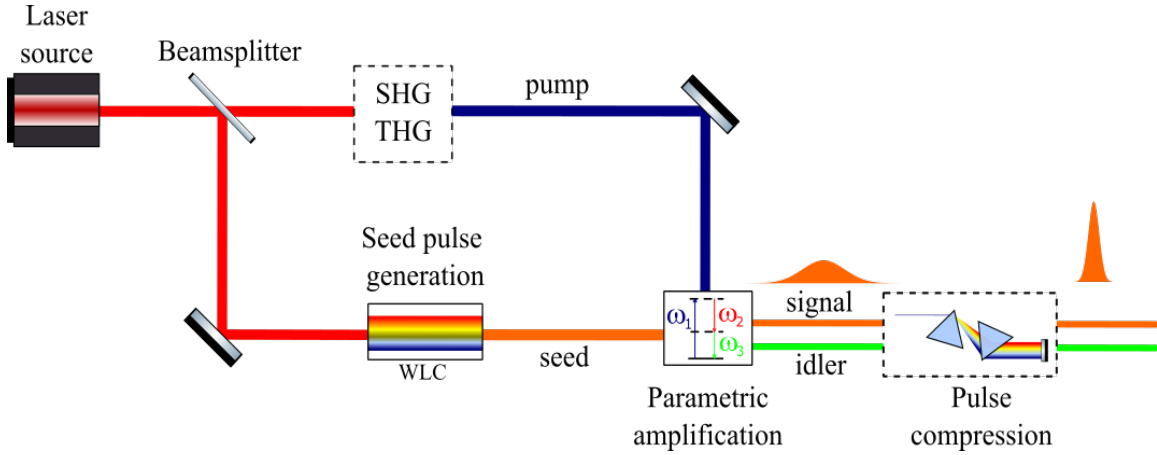

Figure B.1 General structure of an OPA. The dashed boxes indicate parts that are not always required for the OPA functionality, but they might be needed depending on the particular case.

Seed Pulse Generation   Reminding that one of the most interesting properties of an OPA system is the tunability over a wide range of frequencies, it is of fundamental importance to have a broadband seed pulse. A very common nonlinear process used to get such a pulse is supercontinuum generation (SG), also known as white-light generation (WLG): when a sufficiently intense ultrashort pulse propagates through a transparent dielectric medium the

pulse spectrum undergoes a dramatic spectral broadening. This broadening generally exceeds the one that is observed due to the effect of self-phase modulation acting alone, hence the origin of the name supercontinuum. Being based on a $\chi^{(3)}$ nonlinearity, this phenomenon may be observed in gases, liquids and solids. Here we provide an approximate explanation of SG, which is a very intricate process that implies an interplay of both spatial (self-focusing, diffraction) and temporal (dispersion, self-phase modulation) effects [35, 38, 65].

At the beginning of the propagation through the material, when the dispersion has still to come strongly into play, the peak of the pulse is the first temporal region to undergo self-focusing. This in turn increases its intensity and causes a strong spectral broadening due to self-phase modulation. Then, the dispersion kicks in, leading to a spreading in time and causing a flow of energy from the center of the pulse towards the leading and trailing edges [85]. Hence, the combination of self-focusing, SPM and dispersion tends to split the input pulse into two fragments. At this point, since we are dealing with a short and broadband pulse, we have to take into account the effect of self-steepening, which is a consequence of the optical Kerr effect when the group velocity is intensity-dependent: it can be shown [34] that in these conditions the velocity of the peak of the pulse is reduced and therefore the slope of the trailing edge is larger. The self-steepening combined with the pulse splitting introduced above unifies the two fragments into a unique stronger filament, which compresses in time, toward the trailing edge of the original pulse.

By properly tuning the pulse energy and the focusing conditions, a single stable filament of supercontinuum can be obtained. This is ideal for the generation of the OPA seed signal because it produces pulses with diffraction-limited spatial profile and with a very low shot-to-shot energy fluctuations [65]. A good choice of the $\chi^{(3)}$ material for SG is undoped sapphire because it presents high thermal conductivity and high damage threshold.

Parametric Amplification   This is the part where the actual amplification of the weak seed pulse takes place. The most common scheme implies a multistage gain because it allows to distribute the available pump intensity and get the best conversion of energy from pump to signal beam. Indeed, only a small part of the pump beam should be dedicated to the first stage, called preamplifier or signal amplifier, which presents a very high gain (ranging from 10^3 to 10^5) and has the goal to amplify the low-energy seed. In this way, the remaining large part of the pump intensity is used in the final gain stage, which is driven in the saturation regime to efficiently amplify the signal beam and minimize the pulse-to-pulse energy fluctuations. In addition, having a multistage scheme allows to compensate for the group velocity mismatch between pump and signal that originates within each stage [65].

The choice of the pump wavelength is mostly dictated by the desired tuning range of the OPA and by the transparency windows of the nonlinear crystal responsible for the amplification. The first criterion of choice is related to the energy conservation of the OPA process: for instance, in the case of a Yb-based laser, the tunability is limited to the IR region when the pump is the fundamental wavelength (1030 nm) of the laser source, while it extends down to roughly 650 nm and 400 nm when the pump wavelength is, respectively, the second-harmonic and third-harmonic of the driving laser [65]. The second criterion is fixed by the absorption curve of the crystal: both signal and idler frequencies must be out of the absorption region, otherwise the process would not be efficient.

Pulse Compression   As described in subsection 2.1.1, every time a pulse propagates through a medium, it suffers dispersion. Thus, in both the previously described stages, the amplified pulses accumulate spectral phase when going through the nonlinear crystals, the OPA crystal and all the other optical elements along the path. Depending on the bandwidth of the amplified pulses, this might lead to pulse durations significantly larger than the transform-limited one: the effect of dispersion is relevant for broadband pulses, which corresponds to TL duration of ∼30 fs or shorter, while for narrow bandwidths the accumulated spectral phase stretches the duration only by a small margin. Consequently, this subunit is optional. Generally, for wavelengths in the visible and near-IR regions, materials induce a positive chirp and common compression schemes are grating pairs, prism pairs and chirped mirrors [34].